UNIVERSITY OF CALIFORNIA SAN DIEGO

Moderate Resolution Spectroscopy of Directly Imaged Exoplanets

A dissertation submitted in partial satisfaction of the
requirements for the degree Doctor of Philosophy

in

Physics

by

Kielan Kathryn Wilcomb Hoch

Committee in charge:

Quinn Konopacky, Chair
Adam Burgasser
Alison Coil
James M. D. Day
Raphael Flauger
Marshall Perrin

2022

The Dissertation of Kielan Kathryn Wilcomb Hoch is approved, and it is acceptable in quality and form for publication on microfilm and electronically.

University of California San Diego

2022

DEDICATION

To my parents, Elaine and Keith Wilcomb,
my friends, Vinita Thakkar, Allison Cochrane, and Shelby Davis,
and my husband, Jeffrey Alexander Hoch.

TABLE OF CONTENTS

Dissertation Approval Page iii

Dedication iv

Table of Contents v

List of Figures vii

List of Tables xii

Acknowledgements xiii

Vita xvi

Abstract of the Dissertation xvii

Chapter 1 Introduction 1
1.0.1 Formation Tracers 5
1.0.2 An Imaging Spectroscopy Survey of Exoplanetary Atmospheres with Keck/OSIRIS 9

Chapter 2 Moderate-Resolution K-Band Spectroscopy of Substellar Companion κ Andromedae b 10
2.1 Introduction 11
2.2 Data Reduction 14
2.3 Spectral Modeling 18
2.3.1 Synthetic Spectra 18
2.3.2 Forward Modeling 19
2.3.3 Temperature, Gravity, and Metallicity 20
2.3.4 Mole Fractions of CO and H_2O 25
2.3.5 C/O Ratios 26
2.4 Kinematic Modeling 27
2.4.1 Radial Velocity Measurement 27
2.4.2 Orbital Analysis 30
2.5 Discussion and Conclusions 47

Chapter 3 Moderate-Resolution K-Band Spectroscopy of the Substellar Companion VHS 1256 b 51
3.1 Introduction 52
3.2 Data Reduction 54
3.3 Spectral Modeling 57
3.3.1 Synthetic Spectra 57
3.3.2 Forward Modeling 59

3.3.3 Temperature, Gravity, and Cloud Parameters 60
3.3.4 Mole Fractions of CO, H_2O, and CH_4 65
3.3.5 C/O Ratios 67
3.4 Discussion and Conclusions 68

Chapter 4 Directly Imaged Planets: C/O Ratio Formation Diagnostic and Comparisons to other Exoplanet Populations 77
4.1 Introduction 78
4.2 Data Reduction 80
4.3 Spectral Modeling 83
4.3.1 C and O Abundances 85
4.3.2 C/O Ratio for HD 284149b 85
4.4 Non-Detections 86
4.5 C/O Ratio Population Analysis 87
4.6 Discussion and Conclusions 90

Chapter 5 Summary and Future Work 103
5.1 Summary of Results and Conclusions 103
5.2 Future Work 105
5.2.1 Low-resolution, full infrared spectra 107
5.2.2 Moderate-Resolution, NIR spectra 108
5.2.3 Continuation of the Imaging Spectroscopy Survey of Exoplanetary Atmospheres with Keck/OSIRIS 110

Bibliography 111

LIST OF FIGURES

Figure 1.1: The demographics of planetary-mass companions detected via various methods. Bold symbols denote companions with spectroscopic measurements and atmospheric characterization. The directly imaged companions are dominant in this population. This figure was created by Dmitry Savran- 2

Figure 1.2: Cooling tracks for planets, brown dwarfs and stars. Each curve is at a constant mass. Typically today we are sensitive to planets around stars younger than 100 Myr old (Bowler, 2016). The orange lines denote objects greater than 80 M_{Jup}, the green lines denote objects 14-80 M_{Jup}, and the . . 3

Figure 1.3: Comparison of the occurrence rates from the GPIES and other surveys of 5–13 M_{Jup} planets **(top two panels)**, 13–80 M_{Jup} brown dwarfs **(bottom left)**, and 5–80 M_{Jup} substellar companions **(bottom right)** as a function of semimajor axis. Only higher-mass stars from GPIES were considered . 4

Figure 1.4: Estimated C/O ratios in gas (solid lines) and in dust (dashed lines) for an irradiated disk (top panel), an evolving disk (middle panel) and a viscous disk (bottom panel). The particle size increases from 0.05 to 700 cm shown by the color bar to the right. The horizontal dotted line represents the 8

Figure 2.1: An example data cube image frame, collapsed in wavelength via median, from our OSIRIS κ And b data set. The panel on the left shows a reduced cube before speckle removal, demonstrating the brightness of the speckles at the location of κ And b. The right panel shows the data cube after the . . 16

Figure 2.2: Our fully reduced, combined, and flux calibrated moderate-resolution OSIRIS *K*-band spectra of κ And b. The errors are shown as a shaded light blue region. 17

Figure 2.3: Results from the MCMC model fit to the OSIRIS spectrum for κ And b without continuum removal (black). The best matching *PHOENIX-ACES-DUSTY* model has $T_{\rm eff}$ = 1588 K, $\log g$ = 4.72, and a M/H = 0.50 (magenta). The residuals between the data and the model are plotted in gray. 22

Figure 2.4: Corner plot corresponding to the fit shown in Figure 2.3. {The diagonal shows the marginalized posteriors. The subsequent covariances between all the parameters are in the corresponding 2-d histograms. The blue lines represent the 50 percentile, and the dotted lines represent the 16 and 84 . . 33

Figure 2.5: Results from MCMC model fit to the OSIRIS spectrum after continuum removal (black). The best fitting model has $T_{\rm eff}$ = 2048 K, $\log g$ = 3.77, and [M/H] = −0.11 in magenta. The residuals between the flattened data and the flattened model are in gray. 34

Figure 2.6: Corner plot corresponding to the fit shown in Figure 2.5. The diagonal shows the marginalized posteriors. The subsequent covariances between all the parameters are in the corresponding 2-d histograms. The blue lines represent the 50 percentile, and the dotted lines represent the 16 and 84 .. 35

Figure 2.7: OSIRIS K-band data of κ And b compared to Currie et al. (2018) low-resolution CHARIS data of κ And b and their best-matching field source, 2MASS J01415823-4633574 from the SpeX Library (Kirkpatrick et al., 2006). A fit to the SpeX spectrum (not shown) reveals temperatures and .. 36

Figure 2.8: All available spectral and photometric data for κ And b compared to the best-fit *PHOENIX-ACES-DUSTY* model, shown in gray, of $T_{\rm eff}$ = 2048 K, $\log g$ = 3.77, and M/H = −0.11 over the near-infrared. Our OSIRIS data are shown in black. Currie et al. (2018) low-resolution CHARIS spectra 36

Figure 2.9: Results of $T_{\rm eff}$ = 2048 K and $\log g$ = 3.77 model fits with varying mole fractions for both H_2O and CO to our continuum-subtracted OSIRIS spectrum. The mole fractions are given in units relative to the ratio in the Sun, such that a value of zero implies the solar value. Both scalings of CO and H_2O 37

Figure 2.10: Visual comparison of three different $T_{\rm eff}$ = 2048 K and $\log g$ = 3.77 models with different values of C/O in our scaled mole fraction grid. The best fit C/O ratio is shown in the central panel, while values of very high (bottom) and very low (top) C/O ratio are clearly disfavored by our data. The relative 38

Figure 2.11: Radial velocity (RV) measurements of κ And b by individual exposures and epoch of observation. The grey region represents the current uncertainty in the RV of the star. The RVs are shown for different number of principal components (None, 1, 5, and 10 respectively) included in the data model. . 39

Figure 2.12: Same as Figure 2.11, but corrected for biases using simulated planet injection and recovery. The final RV values and uncertainties are available in Figure 2.3..... 39

Figure 2.13: Corner plot showing the results of fitting the orbit of κ And b, including both astrometry and radial velocities. In this case, we use the observationally based prior presented in O'Neil et al. (2019), which can help account for biases in parameters like T_0 that arise in undersampled orbits. Note that 40

Figure 2.14: The same as Figure 2.13, but with no RV included in the fit. The results give values for orbital parameters consistent with previous fits found in the literature. A secondary peak in Ω can be seen more prominently here around $\sim 270^o$ that is nearly absent in Figure 2.13. The addition of the RV 41

Figure 2.15: Corner plot showing the results of fitting the orbit of κ And b, including both astrometry and radial velocities. In this case, we use the typical flat priors in fit parameter space for easier comparison to previous work. Note that the use of these priors leads to a highly peaked prediction for T_0. 42

Figure 2.16: The same as Figure 2.15, but with no RV included in the fit. The results give values for orbital parameters consistent with previous fits found in the literature. Again, a secondary peak in Ω can be seen more prominently here around $\sim 270^o$ that is nearly absent in Figure 2.15. The addition of . . 43

Figure 2.17: Best-fit orbits with (red) or without (blue) inclusion of the OSIRIS RV using the observationally-based prior. Because of the large parameter space allowed by the astrometry, the best-fits are used here only for illustrative purposes. The left panel shows the orbits on the plane of the sky while . . . 44

Figure 2.18: The same as Figure 2.17, but using flat orbit parameter priors. Either choice of prior yields preferred orbit solutions that approach periastron in the next several years, stressing the utility of more RVs. 45

Figure 3.1: An example data cube image frame, collapsed in wavelength via median, from our OSIRIS VHS 1256 b data set. The field of view is $0.32''$ x $1.28''$. The dark spot represents the negative value from the companion subtraction at the other nod position. The bright spot shows the companion clearly . . . 55

Figure 3.2: Our fully reduced, combined, and flux calibrated moderate-resolution OSIRIS *K*-band spectra of VHS 1256 b. The errors are derived from the RMS of the individual spectra at each wavelength. Such as error includes uncertainties in both the continuum and the lines, the former of which 57

Figure 3.3: Our fully reduced, combined, and flux calibrated moderate-resolution OSIRIS *K*-band spectra of VHS 1256 b in black plotted alongside our best-fit model in pink. The residuals are shown below in gray. Even our custom *PHOENIX-ICM* had trouble fitting the continuum 61

Figure 3.4: Our OSIRIS continuum subtracted *K*-band spectra in black plotted against our MCMC best-fit model in magenta. The bump in the center of the spectrum between 2.1 and 2.2 μm is due to residual telluric. By removing the continuum, we remove uncertainties that were tied to the continuum . . 62

Figure 3.5: Corner plot from our MCMC fits for our continuum subtracted OSIRIS *K*-band spectra. The diagonal shows the marginalized posteriors. The covariances between all the parameters are in the corresponding 2-d histograms. The blue lines represent the 50 percentile, and the dotted lines . . 72

Figure 3.6: Our fully reduced, combined, and flux calibrated moderate-resolution OSIRIS K-band spectra of VHS 1256 b in black, plotted alongside our best fit model with two different grain sizes, 3μm in gray and 0.5μm in pink, and spectra from Miles et al. (2018) in blue, spectra from 73

Figure 3.7: Results of $T_{\rm eff}$ = 1240 K, $\log g$ = 3.25, $\log P_{cloud}$ = 6, and grain size = 3 μm model fits with varying mole fractions for both H_2O, CO, and CH_4 to our continuum-subtracted OSIRIS spectrum. The mole fractions are given in units relative to the ratio in the Sun, such that a value of zero implies the . 74

Figure 3.8: **Left:** The results of our χ^2 analysis on the first half of our continuum subtracted OSIRIS data. The CO abundances vary minimally during this analysis because of the lack of CO lines in the first half of our spectra. The best-fit water is still subsolar, with the lowest χ^2 values not including solar. 75

Figure 3.9: Our fully reduced, combined, and continuum subtracted moderate resolution OSIRIS K-band spectra of VHS 1256 b plotted alongside three models of T=1240 K and $\log g$=3.2 with varying C/O. The top panel shows the super-solar H_2O model with C/O=0.0142 in blue. The middle panel 76

Figure 4.1: An example data cube image frame, collapsed in wavelength via median, from our OSIRIS HD 284149 b dataset. The field of view is 0.32″ x 1.28″. The bright spot shows the companion clearly visible without any need for speckle removal. 81

Figure 4.2: Our fully reduced, combined, and flux calibrated, moderate-resolution OSIRIS K-band spectra of HD 284149 b. The errors are calculated from the RMS of the individual spectra at each wavelength. The error includes uncertainties in both the continuum and the lines. The total spectral 82

Figure 4.3: Our fully reduced, combined, and flux calibrated moderate-resolution OSIRIS K-band spectra of HD 284149 b in black plotted against the best-fit model in orange. The residuals are plotted below in gray. 84

Figure 4.4: Corner plot from our MCMC fits for our continuum OSIRIS K-band spectra. The diagonal shows the marginalized posteriors. The covariances between all the parameters are in the corresponding 2-d histograms. The blue lines represent the 50 percentile, and the dotted lines represent the 16 and 84 . . 93

Figure 4.5: Our fully reduced, combined, and continuum subtracted moderate resolution OSIRIS K-band spectra of HD 284149 b in black plotted against the best-fit model in orange. The residuals are plotted below in gray. 94

Figure 4.6: Corner plot from our MCMC fits for our continuum subtracted OSIRIS K-band spectra. 95

Figure 4.7: Results of $T_{\rm eff} = 2469^{+25}_{-26}$ K, $\log g = 4.58^{+0.26}_{-0.31}$, and $M/H = 0.57^{+0.26}_{-0.24}$ model fits with varying abundances for both C and O to our continuum-subtracted OSIRIS spectrum. The abundances are given in units relative to the ratio in the Sun, such that a value of zero implies the solar value. The scalings of 96

Figure 4.8: The best-fit model from the χ^2 results with a C of 1.25×Solar and a O of Solar. The model is plotted in blue, the data are in black, and the residuals are shown below in gray. 97

Figure 4.9: Population of 25 retrieval exoplanets in blue and 9 directly imaged planets in magenta. Here are their C/O ratios plotted against the companion masses in $M_{\rm Jup}$. There appear to be two groupings of planets, one with masses below 4 $M_{\rm Jup}$ and one with masses greater than or equal to 4 $M_{\rm Jup}$, which . 98

Figure 4.10: Population of 25 retrieval exoplanets in blue and 9 directly imaged planets in magenta. Here are their C/O ratios plotted against their projected separation in au from their host star/system. This plot most likely illustrates the detection bias in separation between the two populations. 99

Figure 4.11: Population of 25 retrieval exoplanets in blue and 9 directly imaged planets in magenta. Here are their C/O ratios plotted against the host star masses in $M_\odot$. There seems to be no visible correlation between these parameters. 100

Figure 4.12: Population of 25 retrieval exoplanets in blue and 9 directly imaged planets in magenta. Here are their C/O ratios plotted against the system age in Myr. This most likely illustrates the differences in the two populations, with the directly imaged planets being younger because they are more luminous . . 101

Figure 4.13: A histogram of p values from the KS Test and significance values from the AD Test. The results seem to show that both p values and significance values are less than 1% indicating that the two populations were distinct and not from the same underlying population. 102

Figure 5.1: Simulated data cube slices for our planned NIRSpec IFU pointing. Both companions are obvious at all wavelengths even before PSF subtraction. This hybrid simulation was generated by combining ETC simulated cubes containing the planets plus a diffractive model for light from the star 106

Figure 5.2: Simulated PHOENIX model spectra for TYC 8998 b at three different surface gravities. 107

Figure 5.3: Current and proposed data for TYC8998 b and c, including photometry (Bohn et al., 2020b,a), and a recent R$\sim$ 5000 spectrum in K-band from SINFONI for TYC8998 b. Simulated examples of the data expected are shown with dotted lines, demonstrating the massive increase 109

LIST OF TABLES

Table 2.1: OSIRIS Observations of κ Andromedae b 14

Table 2.2: Summary of atmospheric parameters derived from MCMC fits. 21

Table 2.3: κ And b RV estimates summary. 30

Table 2.4: Final RVs for κ Andromedae b. 30

Table 2.5: Derived orbit parameters for κ And B. 46

Table 3.1: Summary of VHS 1256 AB b System 58

Table 3.2: Summary of atmospheric parameters derived from MCMC fits for the Primary. 60

Table 3.3: Summary of atmospheric parameters derived from MCMC fits. 66

Table 4.1: Log of two non-detected planets observed for the Imaging Spectroscopy Survey of Exoplanetary Atmospheres with Keck/OSIRIS. 87

ACKNOWLEDGEMENTS

First, I would like to thank my advisor, Professor Quinn Konopacky for being an amazing role model. I was a non-traditional PhD student, and she supported and fought for me throughout the many obstacles that came up along my path to becoming an astronomer. When I needed to move home to assist my family in Maryland, Quinn put me in contact with Doctor Marshall Perrin at Space Telescope Science Institute in Baltimore who became my co-advisor, ensuring that I could continue my graduate research. She made it possible for me to finish courses remotely, which was unheard of pre-pandemic, by setting up her laptop in my lectures so I could sit in on them via Zoom. It was truly an honor to be Quinn's first graduate student, and I, my family, and friends are forever grateful for her.

I would also like to thank my co-advisor, Doctor Marshall Perrin. The ability to be at Space Telescope throughout the Cycle 1 proposal season and successful launch of the James Webb Space Telescope (JWST) was pertinent to the direction my post-PhD career will take. Marshall supported and encouraged me to lead a successful JWST Cycle 1 Program with a team of over 20 astronomers from around the world. I learned so much from him. I never thought I could do things he showed me I could do.

I also thank the other members of my committee - Adam Burgasser, Alison Coil, James Day, and Raphael Flauger. They have all given me great advice, have taught excellent courses, and have supported me in my non-traditional journey through out my PhD.

I would like to acknowledge Doctor Chris Theissen, who stepped in as an advisor for me when needed guidance. I could never ask a "dumb" question, and he encouraged me to keep going every chance he had when I needed it most. I would also like to extend an acknowledgement to Doctors Jean-Baptiste Ruffio, Emily Rickman, and Isa Rebollido for mentoring me as I completed my PhD.

I would like to acknowledge my undergraduate Professors - James Overduin, Parviz Gavamian, Thomas Krause, David Schaefer, Raj Kolagani, and Jennifer Scott - for their support when transitioning from a dance major to a physics major. They paved the way for my success

and provided a nurturing environment that I will never forget. Even after I graduated, they invited me to come back as an adjunct faculty member and continued to help and support me through my PhD.

I also thank my undergraduate physics tutor, Doctor Randy Tompkins, who truly made all of this possible. Without his help every Saturday morning throughout my undergraduate career, I would not have been able to catch up to my peers.

I also acknowledge the immense support from my parents, Elaine and Keith Wilcomb, for who never doubted me and gave everything they could so that I could pursue my dream.

I also thank my Uncle Drew Lowry, who has always been there for me and knew I would do great things.

I would also like to thank my husband, Jeffrey Hoch, for believing in me and helping me with my Python coding skills.

I would like to thank my friends and loved ones for their steadfast support throughout my PhD - Vinita Thakkar, Allison Cochrane, Shelby Davis, Seth Aulton, Heidi Petersen, Joel Richey, and Melissa St. James.

I would like to thank the referee, Joe Carson, for reviewing Chapter 2, and Marshall Perrin and Justin Otor for their helpful conversations relating to this work. K. K. W. H. would also like to thank Thea Kozakis and Laura Stevens for discovering κ And b. J.-B. R. acknowledges support from the David & Ellen Lee Prize Postdoctoral Fellowship. Work conducted by Laci Brock and Travis Barman was supported by the National Science Foundation under Award No. 1405504. Support for this work was provided by NASA through the NASA Hubble Fellowship grant HST-HF2-51447.001-A awarded by the Space Telescope Science Institute, which is operated by the Association of Universities for Research in Astronomy, Inc., for NASA, under contract NAS5-26555.

I also thank the observing assistant John Pelletier and support astronomer Jim Lyke for their help obtaining observations of VHS 1256 b. K.K.W.H., Q.M.K, T.S.B, and L.S.B. acknowledge the support by the National Aeronautics and Space Administration under the

Grants/Contracts/Agreements No.NNX17AB63G and 80NSSC21K0573 issued through the Astrophysics Division of the Science Mission Directorate. T.S.B. also acknowledges support by the National Science Foundation under Grant No. 1614492. Any opinions, findings, and conclusions or recommendations expressed in Chapter 3 are those of the author(s) and do not necessarily reflect the views of the National Aeronautics and Space Administration. The data presented herein were obtained at the W. M. Keck Observatory, which is operated as a scientific partnership among the California Institute of Technology, the University of California and the National Aeronautics and Space Administration. The Observatory was made possible by the generous financial support of the W. M. Keck Foundation. The authors wish to recognize and acknowledge the very significant cultural role and reverence that the summit of Maunakea has always had within the indigenous Hawaiian community. We are most fortunate to have the opportunity to conduct observations from this mountain.

Portions of this work were conducted at the University of California, San Diego, which was built on the unceded territory of the Kumeyaay Nation, whose people continue to maintain their political sovereignty and cultural traditions as vital members of the San Diego community.

Chapter 2, in full, is a reproduction of the material as it appears in The Astronomical Journal 2020, Hoch, K. K. W., Konopacky, Q. M., Barman, T. S., Theissen, C. A, Ruffio, J.-B., Brock, L., Macintosh, B., Marois, C., 160, 207.

Chapter 3, in full, has been accepted and is in preparation for publication of the material as it may appear in The Astronomical Journal, 2022, Hoch, K. K. W., Konopacky, Q. M., Barman, T. S., Theissen, C. A, Brock, L., Perrin, M. D., Ruffio, J.-B. Macintosh, B., Marois, C. I (the dissertation author) was the primary investigator and author of both these publications.

VITA

2016	B.S., Physics, Towson University
2016-2022	Graduate Student Researcher Center for Astrophysics and Space Sciences, University of California San Diego
2018–2022	Visiting Scientist, Space Telescope Science Institute
2018–2022	Adjunct Faculty, Towson University
2019	M.S., Physics, University of California San Diego
2022	Ph.D., Physics, University of California San Diego

PUBLICATIONS

Hoch, K. K. W., Konopacky, Q. M., Barman, T. S., Theissen, C. A., Brock, L., Ruffio, J.-B., Perrin, M., Macintosh, B., Marois, C., 2022,"Moderate-Resolution *K*-Band Spectroscopy of the Substellar Companion VHS 1256 b", AJ, accepted

Hoch, K. K. W., Konopacky, Q., Perrin, M., Barman, T., Bonnefoy, M., Chauvin, G., D'Oraziz, V., De Rosa, R. J., Girard, J., Gonzales, E., Luna, J. L., Macintosh, B., Morley, C., Petrus, S., Rameau, J., Ren, B., Rickman, E., Ruffio, J.-B., Theissen, C., Ward-Duong, K., 2021, "Direct Imaging Spectroscopy of two Jovian Exoplanets: Characterization of the TYC 8998-760-1 Multi-Planetary System", JWST Proposal. Cycle 1, 2044

Wilcomb, K. K., Konopacky, Q. M., Barman, T. S., Theissen, C. A., Ruffio, J.-B., Brock, L., Macintosh, B., Marois, C., 2020,"Moderate-resolution K-band Spectroscopy of Substellar Companion κ Andromedae b", AJ, 160, 207

Ruffio, J.-B., Konopacky, Q. M., Barman, T., Macintosh, B., **Hoch, K. K. W.**, De Rosa, R. J., Wang, J. J., Czekala, I., Marois, C., 2021, "Deep exploration of the planets HR 8799 b, c, and d with moderate resolution spectroscopy", arXiv:2109.07614

Ruffio, J.-B., Macintosh, B., Konopacky, Q.M., Barman, T., De Rosa, R. J., Wang, J. J., **Wilcomb, K. K.**, Czekala, I., Marois, C., 2019, "Radial Velocity Measurements of HR 8799 b and c with Medium Resolution Spectroscopy", AJ, 158, 200

ABSTRACT OF THE DISSERTATION

Moderate Resolution Spectroscopy of Directly Imaged Exoplanets

by

Kielan Kathryn Wilcomb Hoch

Doctor of Philosophy in Physics

University of California San Diego, 2022

Quinn Konopacky, Chair

This thesis is part of larger survey conducted using the OSIRIS IFU on the W. M. Keck Telescope to directly image exoplanets. I begin this publication with an overview of direct detection and characterization of exoplanets, the current key scientific questions plaguing the field such as the formation of these objects and how they are distinct from low-mass brown dwarfs, and my contributions using OSIRIS. OSIRIS is an ideal instrument for this type of imaging; an integral field spectrograph (IFU) allows us to distinguish scattered starlight and speckle artifacts from the planet itself. OSIRIS observations of directly imaged planets have greatly improved our understanding of their atmospheres, hinted at formation pathways, and, with sufficient SNR, can reveal individual molecular lines.

The three substellar companions were observed, spectrally extracted, and atmospherically characterized with OSIRIS in K-band ($\sim$2.2 μm) – κ And b, VHS 1256 b, and HD 284149 b. The R$\sim$4,000 spectra were analyzed via a forward modeling framework with custom PHOENIX atmosphere models and Husser et al. (2013) models. This framework allowed for the derivation of effective temperatures, surface gravities, metallicities, and carbon and oxygen abundances. In particular, the C/O ratio was derived for each source as a possible formation tracer diagnostic.

Finally, this thesis analyzed the C/O ratio formation tracer. Directly imaged planets remain a mystery for the two main formation pathways–core accretion/pebble accretion. It was believed an elevated C/O ratio would point towards formation via core accretion, and a stellar C/O ratio would insinuate formation through gravitational instability. The C/O ratios of the planets in this thesis, as well as the C/O ratios from other works show that all directly imaged planets have stellar C/O. A small fraction of transit/eclipse planets also have derived C/O ratios, thus they were compared to the directly imaged planet C/O ratios against various system parameters. A trend was revealed between companion mass and the C/O ratio, which showed that there may be two distinct populations of exoplanets with possible different formation mechanisms. This thesis expresses a need for new formation diagnostics, a more in depth study into why the directly imaged planet population have the same C/O ratios, and more analyses that span across the different exoplanet populations.

Chapter 1

Introduction

Exoplanets provide an exciting laboratory to answer many questions: How did our Solar System form and evolve? What is the diversity of planetary systems? and What planetary parameters are needed to host life and check for biosignatures? The majority of exoplanets known today were discovered by indirect methods such as measuring the periodic dip in brightness of a star (transit method) and the sinusoidal trend in radial velocity of a star (radial velocity method). The only method that directly detects the light from these substellar companions that is completely free from host starlight is direct imaging. Each of these methods are sensitive to distinct populations of exoplanets as shown in Figure 1.1 using data from the NASA Exoplanet Archive[1].

Direct imaging challenges include removing/blocking the starlight from the host star to reveal the companion. Figure 1.2 shows that younger substellar objects are brighter, and therefore, easier to detect. Thus, the directly detected planets are young, self-luminous gas giants detected in thermal emission. Also, because of the brightness of the host stars, we are more sensitive to objects that orbit at moderate to wide separations ($\sim$10–250 au; Rameau et al. 2013; Biller et al. 2013; Galicher et al. 2016; Nielsen et al. 2019; Vigan et al. 2021). These young, bright, and widely separated substellar objects are unique compared to the indirectly detected exoplanets (Fig 1.1). Directly imaged planets also span the mass range into brown dwarf regime with masses of 2 M_{Jup} or more, so they can uniquely constrain our understanding of planet

[1] https://exoplanetarchive.ipac.caltech.edu

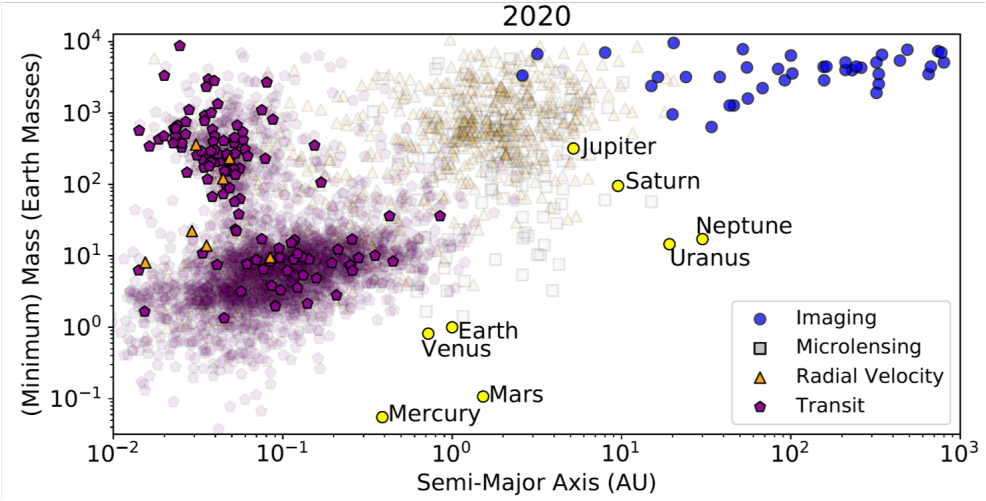

Figure 1.1: The demographics of planetary-mass companions detected via various methods. Bold symbols denote companions with spectroscopic measurements and atmospheric characterization. The directly imaged companions are dominant in this population. This figure was created by Dmitry Savransky, using data from the NASA Exoplanet Archive (Johnston et al., 2022).

formation distinct from star formation. Direct imaging spectroscopy provides access to the photons from the planet itself, allowing for atmospheric characterization to probe temperature, clouds, chemistry, gravity, and possible formation pathways.

The first direct images and spectra of planets relied on adaptive optics (AO) systems that deblur starlight (Chauvin et al., 2004) or space telescopes like the Hubble Space Telescope with the use of coronagraphs (Kalas et al., 2008). Many facilities such as the Very Large Telescope (VLT), the W. M. Keck Telescope, and the Gemini South telescope are outfitted with AO and coronagraphs and have been used to image many of the directly imaged planets (e.g., Chauvin et al. 2004; Marois et al. 2008; Macintosh et al. 2014). The first image of a planetary mass object was 2MASS 1207 b around a 25 M_{Jup} brown dwarf (Chauvin et al., 2004). The nature of this object started to raise questions about whether this companion should be considered a brown dwarf or a planet (Mohanty et al., 2007; Mamajek & Meyer, 2007). The mass ratio of the companion to the star was $>$0.16, which is quite large compared to planets around main sequence stars.

The most famous directly imaged planetary system was imaged using the Keck and

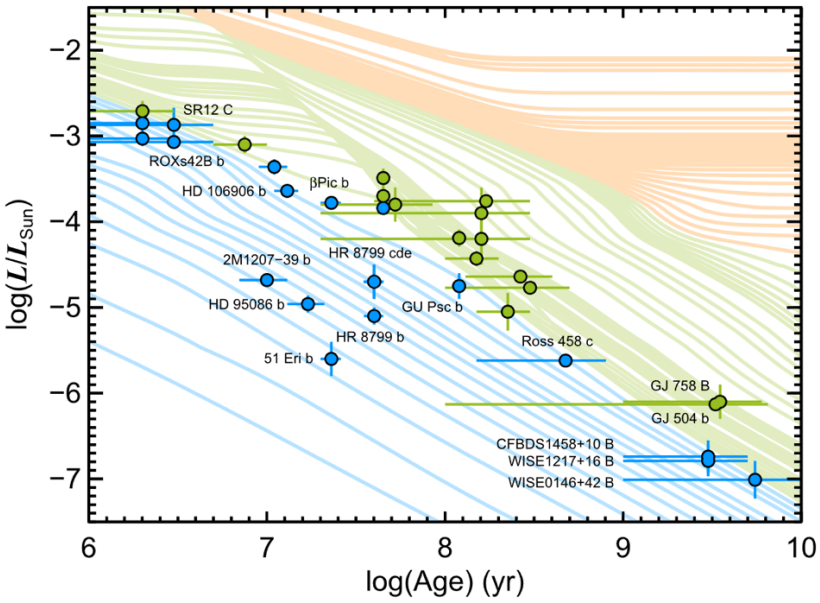

Figure 1.2: Cooling tracks for planets, brown dwarfs and stars. Each curve is at a constant mass. Typically today we are sensitive to planets around stars younger than 100 Myr old (Bowler, 2016). The orange lines denote objects greater than 80 M_{Jup}, the green lines denote objects 14-80 M_{Jup}, and the blue lines denote objects less than 14 M_{Jup}.

Gemini Telescopes in 2008. The HR 8799 system includes 4 companions with semi-major axes ranging from 15 au to 70 au and a 30 Myr A5-type host star (Marois et al., 2008, 2010). How these planets formed is still a mystery, given their separations and masses.

Currently, from the NASA Exoplanet Archive, there are about 50 substellar companions that have been discovered via direct imaging. There are many discovered objects that are, by consensus, planets (i.e., HR 8799 bcde, β Pic b, 51 Eri b, etc), but again the exact criteria to distinguish them from brown dwarfs is still unclear. The working definition by the International Astronomical Union (IAU) is a cutoff at 13 M_{Jup}, the deuterium burning limit, but this criteria does not account for the evolution of low mass objects (Chabrier & Baraffe, 2007; Luhman et al., 2008). Some objects below the deuterium burning limit have been found in configurations that suggest formation via cloud fragmentation, or forming like a star, and other objects above this limit have been found in configurations that imply they formed from a protoplanetary disk, like a planet (Todorov et al., 2010; Liu et al., 2013).

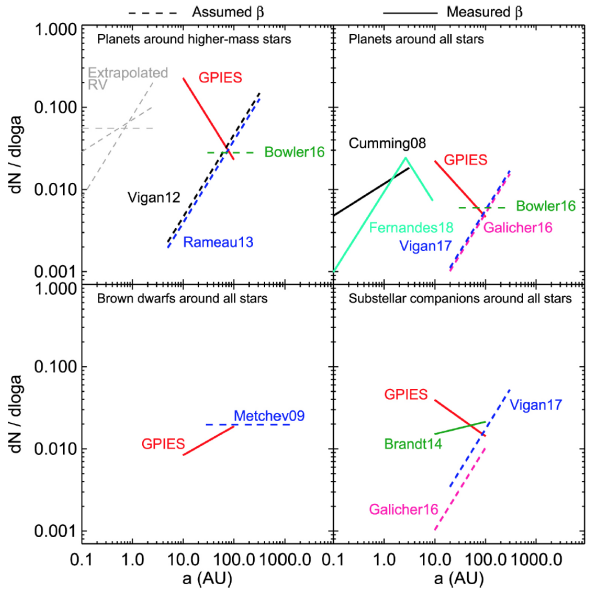

Figure 1.3: Comparison of the occurrence rates from the GPIES and other surveys of 5–13 M_{Jup} planets **(top two panels)**, 13–80 M_{Jup} brown dwarfs **(bottom left)**, and 5–80 M_{Jup} substellar companions **(bottom right)** as a function of semimajor axis. Only higher-mass stars from GPIES were considered for one panel **(top left panel)**, while all 300 stars were used in the other panels. The slope of the lines is the value β, the semimajor axis power-law index, and the normalization showing the planet occurrence rate (Nielsen et al., 2019).

There have been many direct imaging surveys to attempt to uncover more of these objects and to learn more about this population of exoplanets. Nielsen et al. (2019) conducted a survey on the first 300 stars observed by the Gemini Planet Imager Exoplanet Survey (GPIES) and found that stars that were more massive than 1.5 $M_{\odot}$ are more likely to host planets/companions between 2–13 M_{Jup} and semi-major axis between 3–100 au, and that there was a low occurence rate of brown dwarfs (13–80 M_{Jup}) around all stars between 10–100 au (Fig 1.3). They also found that giant planets favor smaller semi-major axes consistent with 1–10 au, a similar result found with radial velocity, while the brown dwarfs exhibited the opposite trend. Vigan et al. (2021) conducted a 500-star survey performed with SPHERE on the Very Large Telescope and found the frequencies of systems with at least one substellar companion to be $23.0^{+13.5}_{-9.7}$, $5.8^{+4.7}_{-2.8}$, and $12.6^{+12.9}_{-7.1}$ % for BA, FGK, and M stars. Both results show that the directly imaged substellar companion population may show different formation pathways for brown dwarfs and gas giant

planets.

In order to shed more light on how these objects formed, we need access to spectral information, which direct imaging provides. Spectral characterization of these objects allow for derivation of atmospheric parameters such as effective temperature, surface gravity, metallicity, and molecular abundances. Integral Field Spectrograph (IFS) instruments have provided low (R$\sim$20–80) and moderate (R$\sim$2000–6000) resolution spectra in the near-IR (1-2.5μm) such as P1640, SPHERE, GPI, SCExAO-CHARIS in combination with extreme AO systems and Gemini/NIFS, VLT/MUSE and SINFONI, Keck/OSIRIS in combination with standard AO modules. Low resolution near-IR data can help constrain H_2O spectral indices that can point towards what spectral type these objects are and low resolution H-band continuum data are gravity sensitive (Allers & Liu, 2013). Moderate resolution near-IR data shows fainter and narrower molecular bands (FeH, CO), and spectral lines (Na I, K I) that are sensitive to surface gravity and chemical composition of the substellar companions (i.e. C/O ratio and metallicity). These measurements are essential to understanding this unique population of exoplanets.

1.0.1 Formation Tracers

Directly imaged planets are massive and widely separated from their host stars as stated above. They remain a mystery for the two main formation scenarios posed for these objects– core/pebble accretion (e.g. Safronov & Zvjagina 1969; Goldreich & Ward 1973; Hayashi et al. 1985; Pollack et al. 1996) and gravitational/disk instability (e.g. Kuiper 1951; Cameron 1978). Core accretion involves the formation of a rocky core through the coagulation of planetesimals until it is massive enough to accrete a gaseous envelope that is later followed by a phase of rapid gas accretion. But, the directly imaged companions orbit at a distance that is too large for core accretion models to create massive planets (Dodson-Robinson et al. (2009)). Pebble accretion can be more efficient than conventional core accretion, but a very high concentration of pebbles is required to create gas giants far from their host stars (Johansen & Lambrechts, 2017). Gravitational/disk instablity involves unstable disk fragments collapsing to form gravitationally-

bound fragments that will go on to become gaseous planets. But, if a disk-instability process occurred and was very efficient, it would produce a large population of brown dwarf companions around similar host stars at large separations, which has not been seen by many massive surveys (Kratter et al., 2010; Rameau et al., 2013; Biller et al., 2013; Galicher et al., 2016). There are some other mechanisms that can aid in explaining wide orbit planet properties using these theories such as planetary migration (Goldreich & Tremaine, 1980; Lin & Papaloizou, 1986). Gas giant planets can cause torques in the protoplanetary disk that are strong enough to clear a gap in the disk at their respective orbits (Ward, 1997). Once the gap forms, the planet's orbital evolution is tied to the disk and the planet will migrate at the same rate as the gas that moves through the disk (Chambers, 2009). This can help relocate gaseous planets to the separations that we see in observations, but the degree of migration required varies planet to planet. Migration history can also affect the composition of exoplanetary atmospheres (Cridland et al., 2020). For example if a planet does not migrate inside of the ice line before accreting gas, the gas will have more carbon because water will still be in its ice phase (Cridland et al., 2019). To reveal elemental abundances of these widely separated companions, we need a detailed understanding of chemical and dynamical evolution of the giant planets' atmospheres.

Detailed abundance measurements for specific species, such as oxygen, have been challenging for the planets in our own Solar System. The ratio of the abundances of carbon and oxygen (C/O) in a Jovian planet atmosphere has been suggested as a potential way to trace the formation location and formation mechanism (e.g., Madhusudhan et al. 2011). An in depth understanding of chemical and dynamical histories of the giant planets' atmospheres is required to estimate these elemental abundances. The luminosity and effective temperature of Jovian planets decrease with time, causing their atmosphere to undergo changes. The composition of their atmospheres could be further altered by continued accretion of solid bodies from the planetary disk, or by mixing inside the metal-rich core (e.g., Mousis et al. 2009). For Saturn, only upper limits on the C/O ratio have been measured (Wong et al., 2004; Visscher & Fegley, 2005). For Jupiter, Li et al. (2020) used Juno data and measured the H_2O abundance in the

equatorial zone as $2.5^{+2.2}_{-1.6}$ x 10^3 ppm. This suggests an oxygen abundance of roughly three times the Solar value. The young, and bright directly imaged planets offer an exciting opportunity for pursuing detailed chemical abundances, as they have not undergone as many complex changes in composition as their older Solar System counterparts.

Elemental abundance ratios such as the C/O ratio are fundamental parameters of gas giant exoplanet atmospheres and their host stars' protoplanetary disks (e.g, Madhusudhan 2019; Cridland et al. 2020). The C/O ratio, in particular, is considered a key formation tracer for how these objects formed and where they formed in their protoplanetary disk. The C/O ratio is a function of location of snowlines and abundances of H_2O, CO_2, and CO relative to the H_2 abundance in the disk as shown in Figure 1.4 (Piso et al., 2015). Öberg et al. (2011) analytically calculated that the C/O ratio is expected to be on order unity, or enhanced compared to the stellar value, between the CO_2 and CO snowlines because oxygen is depleted. Expanding upon the C/O ratio property of disks and companions, particle size and pebble drift are now shown to affect the C/O ratio because the C/O ratio is mainly reliant on the snowline location for the particle size hosting the mass in ice (Piso et al., 2015; Öberg & Bergin, 2016).

More recent studies have suggested that pressure bumps, areas in the protoplanetary disk where large dust grain congregate due to gas-grain drag forces (Birnstiel et al., 2010), are associated with giant planets and that the accretion they endure will be composed of the gaseous material at the location of the bump (e.g. Pinilla et al. 2021; van der Marel et al. 2016). The discovery of low a C/O at the location of an asymmetric dust trap around Oph IRS 48 may indicate that these pressure bumps could have a key role in regulating the C/O ratio profile of planet forming disks (Booth et al., 2021). van der Marel et al. (2021) found a correlation between the presence of a significant CO-icy dust reservoir and high C_2H emission, which illustrates the regulation of the C/O profile in the protoplanetary disk by pressure bump locations and the CO snowline. This signifies a need to include dust transport in chemical disk models, for better interpretations of exoplanet atmospheric compositions.

Other factors will affect the ratio as well such as planet formation, chemical evolution,

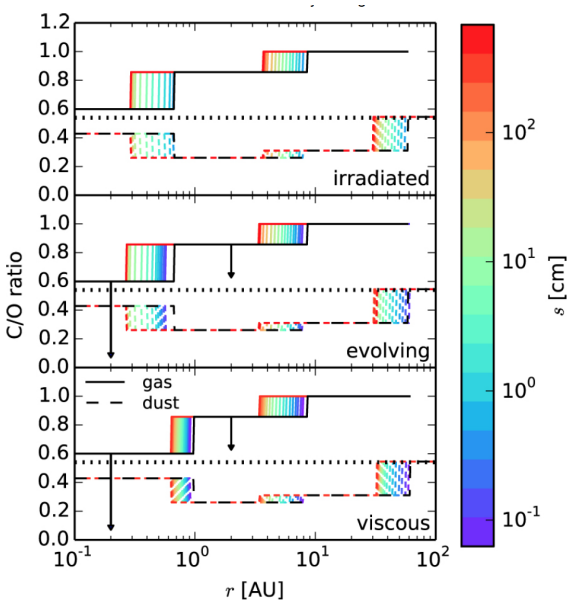

Figure 1.4: Estimated C/O ratios in gas (solid lines) and in dust (dashed lines) for an irradiated disk (top panel), an evolving disk (middle panel) and a viscous disk (bottom panel). The particle size increases from 0.05 to 700 cm shown by the color bar to the right. The horizontal dotted line represents the stellar value of 0.54. The arrows indicate the movement of CO_2 gas inside the CO_2 snowline, and of CO_2 and H_2O gas inside the H_2O snowline and therefore, due to gas accretion, this will increase the amount of oxygen gas inside the snowlines and reduce the gas C/O ratio (Piso et al., 2015).

and physical evolution of protoplanetary disks. Migration of planets on a shorter timescale than the planet growth can cause a wide range of chemical compositions (Cridland et al., 2020). Theoretical (Morbidelli et al. 2014; Batygin 2018) and observational (Szulágyi et al., 2014) evidence shows that the accretion is mostly vertical, so the gas falls from one to three scale heights rather than the midplane in the disk (Teague et al., 2019). Cridland et al. (2020) shows that the C/O ratio does vary slightly when considering accretion from the midplane versus accretion from larger scale heights, but further modeling is needed for the chemical evolution of the gas above the midplane. Current studies are incorporating more chemical and physical processes into models to get a better idea of what impacts the C/O ratio and what exactly the ratio tells us about formation.

1.0.2 An Imaging Spectroscopy Survey of Exoplanetary Atmospheres with Keck/OSIRIS

An advantage of direct imaging of exoplanets is that they can be characterized spectroscopically. Some of the most detailed spectra of extrasolar planets have been obtained using OSIRIS on the W.M. Keck I telescope (Konopacky et al., 2013; Barman et al., 2015; Ruffio et al., 2019, 2021; Wilcomb et al., 2020; Hoch et al., 2022) OSIRIS observations of directly imaged planets have greatly improved our understanding of their atmospheres, hinted at formation pathways, and, with sufficient SNR, can reveal individual molecular lines. OSIRIS is an ideal instrument for this type of imaging; an integral field spectrograph (IFU) allows us to distinguish scattered starlight and speckle artifacts from the planet itself. The impact of the speckles primarily affects the continuum of the imaged planet spectra, but they do not mask narrow spectral lines. Therefore, we can examine the spectra at the full resolution (R$\sim$4000) that OSIRIS has to offer. These data show an immense suite of molecular lines that can, in turn, be used to measure abundances and C/H and O/H ratios. These abundance ratios are potentially useful as diagnostics for formation mechanisms (e.g., Öberg et al. 2011). C/O ratios that are consistent with the values of the host star could point towards formation via gravitational instability, while C/O ratios $\sim$1 may indicate core accretion formation.

Chapter 2 analyzes the first planet in the survey, κ And b, and determines an effective temperature, surface gravity, metallicity, and C/O ratio. Chapter 3 analyzes the second substellar companion in the survey, VHS 1256 b, and measures an effective temperature, surface gravity, cloud parameter, and C/O ratio. Chapter 4 analyzes the third companion, HD 284149 b, and obtains an effective temperature, surface gravity, metallicity, and C/O ratio. Chapter 4 contains a statistical analysis of the C/O ratio as a formation tracer for directly imaged planets and companions against transit discovered planets. And, Chapter 5 is a summary and describes future work.

Chapter 2

Moderate-Resolution K-Band Spectroscopy of Substellar Companion κ Andromedae b

We present moderate-resolution ($R \sim 4000$) K band spectra of the "super-Jupiter," κ Andromedae b. The data were taken with the OSIRIS integral field spectrograph at Keck Observatory. The spectra reveal resolved molecular lines from H_2O and CO. The spectra are compared to a custom *PHOENIX* atmosphere model grid appropriate for young planetary-mass objects. We fit the data using a Markov Chain Monte Carlo forward modeling method. Using a combination of our moderate-resolution spectrum and low-resolution, broadband data from the literature, we derive an effective temperature of $T_{\rm eff}$ = 1950 - 2150 K, a surface gravity of $\log g = 3.5-4.5$, and a metallicity of [M/H] $= -0.2-0.0$. These values are consistent with previous estimates from atmospheric modeling and the currently favored young age of the system (<50 Myr). We derive a C/O ratio of $0.70^{+0.09}_{-0.24}$ for the source, broadly consistent with the solar C/O ratio. This, coupled with the slightly subsolar metallicity, implies a composition consistent with that of the host star, and is suggestive of formation by a rapid process. The subsolar metallicity of κ Andromedae b is also consistent with predictions of formation via gravitational instability. Further constraints on formation of the companion will require measurement of the C/O ratio of κ Andromedae A. We also measure the radial velocity of κ Andromedae b for the first time, with a value of $-1.4 \pm 0.9\,{\rm km\,s^{-1}}$ relative to the host star. We find that the derived radial velocity is consistent with the estimated high eccentricity of κ Andromedae b.

2.1 Introduction

The new era of direct imaging of exoplanets has revealed a population of Jupiter-like objects that orbit their host stars at large separations ($\sim$10–100 AU; Bowler 2016; Nielsen et al. 2019; Vigan et al. 2021). These giant planets, with masses between $\sim$2–14 $M_{\rm Jup}$ and effective temperatures between $\sim$500–2000 K, are young ($\sim$15–200 Myr) compared to exoplanets discovered through other methods (e.g., Doppler spectroscopy, transit, gravitational microlensing) because their detectability is enhanced at young ages (e.g., Baraffe et al. 2008). The formation of these gas giant planets has traditionally been challenging for the two main planet formation models, core (or pebble) accretion and gravitational instability (e.g., Dodson-Robinson et al. 2009).

Some planet formation scenarios influence a planet's final atmospheric composition more than others. A potential connection between formation and composition highlights the importance of studying the properties of exoplanet atmospheres. It has long been suggested that the compositions of giant planets in our Solar System were likely determined by their initial location in the protoplanetary disk and the accretion they experienced (e.g., Owen et al. 1999). For example, the ratio of the abundances of carbon and oxygen (C/O) in a Jovian planet atmosphere has been suggested as a potential way to trace the location and mechanism of formation (e.g., Madhusudhan et al. 2011). To estimate elemental abundances, however, we need a detailed understanding of chemical and dynamical histories of the giant planets' atmospheres. The luminosity and effective temperature of a giant planet decreases with time causing its atmosphere to undergo considerable changes even over a short period of time equal to the age of the directly imaged planet population, and certainly over a few billion years. In particular, the vertical mixing timescales will change as the planet's atmospheric dynamics evolve and as the radiative-convective boundary moves to higher pressures. Changes in temperature and pressure will also result in changes in the atmospheric abundances of gasses and condensates. The composition of their atmospheres could be further altered by continued accretion of solid

bodies from the planetary disk, or mixing inside the metal-rich core (e.g., Mousis et al. 2009). Important trace molecules (H_2O, CH_4, CO_2, CO, NH_3, and N_2) of giant planets are greatly impacted by these complex chemical and physical processes that occur over time (e.g., Zahnle & Marley 2014).

Because of these challenges, detailed abundance measurements for certain species, such as oxygen, have been challenging for the planets in our Solar System. For Saturn, only upper limits on the C/O ratio have been measured (Wong et al., 2004; Visscher & Fegley, 2005). For Jupiter, previous estimates of C/O were impacted by inconclusive findings on the water abundance in the atmosphere from the Galileo probe. Using Juno data, Li et al. (2020) recently measured the water abundance in the equatorial zone as $2.5^{+2.2}_{-1.6} \times 10^3$ ppm, suggesting an oxygen abundance roughly three times the Solar value. The directly imaged planets offer an interesting laboratory for pursuing detailed chemical abundances, as they have not undergone as many complex changes in composition as their older counterparts.

The κ Andromedae (κ And) system consists of a B9V-type host star with a mass of $\sim$2.7 $M_\odot$ and a bound companion, κ And b (Carson et al., 2013). This system is one of the most massive stars known to host an extrasolar planet or low-mass brown dwarf companion. κ And b has been described as a "super-Jupiter," with a lower mass limit near or just below the deuterium burning limit (Carson et al., 2013; Hinkley et al., 2013).

Zuckerman et al. (2011) proposed that κ And is a member of the Columba association with an age of $\sim$30 Myr, leading Carson et al. (2013) to adopt that age and estimate κ And b to have a mass $\sim$12.8 $M_{\rm Jup}$ with DUSTY evolutionary models (Chabrier et al., 2000). However, Hinkley et al. (2013) suggested that κ And b had a much older isochronal age of 220 $\pm$ 100 Myr, a higher surface gravity ($\log g \approx 4.33$ as opposed to $\log g \sim 4$ for 30 Myr), and a mass of 50^{+16}_{-13} $M_{\rm Jup}$ by comparing its low-resolution YJH-band spectra with empirical spectra of brown dwarfs. Bonnefoy et al. (2014) derived a similar age to Carson et al. (2013) of 30^{+120}_{-10} Myr based on the age of the Columba association and a lower mass limit of 10 $M_{\rm Jup}$ based on "warm-start" evolutionary models, but did not constrain the surface gravity. More recent studies

of κ And b by Currie et al. (2018) and Uyama et al. (2020) have concluded the object is low gravity ($\log g \sim 4$–4.5) and resembles an L0–L1 dwarf. Other studies focusing on the host star found the system to be young ($t \sim 30$–40 Myr; David & Hillenbrand 2015; **?**). Using CHARA interferometry, Jones et al. (2016) constrained the rotation rate, gravity, luminosity, and surface temperature of κ And A and compared these properties to stellar evolution models, showing that the models favor a young age, 47^{+27}_{-40} Myr, which agrees with a more recent age estimate of 42^{+6}_{-4} Myr for the Columba association by Bell et al. (2015).

Understanding the orbital dynamics of exoplanets can also put constraints on formation pathways. Radial velocity measurements can be used to break the degeneracy in the orientation of the planets' orbital plane. While astrometric measurements from imaging are ever increasing in precision (e.g., Wang et al. 2018b), measuring the radial velocity (RV) of directly imaged exoplanets is challenging due to the required higher spectral resolution balanced with their faintness and contrast with respect to their host stars. The first RV measurement of a directly imaged planet was β Pictoris b using the Cryogenic High-Resolution Infrared Echelle Spectrograph (CRIRES, R=100,000) at the Very Large Telescope (VLT; Kaeufl et al. 2004). An RV of -15.4 $\pm$ 1.7 km s^{-1} relative to the host star was measured via cross-correlation of a CO molecular template (Snellen et al., 2014). Haffert et al. (2019) detected Hα around PDS 70 b and c, but the radial velocities measured were of the accretion itself and not of the motion of the planets. Ruffio et al. (2019) measured the RV of HR 8799 b and c with a 0.5 km s^{-1} precision using a joint forward modeling of the planet signal and the starlight (speckles).

Here we present $R \sim 4000$ K-band spectra of κ And b. In Section 2.2 we report our observations and data reduction methods. In Section 2.3 we use atmosphere model grids and forward modeling Markov Chain Monte Carlo methods to determine the best-fit effective temperature, surface gravity, and metallicity of the companion. We use our best-fit parameters and *PHOENIX* models with scaled molecular mole fractions to derive a C/O ratio of $0.70^{+0.09}_{-0.24}$ for κ And b. In Section 2.4 we use the joint forward modeling technique devised by Ruffio et al. (2019) to measure κ And b's radial velocity and to constrain the plane and eccentricity of its

orbit. In Section 2.5 we discuss the implications of our results and future work.

2.2 Data Reduction

κ And b was observed in 2016 and 2017 with the OSIRIS integral field spectrograph (IFS) (Larkin et al., 2006) in the *K* broadband mode (1.965–2.381 μm) with a spatial sampling of 20 milliarcseconds per lenslet. A log of our observations is given in Table 2.1. Observations of a blank patches of sky and an A0V telluric standard (HIP 111538) were obtained close in time to the data. We also obtained dark frames with exposure times matching our dataset. The data were reduced using the OSIRIS data reduction pipeline (DRP; Krabbe et al., 2004; Lockhart et al., 2019). Data cubes are generated using the standard method in the OSIRIS DRP, using rectification matrices provided by the observatory. At the advice of the DRP working group, we did not use the Clean Cosmic Rays DRP module. We combined the sky exposures from each night and subtracted them from their respective telluric and object data cubes (we did not use scaled sky subtraction).

Table 2.1: OSIRIS Observations of κ Andromedae b

Date (UT)	Number of Frames	Integration Time (min)	Total Int. Time (min)
2016 Nov 6	5	10	50
2016 Nov 7	8	10	80
2016 Nov 8	5	10	50
2017 Nov 4	13	10	130

After extracting one-dimensional spectra for the telluric sources, we used the DRP to remove hydrogen lines, divide by a blackbody spectrum, and combine all spectra for each respective night. An initial telluric correction for κ And b was then obtained by dividing the final combined telluric calibrator spectrum in all object frames.

Once the object data cubes are fully reduced, we identify the location of the planet. The location can be challenging to find due to the brightness of the speckles even at the separation of

the planet ($\sim 1''$ separation). Speckles have a wavelength-dependent spatial position behavior, and the planet signal does not. In order to locate the planet, we visually inspect the cubes while stepping through the cube in wavelength, and determine which features do not depend on wavelength. Once we find the planet, we record the spatial coordinates.

During preliminary spectral extraction, we noted that the telluric frames did a poor job of correcting some absorption features, particularly in the blue part of the spectrum. We therefore used the speckles from κ And A that are present in all datacubes to derive a telluric correction spectrum for each individual exposure. This correction works well because κ And A is a B9 type star with very few intrinsic spectral lines, so the majority of the spectral features will be from Earths' atmosphere. We masked the location of the planet and extracted a 1-D spectrum from the rest of the datacube to use as the telluric spectrum. As with the A0V star, we removed the hydrogen lines and blackbody spectrum based on the temperature of κ And A.

Once the data cubes were reduced and planet location identified, we used a custom IDL routine to remove speckles. The program smooths and rebins the data to $\lambda/\Delta\lambda \sim 50$, and then magnifies each wavelength slice, λ, about the star by $\lambda m/\lambda$ with $\lambda m = 2.173$ μm, the median wavelength in the K-band. The generated data cube has speckles that are positionally aligned, with the planet position varying. The program then fits first order polynomials to every spatial location as a function of wavelength (Barman et al., 2011; Konopacky et al., 2013). We know the position of the planet, and use it to mask the planet to prevent bias in the polynomial fit. The results of the fits are subtracted from the full-resolution spectrum before the slices are demagnified. The resultant cube is portrayed in Figure 2.1 by showing one of the spaxels before and after the speckle removal.

Uncertainties were determined by calculating the RMS between the individual spectra at each wavelength. These uncertainties include contributions from statistical error in the flux of the planet and the speckles as well as some additional error in the blue end of the spectrum due to imperfect removal of large telluric features in this region. The OH sky lines are well-subtracted and have a negligible contribution to the uncertainties.

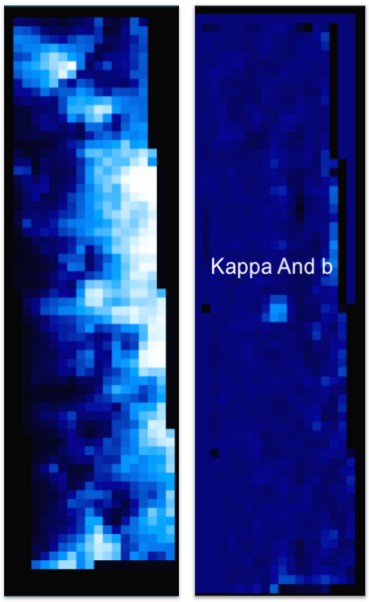

Figure 2.1: An example data cube image frame, collapsed in wavelength via median, from our OSIRIS κ And b data set. The panel on the left shows a reduced cube before speckle removal, demonstrating the brightness of the speckles at the location of κ And b. The right panel shows the data cube after the speckle removal process. The algorithm effectively removes the speckle noise, leaving most of the flux from the planet behind for spectral extraction.

We also tested our reduction methodology by planting a fake planet with a flat spectrum in each data cube and going through the same reduction process as above. When we ran the speckle subtraction and then extracted the fake planet spectra from each cube, there were some fluctuations in the spectra, particularly near the ends of the spectral range. We decided to test the speckle subtraction algorithm and extract the fake planet spectra using a higher order polynomoial fit, but the continuum fluctuations were much larger. We therefore determined that the first order polynomial fit introduces the least continuum bias to our data. The uncertainties from the extracted spectra incorporate most of the impact of this bias, with some residual impact at the blue and red ends. We mitigate the impact in further analysis through removal of the continuum (see Section 2.3.3).

Once the speckles are removed, we extract the object spectrum using a box of 3×3 spatial pixels (spaxels). Once we extracted the κ And b spectra from each frame for all data, we then normalize each individual spectrum to account for seeing and background fluctuations,

and we apply a barycentric correction to each spectrum. Finally, we median-combine all 30 individual spectra. To calibrate the flux of our spectra we calculated the flux at each wavelength such that, when integrated, the flux matches the K-band apparent magnitude (14.37 ± 0.07) from Currie et al. (2018). Figure 3.2 shows the combined, flux calibrated spectrum for κ And b.

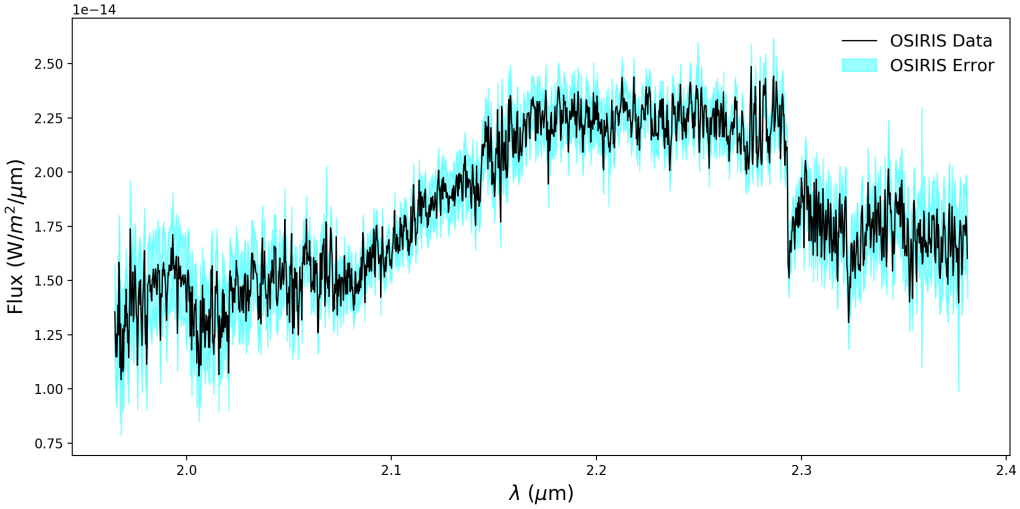

Figure 2.2: Our fully reduced, combined, and flux calibrated moderate-resolution OSIRIS K-band spectra of κ And b. The errors are shown as a shaded light blue region.

Once we had our fully reduced, combined, and flux calibrated spectra, we wanted to analyze the spectrum both with and without the continuum. The expectation is that by removing the continuum, some of the residual correlated noise from the speckles get removed as well. To remove the continuum, we apply a high-pass filter with a kernel size of 200 spectral bins to each of the individual spectra. Then we subtract the smoothed spectrum from the original spectra. Once all the individual spectra had been continuum subtracted we median combined them as well, and find the uncertainties by calculating the RMS of the individual spectra at each wavelength.

2.3 Spectral Modeling

2.3.1 Synthetic Spectra

Our first goal is to constrain the temperature, surface gravity, and metallicity of κ And b. In order to do this, we must construct a model grid that spans the expected values of these parameters. In a number of previous works on κ And b, the temperature was estimated to be $\sim$2000 K and the surface gravity ($\log g$) < 5 (e.g., Hinkley et al., 2013; Bonnefoy et al., 2014; Todorov et al., 2016; Currie et al., 2018; Uyama et al., 2020). The metallicity has not been constrained, but estimates from the host star suggest values near solar or slightly subsolar (Wu et al., 2011; Jones et al., 2016).

Based on these measurements, we generated a custom grid based on the *PHOENIX* model framework. The details on the computation of this grid are described in Barman et al. (2011, 2015), with the updated methane line list from Yurchenko & Tennyson (2014) and the optical opacities from Karkoschka & Tomasko (2010). The grid spans a temperature range 1500–2500 K, a $\log g$ range of 2–5.5 dex, and a metallicity range of -0.5–0.5 dex, which encompasses the range of values previously reported for κ And b. For a $\sim$2000 K object, the C is already in CO instead of CH_4 throughout the atmosphere, and thus the amount of CO should be constant with height. Therefore, for κ And b, we chose not to model vertical mixing (Kzz = 0).

The cloud properties for young gas giants and brown dwarfs are notoriously complex. In our modeling framework, we are able to incorporate clouds in several different ways. We can generate a thick cloud with an ISM-like grain size distribution (DUSTY, Allard et al. 2001), a complete lack of cloud opacity (COND, Allard et al. 2001), or an intermediate model that spans these two extremes (ICM, Barman et al. 2011). Given the estimated temperature and surface gravity of κ And b, we chose to use a (*DUSTY*) cloud model in our grid, which has been shown to do a reasonably good job at reproducing brown dwarf spectra with similar properties (e.g., Kirkpatrick et al., 2006). We will therefore refer to the custom grid constructed here as *PHOENIX-ACES-DUSTY* to distinguish it from other models based on the *PHOENIX* framework.

We explore the results of this choice of cloud model and describe the results from a few other models in Section 2.3.3.

The synthetic spectra from the grid were calculated with a wavelength sampling of 0.05 Å from 1.4 to 2.4 μm. Each spectrum was convolved with a Gaussian kernel with a FWHM that matched the OSIRIS spectral resolution (Barman et al., 2015). Both flux calibrated and continuum subtracted data were modeled and analyzed. The synthetic spectra was flux calibrated and continuum subtracted using the same routines as the data.

2.3.2 Forward Modeling

To determine the best-fit *PHOENIX-ACES-DUSTY* model, we use a forward-modeling approach following Blake et al. (2010), Burgasser et al. (2016), Hsu et al. (in prep), and Theissen et al. (in prep). The effective temperature ($T_{\rm eff}$), surface gravity ($\log g$), and metallicity ([M/H]) are inferred using a Markov Chain Monte Carlo (MCMC) method built on the `emcee` package that uses an implementation of the affine-invariant ensemble sampler (Goodman & Weare, 2010; Foreman-Mackey et al., 2013).

We assume that each parameter we are solving for should be normally distributed, and thus the log-likelihood function is computed as follows

$$\ln L = -0.5 \times \left[\sum \left[\frac{\text{data}[p] - D[p]}{\sigma[p]} \right]^2 + \sum ln(2\pi\sigma^2) \right], \tag{2.1}$$

where σ is the provided uncertainties, data[p] is our science data, and $D[p]$ is the forward-modeled data. The uncertainty is taken as the difference between the 84th and 50th percentile as the upper limit, and the difference between the 50th and 16th percentile as the lower limit for all model parameters. If the posterior distributions follow normal (Gaussian) distributions then this equates to the 1-σ uncertainty in each parameter (e.g., Blake et al. 2010; Burgasser et al. 2016). Assuming that there are no additional systematic uncertainties in the data or in the models, these uncertainties should be an accurate reflection of our knowledge of each parameter.

We discuss and attempt to account for additional systematic uncertainties in the data and the models in Section 2.3.3.

The data is forward-modeled using the following equation:

$$D[p] = C \times \left[\left(M \left[p \left(\lambda \left[1 - \frac{RV}{c} \right] \right), T_{\rm eff}, \log g, [M/H] \right] \right) \right] * \kappa_G(\Delta\nu_{\rm inst}) + C_{\rm flux}. \quad (2.2)$$

Here, $p(\lambda)$ is the mapping of the wavelength values to pixels, $M[p(\lambda)]$ is the stellar atmosphere model parameterized by effective temperature ($T_{\rm eff}$), surface gravity ($\log g$), and metallicity ([M/H]), C is the dilution factor, (radius/distance)^2, that scales the model to the observed fluxes, (which is measure of radius since the distance is known, e.g., Theissen & West 2014; Kesseli et al. 2019), and $\kappa_G(\Delta\nu_{\rm inst})$ is the line spread function (LSF) calculated from the OSIRIS resolution of $R = 4000$ to be 34.5 km s^{-1}. The RV is the radial velocity that is used here only to account for wavelength calibration errors in the OSIRIS DRP, c is the speed of light, and $C_{\rm flux}$ is an additive continuum correction to account for potential systematic offsets in the continuum. This final parameter ($C_{\rm flux}$) is only used when fitting the continuum normalized data. Our MCMC runs used 100 walkers, 500 steps, and a burn-in of 400 steps to ensure parameters were well mixed.

2.3.3 Temperature, Gravity, and Metallicity

We ran our MCMC fitting procedure on both the flux calibrated spectrum and the continuum-subtracted spectrum. The best-fit parameters for our flux calibrated data are $T_{\rm eff} = 1588 \pm 5$ K, $\log g = 4.72^{+0.05}_{-0.06}$, and a metallicity of [M/H] = 0.5 ± 0.01. For the radius, which comes from the multiplicative flux parameter, we found R = 1.00 $\pm$ 0.02 R_{Jup}. For our continuum-subtracted data the best-fit parameters were $T_{\rm eff}$ = 2048 $\pm$ 11 K, $\log g$ = 3.77 $\pm$ 0.03, and a metallicity of [M/H] = -0.11 ± 0.02. Radii cannot be derived for the continuum-subtracted data. Figures 2.3 through 2.6 show the best-fit spectrum overplotted on our data, and the resulting corner plots from our MCMC analysis for both the initially extracted and continuum-subtracted spectra.

Table 2.2: Summary of atmospheric parameters derived from MCMC fits.

Spectra κ And b	Effective Temperature $T_{\rm eff}$ (K)	Surface Gravity $\log g$	Metallicity [M/H]	Radius ($R_{\rm Jup}$)	Luminosity $\log_{10}\left(\frac{L}{L_\odot}\right)$
PHOENIX-ACES-DUSTY					
OSIRIS Including Continuum	1588 ± 5	$4.72^{+0.05}_{-0.06}$	$0.50^{+0.01}_{-0.01}$	1.0 ± 0.02	-4.2 ± 0.1
OSIRIS Continuum Subtracted	2048 ± 11	3.77 ± 0.03	-0.11 ± 0.02	n/a	n/a
CHARIS All Bands	2021^{+20}_{-19}	$3.64^{+0.18}_{-0.10}$	$0.46^{+0.03}_{-0.07}$	0.99 ± 0.02	-3.80 ± 0.02
CHARIS K Band Only	1707^{+147}_{-118}	$4.62^{+0.48}_{-0.63}$	$-0.12^{+0.28}_{-0.23}$	1.4 ± 0.2	-3.8 ± 0.1
SpeX 2MASS J01415823−4633574	1972^{+9}_{-10}	$2.93^{+0.08}_{-0.14}$	0.49 ± 0.01	n/a	n/a
BT-SETTL					
OSIRIS Including Continuum	1630^{+7}_{-5}	$3.5^{+0.5}_{-0.4}$	n/a	1.10 ± 0.10	-4.11 ± 0.1
OSIRIS Continuum Subtracted	2128^{+70}_{-73}	$4.47^{+0.02}_{-0.06}$	n/a	n/a	n/a
CHARIS All Bands	1817^{+48}_{-18}	$5.15^{+0.13}_{-1.13}$	n/a	1.2 ± 0.1	-3.8 ± 0.1
CHARIS K Band Only	1647^{+194}_{-96}	$4.16^{+0.35}_{-0.33}$	n/a	1.5 ± 0.3	-3.8 ± 0.2
DRIFT-PHOENIX					
OSIRIS Including Continuum	2200^{+100}_{-130}	$4.0^{+0.3}_{-0.5}$	n/a	$1.0^{+0.2}_{-0.1}$	-3.6 ± 0.2
OSIRIS Continuum Subtracted	2126^{+104}_{-131}	$4.19^{+0.2}_{-0.22}$	n/a	n/a	n/a
CHARIS All Bands	1747^{+20}_{-18}	$3.99^{+0.19}_{-0.20}$	n/a	1.5 ± 0.1	-3.7 ± 0.1
CHARIS K Band Only	1863^{+289}_{-233}	$4.22^{+0.50}_{-0.46}$	n/a	1.3 ± 0.3	-3.7 ± 0.2
Adopted Values	2050	3.8	-0.1	1.2	-3.8
Range of Allowed Values	1950 - 2150	3.5 - 4.5	-0.2 - 0.0	1.0 - 1.5	-3.5 - -3.9

[−]The grid used in each case is noted above derived parameters. Using the range of best-fit values and our estimates of systematic uncertainties, range of adopted atmospheric parameters for κ And b are shown in the last row. We are using the convention for metallicity where $[\mathrm{M/H}] = \log_{10}\left(\frac{N_M}{N_H}\right)_{\rm star} - \log_{10}\left(\frac{N_M}{N_H}\right)$

The discrepancy between the two fits, one with the continuum and one without, is not entirely unexpected. The continuum is strongly impacted by residual systematic errors from the speckle noise, which injects features at low spatial frequencies. Effective temperature is particularly sensitive to continuum shape, and as a bolometric quantity is better estimated by including data from a broader range of wavelengths. Subtracting the continuum mitigates and removes some of these residual errors.

In order to verify that the temperature estimates we derived from the flattened spectra are robust, we ran our MCMC fitting code using the *PHOENIX-ACES-DUSTY* grid on the CHARIS spectrum from Currie et al. (2018), which spans a much larger range of wavelengths (Figure 2.7). We adjusted our MCMC code for the CHARIS data by changing the LSF to 7377 km s^{-1} for the instrument. We fit all near-infrared bands simultaneously, and also performed a fit using only the K-band. For the fit to all the bands simultaneously, we obtained $T_{\rm eff} = 2021^{+20}_{-19}$ K, $\log g = 3.64^{+0.18}_{-0.10}$, $[\mathrm{M/H}] = 0.46^{+0.03}_{-0.07}$, and R = 0.99 $\pm$ 0.02. When we fit only the K-band of the CHARIS spectrum

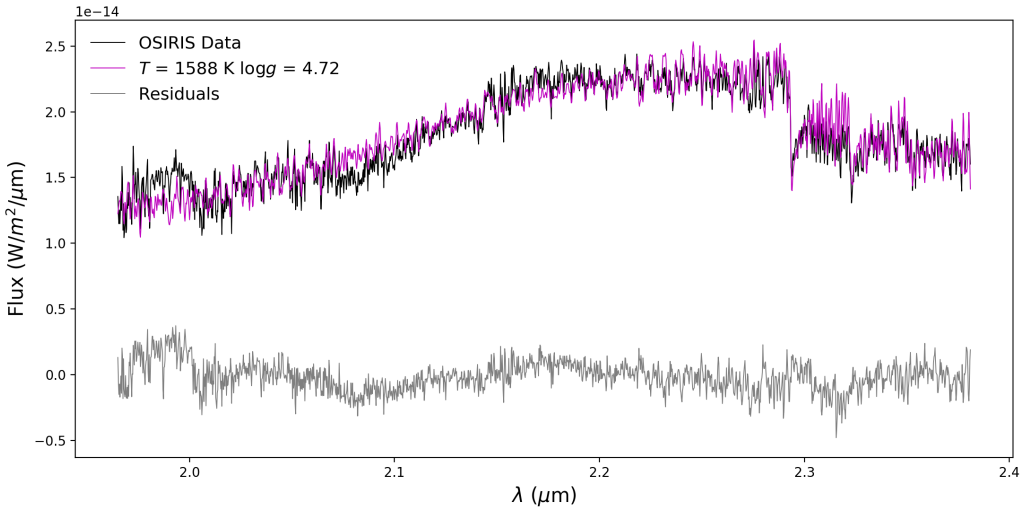

Figure 2.3: Results from the MCMC model fit to the OSIRIS spectrum for κ And b without continuum removal (black). The best matching *PHOENIX-ACES-DUSTY* model has $T_{\rm eff}$ = 1588 K, $\log g = 4.72$, and a [M/H] = 0.50 (magenta). The residuals between the data and the model are plotted in gray. The shape of the continuum is impacted by speckle noise, which modulates at low spatial frequencies and leaves residual noise in our dataset post speckle removal. The fits are then driven to lower temperatures and higher metallicities than previously found for κ And b due to the continuum shape impact, particular at blue wavelengths.

we obtained $T_{\rm eff} = 1707^{+147}_{-118}$ K, $\log g = 4.62^{+0.48}_{-0.63}$, [M/H] = $-0.12^{+0.28}_{-0.23}$, and R=1.4±0.2. The all-wavelength fit is consistent with the results we obtained for our continuum-normalized spectrum fitting of the OSIRIS data, while K-band only is slightly lower in temperature, albeit with large uncertainties. Our fits to the CHARIS data are also consistent with the results obtained in Currie et al. (2018) and Uyama et al. (2020) ($T_{\rm eff} \approx 1700-2000\ K, \log g \approx 4-4.5$, R=1.3–1.6 R_{Jup}). For a more detailed comparison of the OSIRIS continuum to the CHARIS spectrum, we binned our OSIRIS *K*-band spectra to the same sampling as the Currie et al. (2018) spectra shown in Figure 2.7. The spectra were consistent except for the OSIRIS spectral peak was shifted very slightly towards the red. Two CHARIS data points are less than 1.5-σ off from our OSIRIS data, and the rest (4 additional points) are consistent within the error bars.

Figure 2.7 also shows a comparison between our spectrum and the best-matching brown dwarf from the SpeX prism library (Burgasser et al., 2016) found by Currie et al. (2018), 2MASS

J01415823-4633574 (Kirkpatrick et al., 2006). This source is a young, early L-type object associated with the Tucana-Horologium association (age $\sim$ 40 Myr). Since the match to this brown dwarf is quite good, we also fit its spectrum using the same model grid and our MCMC framework, adjusting the model resolution to match SpeX. We found fully consistent properties with temperatures between $\sim$2050–2130 K and a $\log g \approx$ 3–4 for this source.

Figure 2.8 shows all available spectral and photometric data for κ And b. Overplotted on the spectrum is the best-fit *PHOENIX-ACES-DUSTY* model based on the continuum-subtracted OSIRIS spectrum. The model is scaled to match the continuum flux at K-band, which in turn is derived using the K-band magnitude in Currie et al. ($K_s = 14.37 \pm 0.07$; 2018). The match to the Currie et al. (2018) spectrum is quite good, in alignment with the consistent effective temperature we derive from fitting that data set with our models. While the shape of the J- and H-band spectra is similar to the CHARIS spectrum, the model over-predicts the flux by 2–7-σ in the H-band and 1–4-σ in the J-band, and slightly underpredicts the flux by $\sim$1.5-σ near 4 μm. The reason that a similar temperature is derived from an all-band fit to the CHARIS spectrum using our models is that the flux scaling parameter, and thus the radius, is lowered in this case such that it results in the model "trisecting" the three wavelengths, matching J- and H-band quite nicely, but then underpredicting the K-band flux.

The mismatch at J and H bands could almost certainly be due to the cloud properties used in our grid. We are using a DUSTY cloud model, which is meant to be a limiting case of a true thick cloud model. Generally, DUSTY models do a reasonable job at matching spectra in this temperature range (2000–2500 K). A slight modification to the cloud properties could result in a general change to the flux at a given band without dramatically impacting the spectral morphology. Given the insensitivity of the continuum-normalized OSIRIS spectrum to clouds, it is encouraging that all fits are returning consistent temperatures in spite of the flux offsets.

A recent analysis of the CHARIS data by Uyama et al. (2020) found a slightly lower temperature using models from Allard et al. (2012), Chabrier et al. (2000), and Witte et al. (2011) (*BT-SETTL*, *BT-DUSTY*, *DRIFT-PHOENIX*). These models have different assumptions about

cloud properties than we used in our grid. The *BT-SETTL* grids treat clouds with number density and size distribution as a function of depth based on nucleation, gravitational settling, and vertical mixing (Allard et al., 2012). The *DRIFT-PHOENIX* grids treat clouds by including effects of nucleation, surface growth, surface evaporation, gravitational settling, convection, and element conservation (Witte et al., 2011). Uyama et al. (2020) were able to get very good matches at all wavelengths using these models, with temperatures of 1700–1900 K and $\log g$ between 4–5. The range of uncertainties they found encompasses $\sim$2000 K, and were close to the range of temperatures we find with *PHOENIX-ACES-DUSTY*.

Since our subsequent analysis of the chemical abundances of κ And b relies on knowledge of the temperature and gravity, we did additional modeling to look at the comparison between these models and our continuum-normalized OSIRIS data. In addition to differences in cloud parameters, each set of models incorporates slightly different assumptions that lead to systematic differences in the output spectra for the same parameters such as temperature and gravity (e.g., Oreshenko et al. 2020). These systematics are not captured in the formal uncertainties from each MCMC run. We attempt to account for these systematics by looking at the range of values given from the three models.

We incorporated both the *BT-SETTL* and *DRIFT-PHOENIX* models into our MCMC analysis code, and fit our OSIRIS spectrum using the same procedure described above. The best-fit using *BT-SETTL* yielded $T_{\rm eff} = 2128^{+70}_{-73}$ K and $\log g = 4.47^{+0.02}_{-0.06}$. The *DRIFT-PHOENIX* models generally provided poor matches to the higher resolution data, but yielded $T_{\rm eff} = 2126^{+104}_{-131}$ K and $\log g = 4.19^{+0.2}_{-0.22}$ as best-fit parameters. We found no fits with *DRIFT-PHOENIX* that properly captured the first drop of the CO bandhead at $\sim$2.9 μm. We also fit the CHARIS data using our code and these model grids, and found parameters consistent with Uyama et al. (2020). We then looked in detail at the difference between our best-fits to the OSIRIS data and these lower temperature models at $R \sim 4000$. The χ^2 of the best fits ($T_{\rm eff} = 2100$ K) is significantly better than the χ^2 of a $T_{\rm eff} = 1700$ K, $\log g = 4$ model, by roughly 5σ using either grid.

Table 3.3.2 shows the results for all atmospheric parameters derived in this work. We use

the range of best-fit values from the OSIRIS continuum-normalized data to define the adopted parameters for temperature, gravity, and metallicity, as the resolved line information offers the most constraints on those parameters. We adopt values a value of $T_{\rm eff}$ = 2050 K, with a range of 1950–2150 K, $\log g$ = 3.8, with a range of 3.5–4.5, and [M/H] = −0.1, with a range of -0.2–0.0. For radius, we use the median value from the OSIRIS continuum-included data and the CHARIS data to arrive at $R = 1.2\ R_{Jup}$, with a range of 1.0–1.5 R_{Jup}. This yields an implied bolometric luminosity of $\log(L/L_\odot) = -3.7$, with a range of −3.5 to −3.9, consistent with the estimate from Currie et al. (2018). While it is possible that lower temperatures could be invoked for κ And b, a more detailed analysis including a variation of cloud models will be required to determine whether this is a viable solution that also matches the OSIRIS data. Since our high resolution data is not particularly informative for cloud properties, we leave such analysis to future work.

2.3.4 Mole Fractions of CO and H_2O

With best-fit values for temperature, surface gravity, and metallicity we can fit for abundances of CO and H_2O in our OSIRIS *K*-band spectra. Once best-fit values were determined for $T_{\rm eff}$, $\log g$, and [M/H], we fixed those parameters to generate a grid of spectra with scaled mole fractions of the molecules for the *K*-band (Barman et al., 2015). Since our best-fit metallicity was slightly subsolar (roughly 80% of the solar value), we note that the overall abundances of these molecules will be slightly less than that of the Sun, but their unscaled *ratios* will match the Sun. The molecular abundances of CO, CH_4, and H_2O were scaled relative to their initial values from 0 to 1000 using a uniform logarithmic sampling, resulting in 25 synthetic spectra. We fit for the mole fraction of H_2O first, holding CO and CH_4 at their initial values. The fit was restricted to wavelengths less than the CO band head to avoid biasing from overlapping CO. Next, the H_2O mole fraction was set to its nominal value, and we fit for scaled CO. While in principle we could do the same analysis for CH_4, we did not do so because in this temperature regime there is no expectation of a significant amount of CH_4 present in our *K*-band spectrum.

Figure 2.9 shows the resulting χ^2 distribution as a function of CO and H_2O mole fraction.

The models with the lowest χ^2 when compared to the flattened data gave us the best-fits for both H_2O and CO. The best fit for H_2O had a scaling of 1, and the best fit for CO had a scaling of 1.66. To calculate the 1-σ uncertainties in each mole fraction value, we used the values from models within ± 1 of our lowest χ^2. Using interpolation along the curves shown in Figure 2.9, the range of mole fractions encompassed by these uncertainties is 0.599 to 3.24 times the initial mole fraction of CO, and 0.599 to 1.791 times the initial H_2O mole fraction.

Todorov et al. (2016) derived a water abundance for κ And b using spectral retrieval with a one-dimensional plane-parallel atmosphere and a single cloud layer that covers the whole planet. This modeling was done on the low-resolution spectrum from P1640 presented in Hinkley et al. (2013). They derived the $\log(n_{H_2O})$ for four cases that varied in the treatment of molecular species and clouds. In each case, they found consistent values for the mole fraction of water, with $\log(n_{H_2O}) \sim -3.5$. Our best-matching mole fraction for water is $\log(n_{H_2O}) \sim -3.7$, which is consistent within the uncertainties in Todorov et al. (2016).

2.3.5 C/O Ratios

For giant planets formed by gravitational instabilities, their atmospheres should have element abundances that match their host stars (Helled & Schubert, 2009). If giant planets form by a multi-step core accretion process, it has been suggested that there could be a range of elemental abundances possible (Öberg et al., 2011; Madhusudhan, 2019). In this scenario, the abundances of giant planets' atmospheres formed by core/pebble accretion are highly dependent on the location of formation relative to CO, CO_2, and H_2O frost lines and the amount of solids acquired by the planet during runaway accretion phase. This can be diagnosed using the C/O ratio.

The C/O ratio dependence on atmospheric mole fractions (N) is

$$\frac{C}{O} = \frac{N(CH_4)+N(CO)}{N(H_2O)+N(CO)},$$

and for small amounts of CH_4, as in κ And b's case, the C/O ratio can be determined by H_2O and CO alone (Barman et al., 2015). The C/O ratio we derive for κ And b is $0.70^{+0.09}_{-0.24}$. In Figure 2.10 we show a visual comparison of three different models with different values of C/O, with our best-fit model in the middle panel. Clearly, the models with low C/O do not make deep enough lines in the CO bandhead, and the models with C/O near unity make the first drop in the CO bandhead too wide. With lower resolution, it would be difficult to distinguish this difference, thus demonstrating the need for higher spectral resolution to probe these abundance ratios.

Due to the remaining uncertainty in the temperature of the planet, we verified that lower temperature model grids with scaled mole fractions return C/O ratios encompassed by our model. We explored a grid with a temperature of $\sim$1900 K and a $\log g$ $\sim$4, scaling the ratios of H_2O and CO by the same values as above. We find that the best matching spectrum at this temperature is also $\sim$0.70, with similar uncertainties. Given the obvious changes in the spectral morphology expected at high and low C/O ratio as shown in Figure 2.10, it is not surprising that a small temperature change does not dramatically change the best-fit C/O ratio. Thus we assert that our uncertainties properly capture our current knowledge of the C/O ratio for κ And b.

2.4 Kinematic Modeling

2.4.1 Radial Velocity Measurement

Radial velocity measurements can be used to help determine the orientation of the planets' orbital plane. We measure the radial velocity of κ And b following a similar method to the one described in Ruffio et al. (2019). A significant limitation of Ruffio et al. (2019) is that the transmission of the atmosphere in Ruffio et al. (2019) is calculated using A0 star calibrators, which assumes that the tellurics are not changing during the course of a night. This assumption is not valid for the κ And b data presented in this work, as discussed in Section 2.2. We therefore improved upon the method to correct for the biases due to the variability of the telluric lines compared to the calibrator.

A common way to address such systematics in high-resolution spectroscopic data is to use a principal component analysis (PCA)-based approach to subtract the correlated residuals in the data (Hoeijmakers et al., 2018; Petit dit de la Roche et al., 2018; Wang et al., 2018a). However, this approach can lead to over-subtraction of the planet signal and therefore also bias any final estimation. For example, the water lines from the companion can be subtracted by the telluric water lines appearing in the PCA modes. The over-subtraction can be mitigated by jointly fitting for the planet signal and the PCA modes, which is possible in the framework presented in Ruffio et al. (2019). The original data model is,

$$d = M_1 \phi_1 + n. \tag{2.3}$$

The data d is a vector including the pixel values of a spectral cube stamp centered at the location of interest. The data vector has $N_d = 5 \times 5 \times N_\lambda$ elements corresponding to a 5×5 spaxel stamp in the spatial dimensions and N_λ spectral channels (e.g., $N_\lambda = 1665$ in K-band). The matrix M_1 includes a model of the companion and the spurious starlight. It is defined as $M_1 = [c_{0,\text{planet}}, c_1, \ldots, c_{25}]$, where the c_i are column vectors with the same size as the data vector d. The companion model $c_{0,\text{planet}}$ is also a function of the RV of the companion. The linear parameters of the model are included in ϕ_1 and the noise is represented by the random vector n.

A spectrum of the planet can be extracted at any location in the image by, first, subtracting a fit of the null hypothesis (i.e., $M_0 = [c_1, \ldots, c_{25}]$) from the data, $r_{xy} = d - M_0 \phi_0$, and then, fitting the companion PSF at each spectral channel to the residual stamp spectral cube. We perform this operation at each location in the field of view and divide the subsequent residual spectra by their local low-pass filtered data spectrum.

This results in a residual vector r_{xy}, which has been normalized to the continuum, for each spaxel in the field of view. After masking the spaxels surrounding the true position of the companion, a PCA of all the r_{xy} for a given exposure defines a basis of the residual systematics in the data. These principal components can be used to correct the model of the data. Before

they can be included in the data model, each principal component needs to be rescaled to the local continuum, which is done by multiplying them by the low-pass filtered data at the location of interest. Finally, these 1D spectra are applied to the 3D PSF to provide column vectors that can be used in the model matrix M. We denote these column vectors $\{r_{\rm pc1}, r_{\rm pc2}, \dots\}$ ordered by decreasing eigenvalues.

A new data model M_2 including the first K principal components is defined as

$$M_2 = [c_{0,\rm planet}, c_1, \dots, c_{25}, r_{\rm pc1}, \dots, r_{{\rm pc}K}]. \tag{2.4}$$

We define a new vector of linear parameter ϕ_2 including K more elements than ϕ_1. The advantage of this approach is that the PCA modes are jointly fit with the star and the companion models preventing over-subtraction. Additionally, the general form of the linear model is unchanged, which implies that the radial velocity estimation is otherwise identical to Ruffio et al. (2019).

Figure 2.11 shows the RV estimates for each exposure as a function of the number of principal components used in the model. The final RV converges from $-11.9 \pm 0.4\,\mathrm{km\,s^{-1}}$ to $-13.9 \pm 0.4\,\mathrm{km\,s^{-1}}$ as the number of modes increases suggesting a $2\,\mathrm{km\,s^{-1}}$ bias in the original model. In order to increase our confidence in the robustness of the RV estimate and uncertainty, we calculate the final RV and uncertainty after binning the data by pair to account for possible correlations between exposures. Each pair of measurements is replaced by their mean value and largest uncertainty. We note that the reduced χ^2 is lower than unity, which suggests that the final uncertainty is not overestimated.

Additionally, we perform a simulated companion injection and recovery at each location in the field of view to estimate possible residual biases in the data. The corrected RV estimates are shown in Figure 2.12, which prove to be consistent with the results from Figure 2.11. Table 3 summarizes the RV estimates, uncertainties, and χ^2_r as a function of the different cases presented previously. The uncertainties are inflated when χ^2_r is greater than unity.

We conclude that the RV of κ And b is $-14.1 \pm 0.4\,\mathrm{km\,s^{-1}}$ (cf Table 4), while the estimates

Table 2.3: κ And b RV estimates summary.

# PCs	Independent		Binned		Independent + injection & recovery			Binned + injection & recovery		
	RV ($\mathrm{km\,s^{-1}}$)	χ^2_r	RV ($\mathrm{km\,s^{-1}}$)	χ^2_r	RV ($\mathrm{km\,s^{-1}}$)	χ^2_r	Offset ($\mathrm{km\,s^{-1}}$)	RV ($\mathrm{km\,s^{-1}}$)	χ^2_r	Offset ($\mathrm{km\,s^{-1}}$)
None	-11.9 ± 0.4[a]	1.8	-11.9 ± 0.3[a]	1.1	-13.2 ± 0.3[a]	1.6	−1.28	-13.1 ± 0.3	0.8	−1.28
1	-13.2 ± 0.3[a]	1.5	-13.1 ± 0.3	0.8	-13.3 ± 0.4[a]	1.6	−0.14	-13.3 ± 0.3	0.9	−0.15
5	-13.8 ± 0.3[a]	1.4	-13.8 ± 0.3	0.8	-14.0 ± 0.3[a]	1.6	−0.16	-14.0 ± 0.3	0.9	−0.17
10	-13.9 ± 0.3[a]	1.4	-13.9 ± 0.3	0.8	-14.1 ± 0.4[a]	1.6	−0.19	-14.1 ± 0.3	1	−0.19

[−](Columns 2–3) RVs calculated using a data model that includes principal component as defined in Equation 2.4. The final RVs were calculated with a weighted mean assuming that each individual exposure is independent. (Columns 4–5) Same as columns 2–3, but pairs of consecutive exposures were averaged and the largest of their uncertainties used. (Columns 6–7) RVs are corrected for biases using simulated planet injection and recovery. The resulting offset on the final RV with and without the injection and recovery is given in column 8. (Columns 9–11) Same as columns 6–8, but combining consecutive pairs of exposures.

[a]Uncertainties have been inflated by χ^2_r when χ^2_r is greater than unity.

for the RV of the star are $-12.7\pm0.8\,\mathrm{km\,s^{-1}}$ (Gontcharov, 2006) and $-11.87\pm1.53\,\mathrm{km\,s^{-1}}$ (Becker et al., 2015). These values are consistent within the uncertainties - we use $-12.7\pm0.8\,\mathrm{km\,s^{-1}}$ in the following because the uncertainty is smaller. The relative RV between the companion and the star is $-1.4\pm0.9\,\mathrm{km\,s^{-1}}$ for which the error is dominated by the stellar RV. Similar to Ruffio et al. (2019), this highlights the need to better constrain the stellar RV of stars hosting directly imaged companions.

Table 2.4: Final RVs for κ Andromedae b.

Date	RV ($\mathrm{km\,s^{-1}}$)
2016 Nov 6–8	-14.3 ± 0.4
2017 Nov 4	-13.6 ± 0.6

2.4.2 Orbital Analysis

The orbit of κ And b has been explored using astrometry by several authors (Blunt et al. 2017; Currie et al. 2018; Uyama et al. 2020; Bowler et al. 2019). Though the orbit is highly under-constrained in terms of phase coverage, current fits to astrometry have yielded some constraints on orbit orientation and eccentricity of the companion. In particular, the eccentricity is currently estimated to be fairly high ($>$0.7).

The measurement of an RV for the companion with our OSIRIS data offers a valuable new piece of information, wherein degeneracies in the orbit orientation can be resolved. To determine the constraints provided by the RV measurement, we performed a series of orbit fits with both astrometry from the literature (Carson et al. 2013; Bonnefoy et al. 2014; Currie et al. 2018; Uyama et al. 2020) and our OSIRIS RV using the code described in O'Neil et al. (2019). Specifically, we use the Efit5 code (Meyer et al., 2012), which uses MULTINEST to perform a Bayesian analysis of our data (e.g., Feroz et al. 2009), and we use two different priors. We first use the typical flat priors in orbital parameters, including period (P), eccentricity (e), time of periastron passage (T_0), inclination (flat in $\sin i$), longitude of the ascending node (Ω or O), and longitude of periastron passage (ω or w). We also use the observational-based priors derived in O'Neil et al. (2019). Although we believe the latter are more appropriate in this case due to the biases introduced by flat priors for under-constrained orbits, we include both for completeness. We performed fits both with and without the RV point derived above to determine the impact of including the RV. We fix the distance to 50.0 ± 0.1 pc (Gaia Collaboration et al., 2018), and the mass to the value of 2.7 ± 0.1 $M_\odot$ estimated by Jones et al. (2016), which encompasses the range of values they found given uncertainty in the internal metallicity of κ And A.

The results of these fits are given in Table 2.5 and shown visually in corner plots in Figures 2.13–2.16. The addition of the RV constrains Ω to most likely be $\sim$85–90deg, although due to the large uncertainty in the RV the secondary peak is not completely ruled out. Additionally, the RV pushes the distribution of eccentricities slightly higher than the astrometry alone, with global minima $>$0.8, although the uncertainties encompass the previous values. Figures 2.17 and 2.18 demonstrates the impact of the RV on the best-fit orbits. Although the best fits are not strictly meaningful due to undersampling of the period, there are clear differences in orbit predictions when the RV is included - the best fit with astrometry alone favors RVs that are closer to 0 km s^{-1}.

The current prediction (whether RVs are included or not) is that κ And b is on its way towards closest approach in the next 20–30 years. It is possible this prediction is impacted

by systematics in the astrometric dataset, which is drawn from multiple different cameras and reduction pipelines. Indeed, the observational prior is meant to account for this known bias in $T_{0)}$, and using it pushes the prediction of periastron later by about 10 years (Table 2.5). If it is the case that the planet is heading towards closest approach, the predicted change in RV in the next several years is significant and thus can be easily confirmed with more data of similar quality in the next decade. Thus spectroscopy has the potential to provide much more stringent constraints on the orbit in the near term than more astrometric measurements.

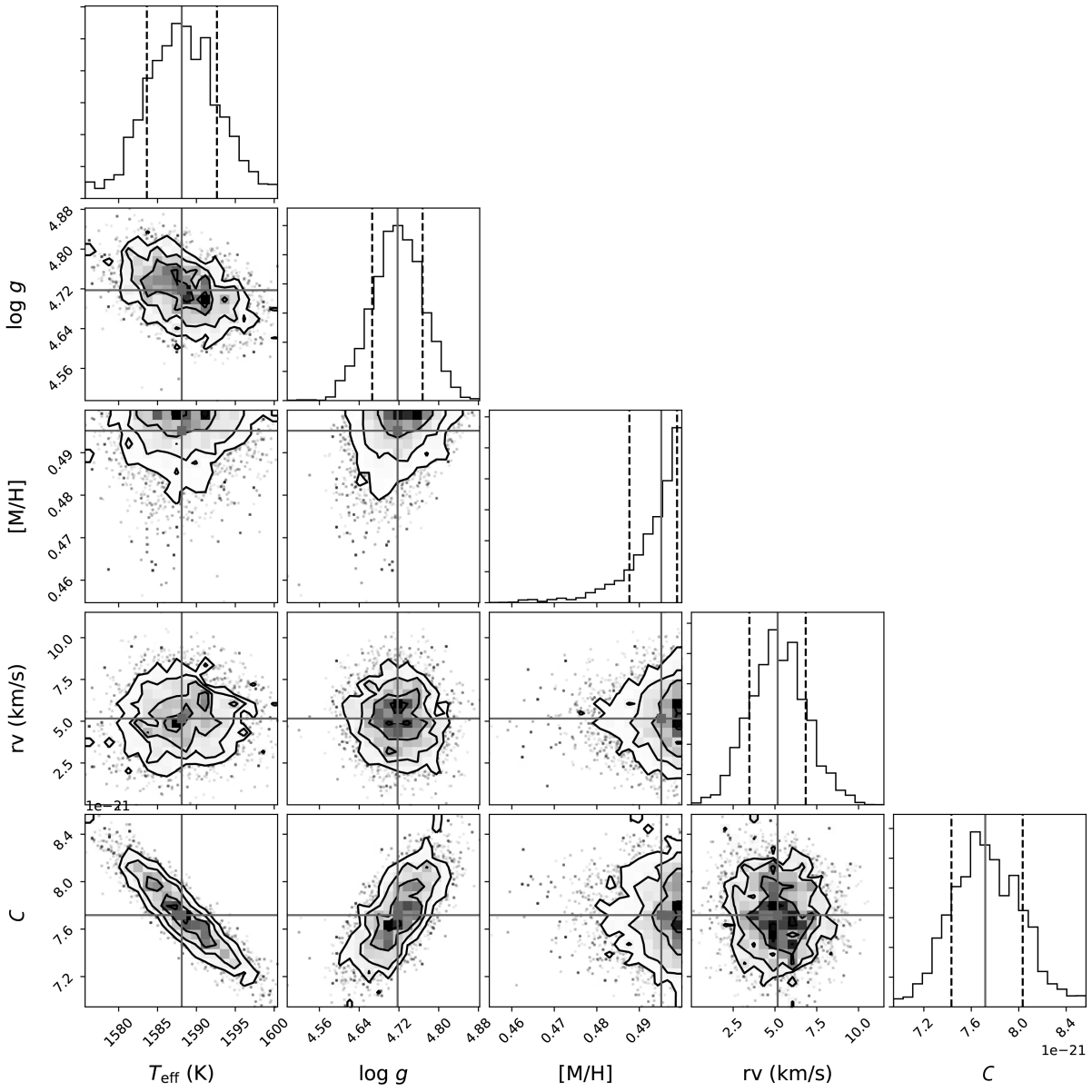

Figure 2.4: Corner plot corresponding to the fit shown in Figure 2.3. {The diagonal shows the marginalized posteriors. The subsequent covariances between all the parameters are in the corresponding 2-d histograms. The blue lines represent the 50 percentile, and the dotted lines represent the 16 and 84 percentiles. *C* corresponds to the dilution factor that scales the model by $(radius)^2(distance)^{-2}$ as mentioned in Section 3.3.2

.

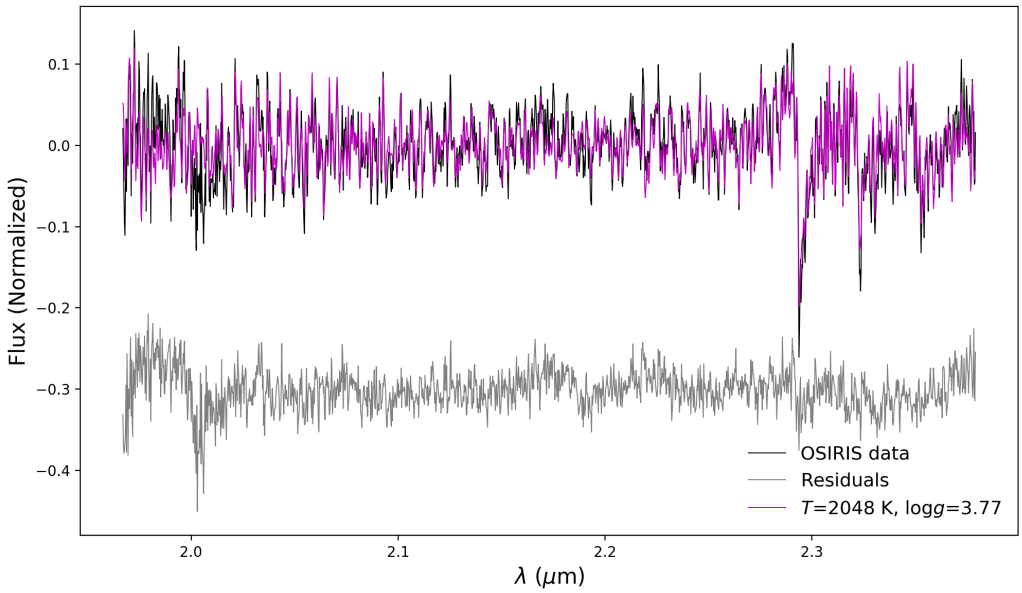

Figure 2.5: Results from MCMC model fit to the OSIRIS spectrum after continuum removal (black). The best fitting model has $T_{\rm eff}$ = 2048 K, $\log g$ = 3.77, and [M/H] = −0.11 in magenta. The residuals between the flattened data and the flattened model are in gray.

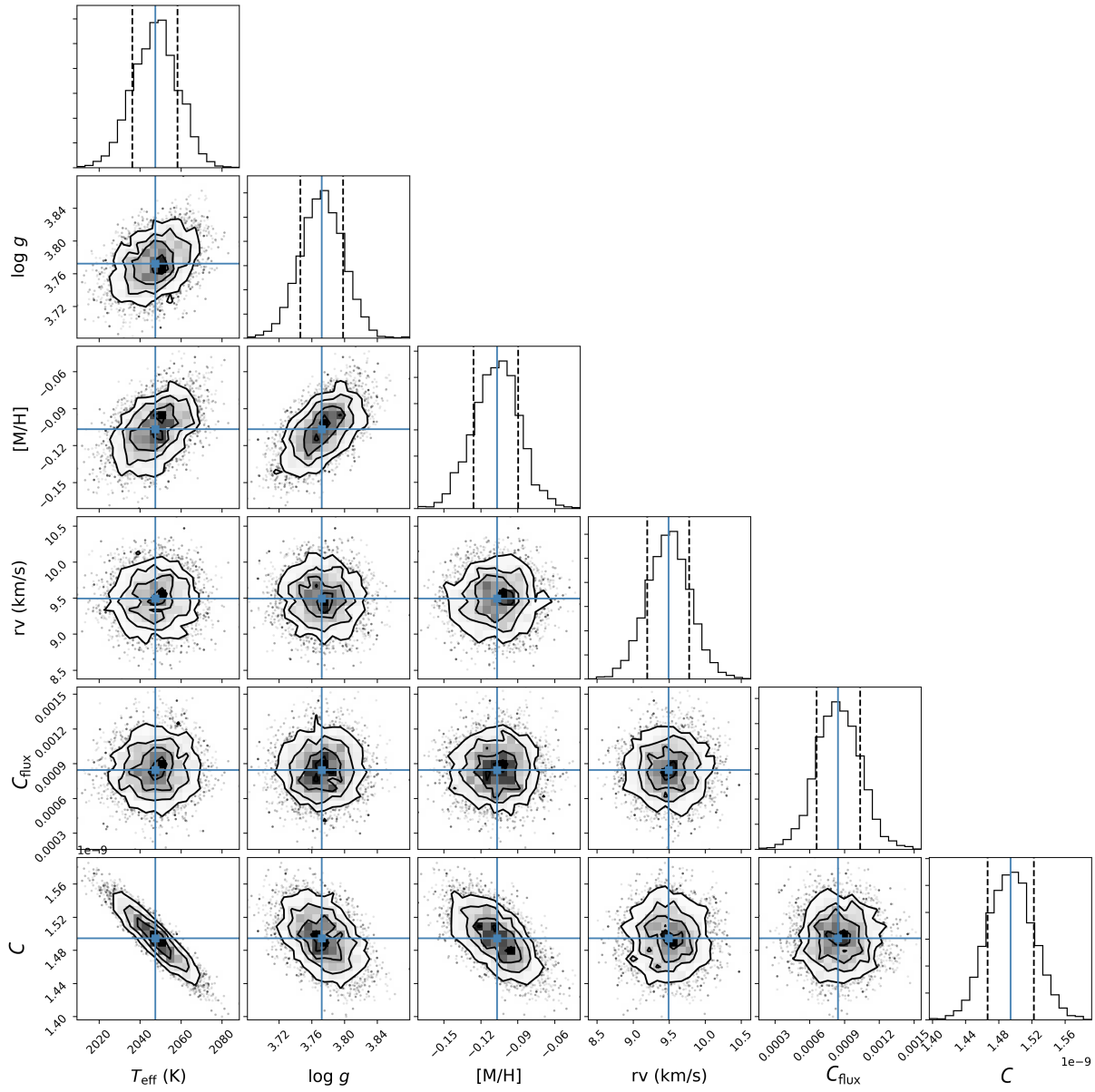

Figure 2.6: Corner plot corresponding to the fit shown in Figure 2.5. The diagonal shows the marginalized posteriors. The subsequent covariances between all the parameters are in the corresponding 2-d histograms. The blue lines represent the 50 percentile, and the dotted lines represent the 16 and 84 percentiles. C_{flux} is the additive flux parameter and C corresponds to the dilution factor that scales the model by $(radius)^2(distance)^{-2}$ as mentioned in Section 3.3.2

.

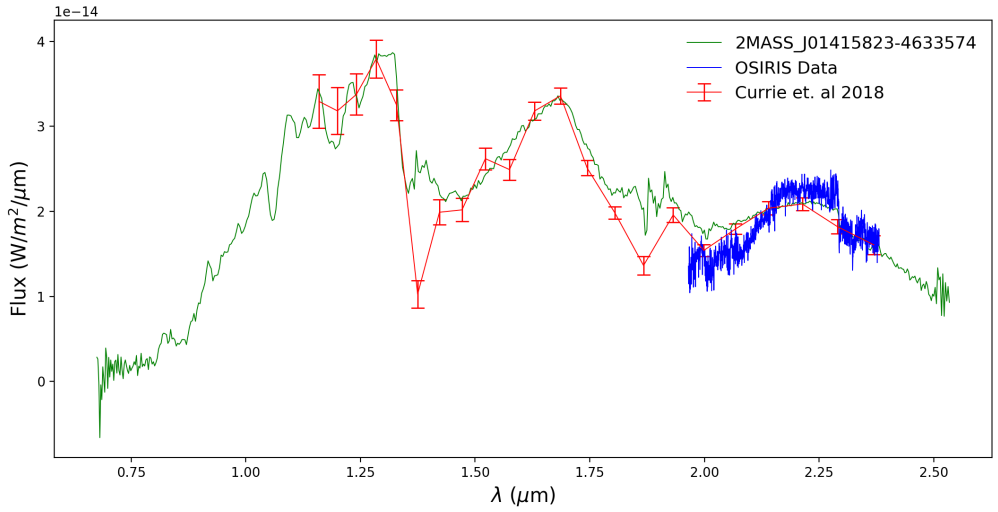

Figure 2.7: OSIRIS *K*-band data of κ And b compared to Currie et al. (2018) low-resolution CHARIS data of κ And b and their best-matching field source, 2MASS J01415823-4633574 from the SpeX Library (Kirkpatrick et al., 2006). A fit to the SpeX spectrum (not shown) reveals temperatures and gravities consistent with the OSIRIS and CHARIS data on κ And b.

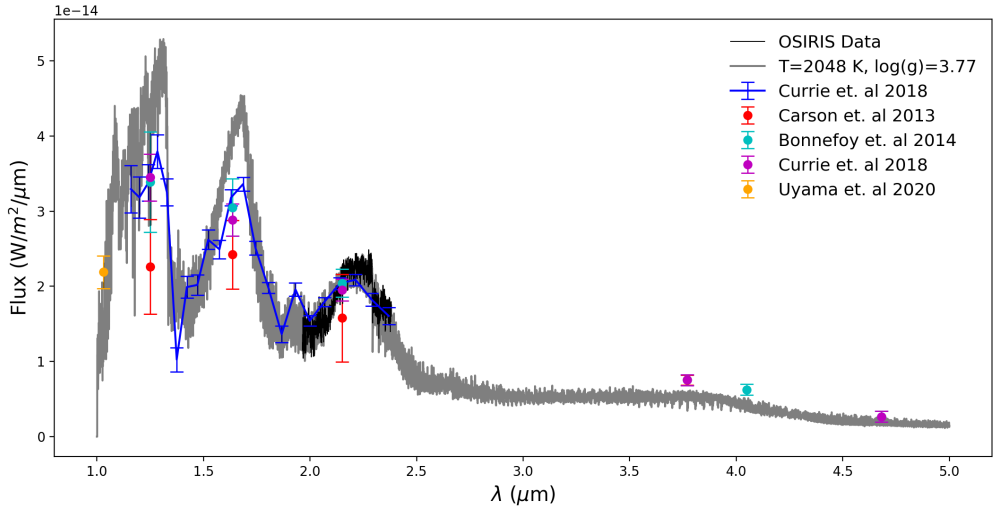

Figure 2.8: All available spectral and photometric data for κ And b compared to the best-fit *PHOENIX-ACES-DUSTY* model, shown in gray, of $T_{\rm eff}$ = 2048 K, $\log g$ = 3.77, and M/H = −0.11 over the near-infrared. Our OSIRIS data are shown in black. Currie et al. (2018) low-resolution CHARIS spectra is plotted in dark blue. Photometric data points are taken from Bonnefoy et al. (2014), Carson et al. (2013), Currie et al. (2018), and Uyama et al. (2020). The model matches the data at *K*-band, but predicts higher flux in *H*- and *J*-band (though the morphology is consistent). The mismatch at the low and high wavelength range is likely due to our use of a DUSTY cloud model.

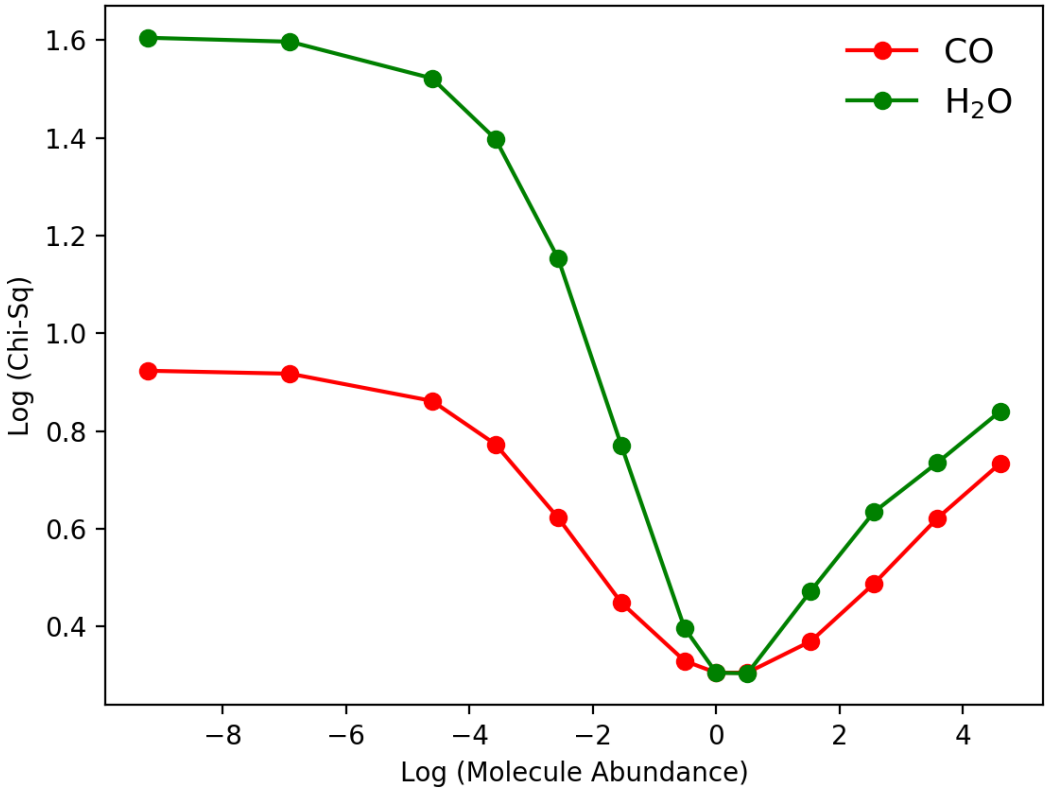

Figure 2.9: Results of $T_{\rm eff}$ = 2048 K and $\log g$ = 3.77 model fits with varying mole fractions for both H_2O and CO to our continuum-subtracted OSIRIS spectrum. The mole fractions are given in units relative to the ratio in the Sun, such that a value of zero implies the solar value. Both scalings of CO and H_2O prefer values near solar. From these fits we find C/O = $0.70^{+0.09}_{-0.24}$.

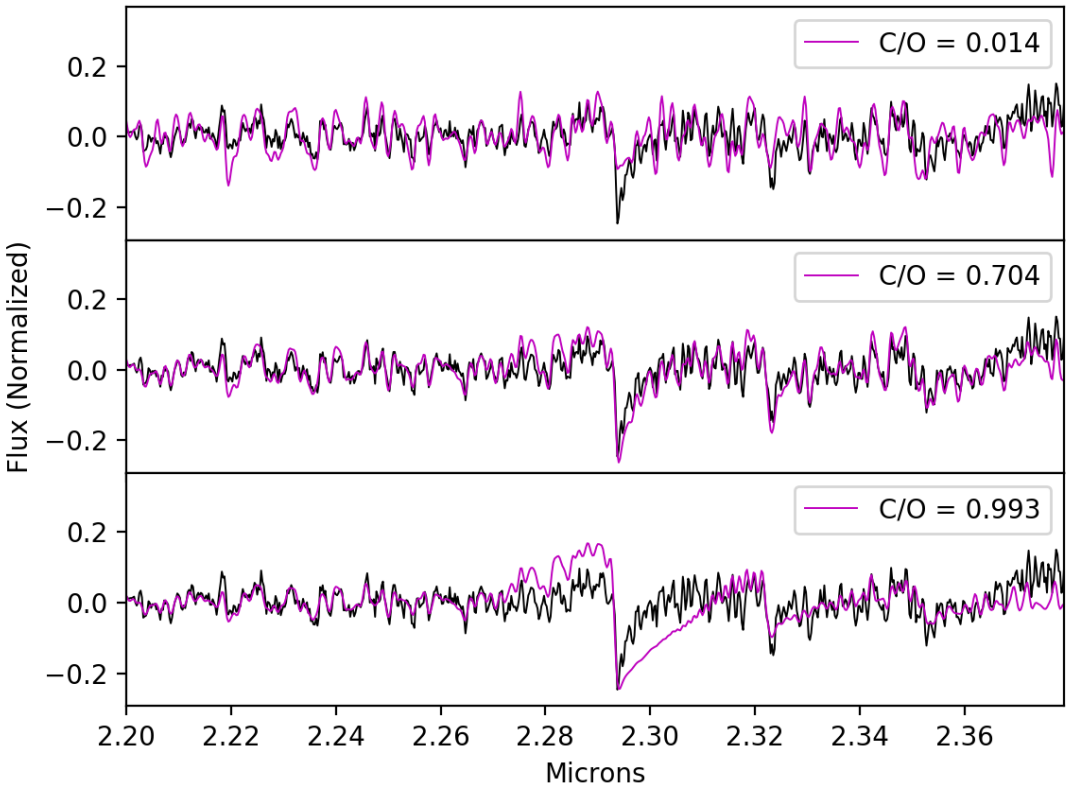

Figure 2.10: Visual comparison of three different $T_{\rm eff}$ = 2048 K and $\log g$ = 3.77 models with different values of C/O in our scaled mole fraction grid. The best fit C/O ratio is shown in the central panel, while values of very high (bottom) and very low (top) C/O ratio are clearly disfavored by our data. The relative strengthening or weakening of the primary CO bandhead at $\sim$2.29 μm is a fairly clear discriminator at R$\sim$4000 that might otherwise be lost at lower spectral resolution.

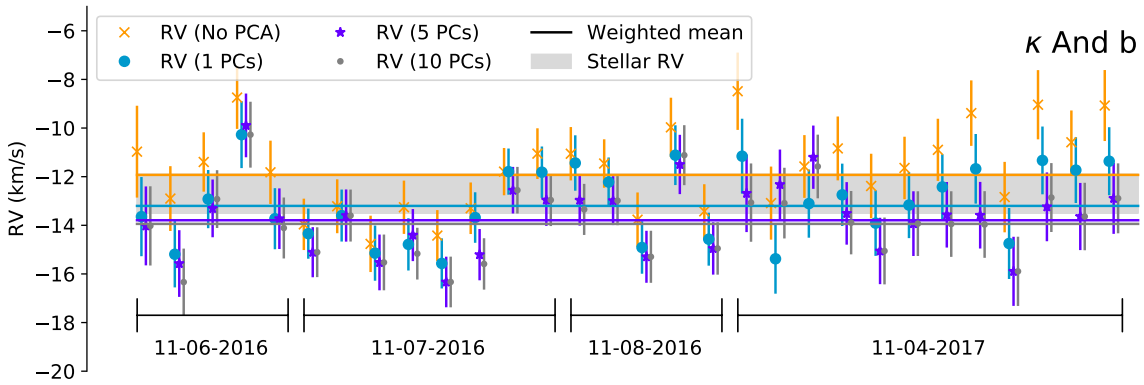

Figure 2.11: Radial velocity (RV) measurements of κ And b by individual exposures and epoch of observation. The grey region represents the current uncertainty in the RV of the star. The RVs are shown for different number of principal components (None, 1, 5, and 10 respectively) included in the data model. The weighted mean RVs (solid horizontal lines) converge as the number of principal components increases. The final RV values and uncertainties are available in Table 2.4.1.

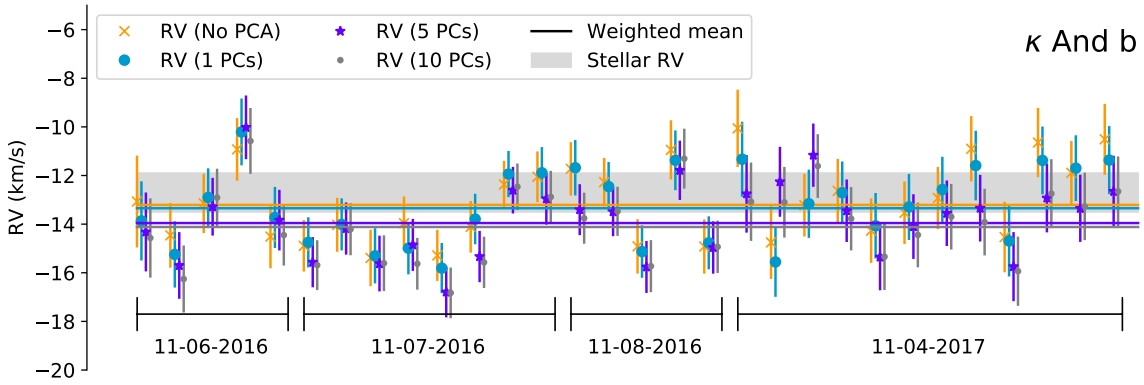

Figure 2.12: Same as Figure 2.11, but corrected for biases using simulated planet injection and recovery. The final RV values and uncertainties are available in Figure 2.3.

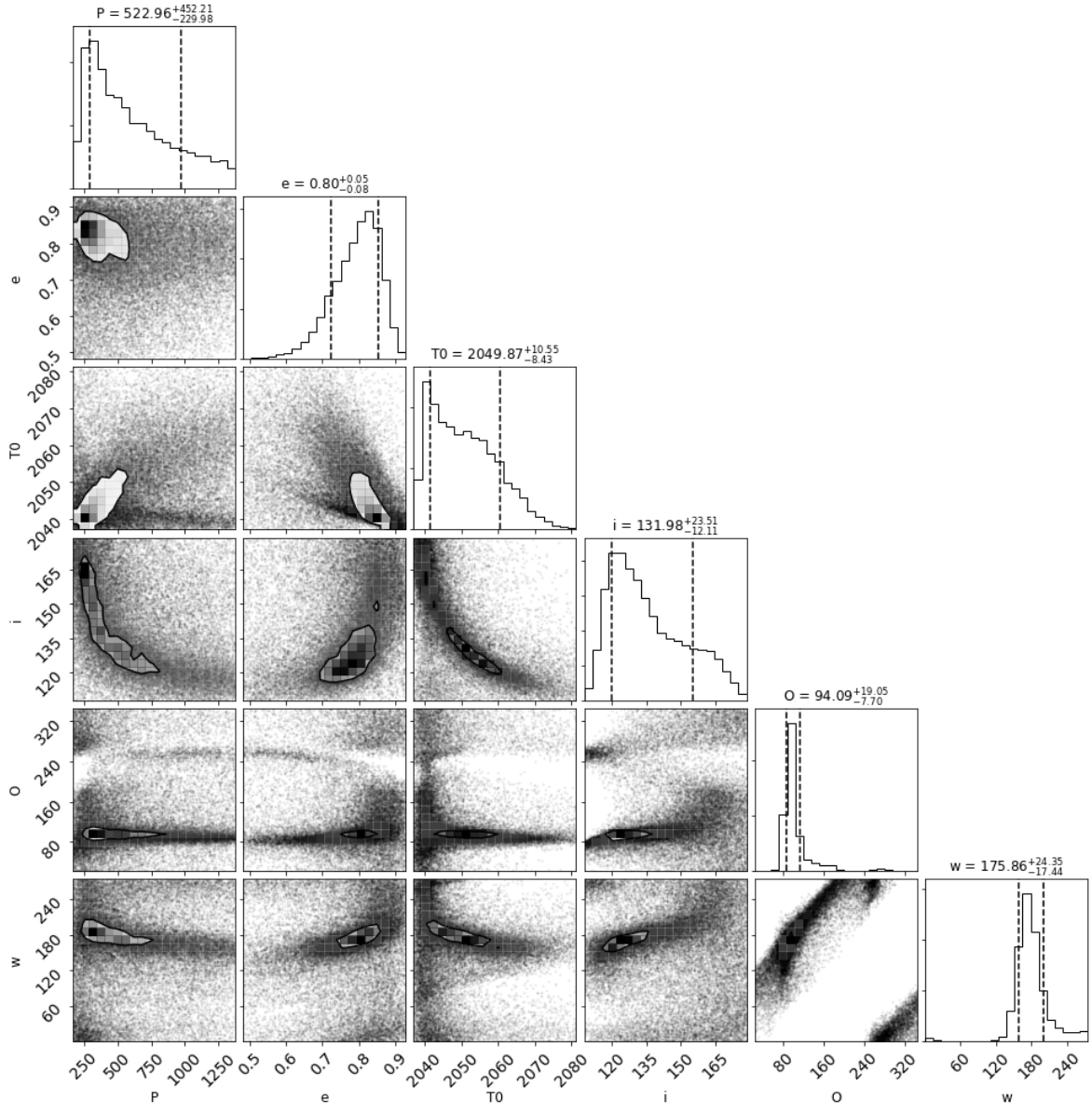

Figure 2.13: Corner plot showing the results of fitting the orbit of κ And b, including both astrometry and radial velocities. In this case, we use the observationally based prior presented in O'Neil et al. (2019), which can help account for biases in parameters like T_0 that arise in undersampled orbits. Note that this prior does increase the range of T_o included in our 1σ uncertainties more than is seen when flat priors in the orbital parameters are used (e.g., Figure 2.15). The allowed parameter space for ω also shrinks considerably when RV is included (see for comparison Figure 2.14).

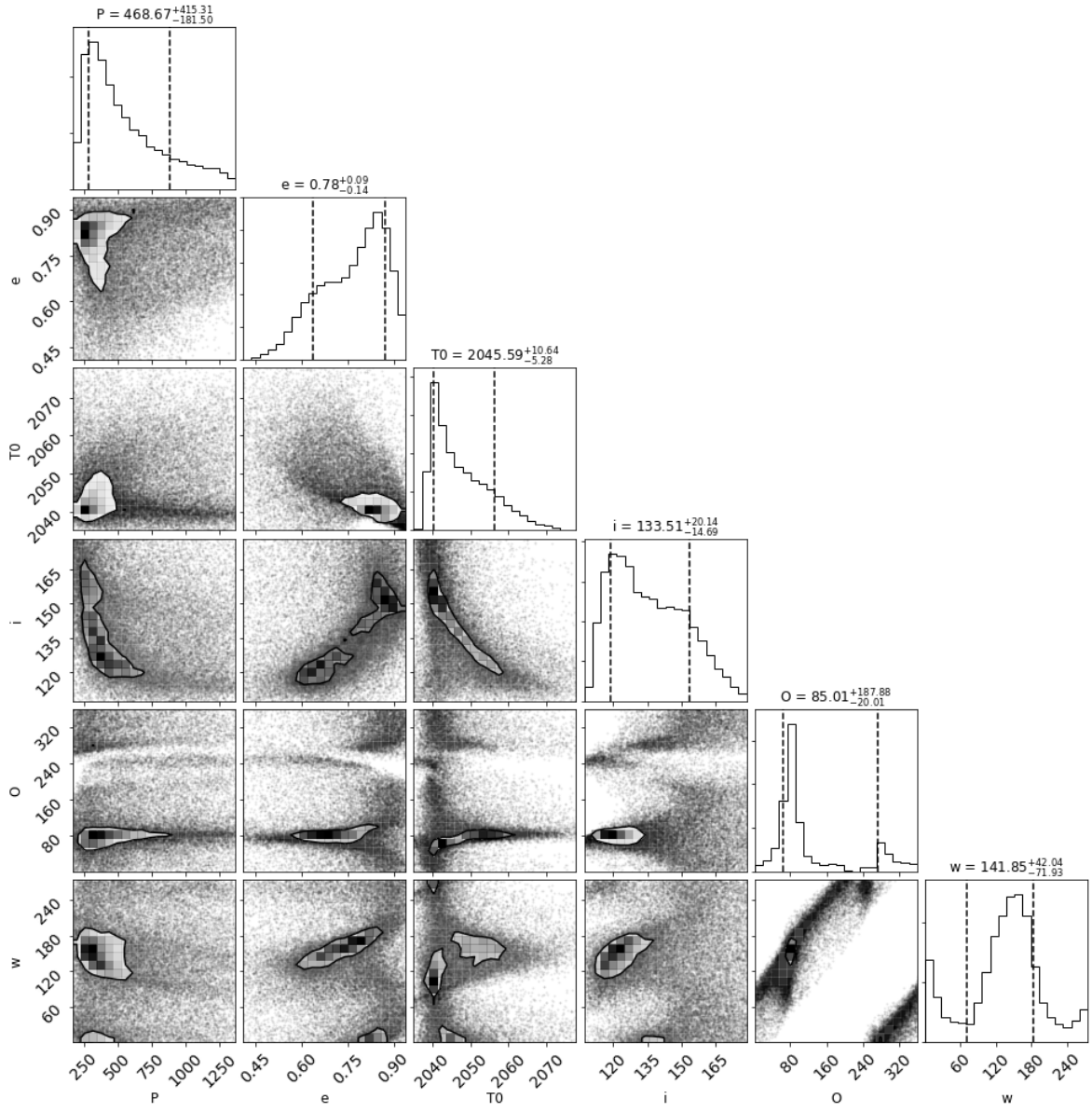

Figure 2.14: The same as Figure 2.13, but with no RV included in the fit. The results give values for orbital parameters consistent with previous fits found in the literature. A secondary peak in Ω can be seen more prominently here around $\sim 270^o$ that is nearly absent in Figure 2.13. The addition of the RV eliminates this degeneracy in the orbit plane orientation.

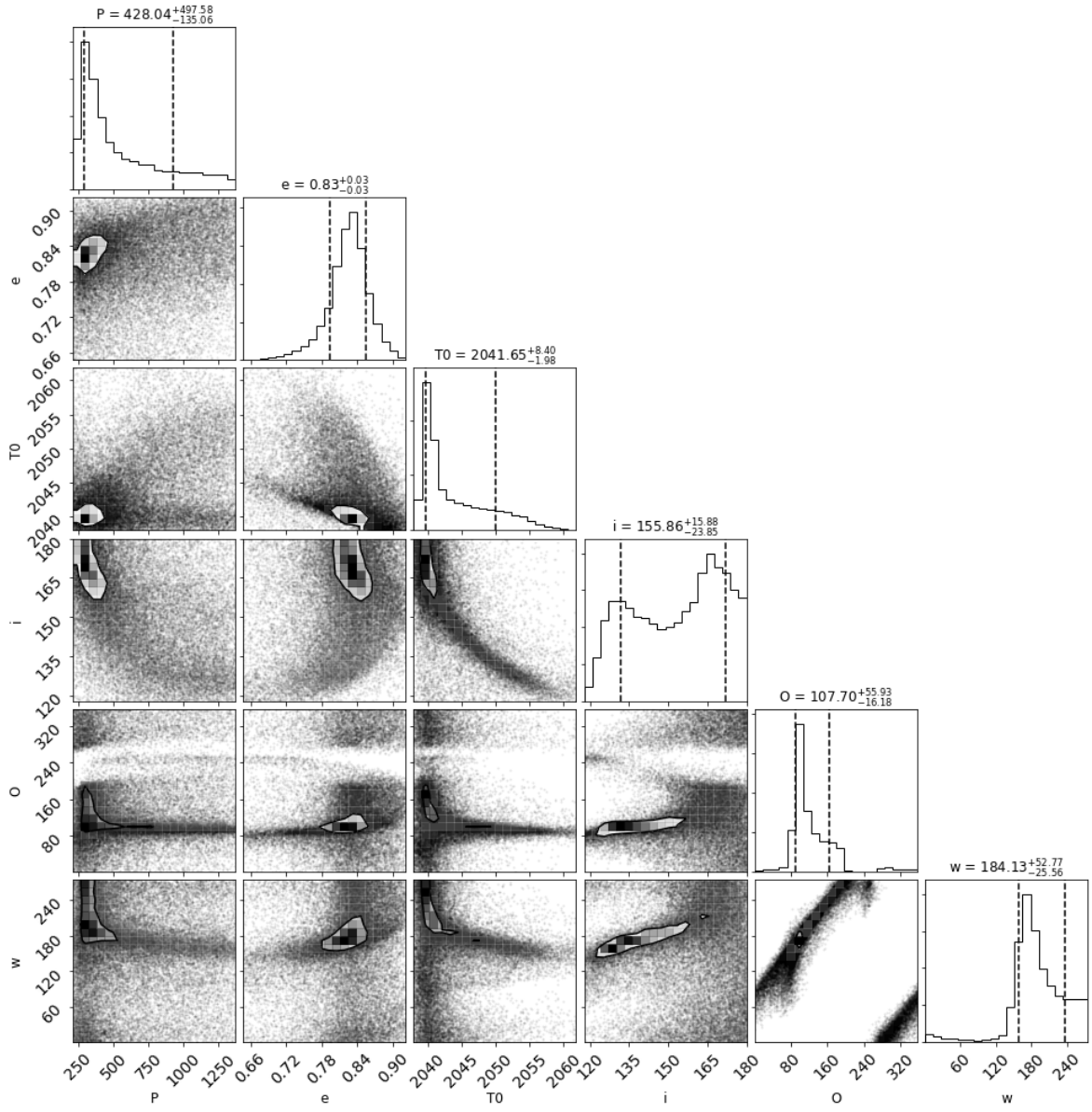

Figure 2.15: Corner plot showing the results of fitting the orbit of κ And b, including both astrometry and radial velocities. In this case, we use the typical flat priors in fit parameter space for easier comparison to previous work. Note that the use of these priors leads to a highly peaked prediction for T_0. Since velocity changes rapidly at this orbital phase, we will be able to test whether this prediction holds true in the next few years (Figure 2.18).

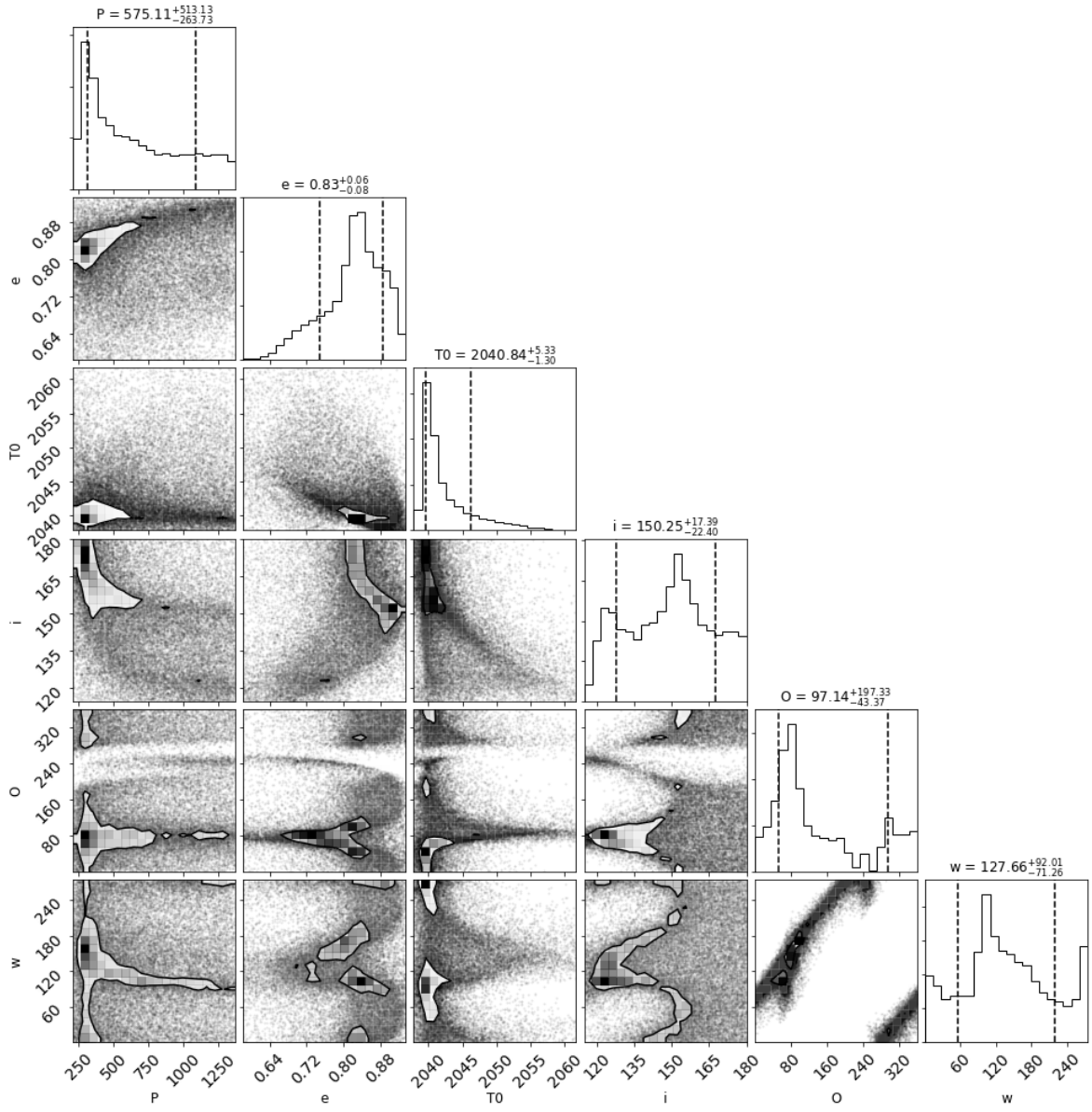

Figure 2.16: The same as Figure 2.15, but with no RV included in the fit. The results give values for orbital parameters consistent with previous fits found in the literature. Again, a secondary peak in Ω can be seen more prominently here around $\sim 270^o$ that is nearly absent in Figure 2.15. The addition of the RV eliminates this degeneracy in the orbit plane orientation (regardless of prior choice).

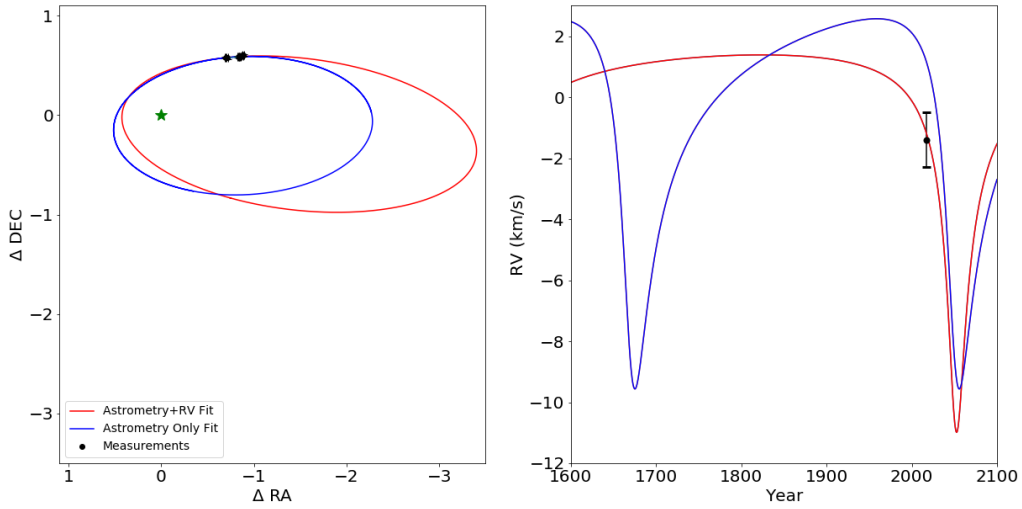

Figure 2.17: Best-fit orbits with (red) or without (blue) inclusion of the OSIRIS RV using the observationally-based prior. Because of the large parameter space allowed by the astrometry, the best-fits are used here only for illustrative purposes. The left panel shows the orbits on the plane of the sky while the right panel demonstrates the variation in relative RV of the planet with time. Including the RV increases the preferred eccentricity of the best-fit solution, though the astrometry drives solutions to high eccentricities regardless. Based on the right hand panel, the RVs clearly have more diagnostic power in the next several years than the astrometry. If the planet is indeed approaching periastron passage, a rapid decrease in the relative radial velocity is predicted.

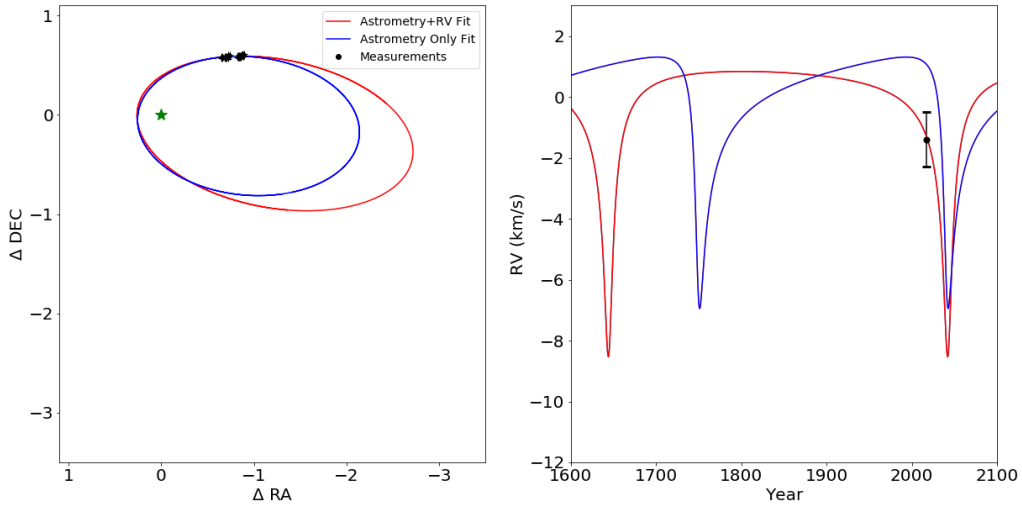

Figure 2.18: The same as Figure 2.17, but using flat orbit parameter priors. Either choice of prior yields preferred orbit solutions that approach periastron in the next several years, stressing the utility of more RVs.

Table 2.5: Derived orbit parameters for κ And B.

Fit Type	Global Minimum						Mean						1σ Range					
	P (yrs)	ecc	T_o (yr)	inc. (deg.)	ω deg.	Ω (deg)	P (yrs)	ecc	T_o (yr)	inc. (deg.)	ω deg.	Ω (deg)	P (yrs)	ecc	T_o (yr)	inc. (deg.)	ω deg.	Ω (deg)
Flat Priors Astrometry+RV	398.0	0.83	2042.5	152.1	186.4	104.4	428.0	0.83	2041.7	155.9	184.1	107.1	293.0 - 925.6	0.80 - 0.86	2039.7 - 2050.1	132.0 - 171.7	158.6 - 236.9	91.5 - 163.6
Flat Priors Astrometry Only	291.42	0.79	2040.85	156.2	68.5	149.6	576.1	0.83	2040.8	150.3	127.7	97.1	311.4 - 1088.24	0.75 - 0.89	2039.5 - 2046.2	127.9 - 167.6	56.4 - 219.7	53.8 - 294.5
Obs. Priors Astrometry+RV	576.6	0.78	2051.7	129.3	172.5	92.5	523.0	0.80	2049.9	132.0	175.9	94.1	293.0 - 975.2	0.72 - 0.85	2041.4 - 2060.4	119.9 - 113.1	158.4 - 200.2	86.4 - 163.6
Obs. Priors Astrometry Only	380.4	0.66	2050.8	127.3	150.7	78.1	468.7	0.78	2045.6	133.5	141.9	85.0	287.2 - 884.0	0.64 - 0.87	2040.3 - 2056.2	118.8 - 153.7	69.9 - 183.9	65.0 - 272.9

2.5 Discussion and Conclusions

Using moderate-resolution spectroscopy, we have greatly expanded our knowledge of the low-mass, directly imaged companion, κ And b. In recent years, most studies of the κ And system have led to the conclusion that it is young, as originally predicted by Carson et al. (2013). Our derivation of low surface gravity ($\log g$ <4.5) using our OSIRIS spectrum is another piece of evidence in favor of a young age. If we consider the age range adopted by Jones et al. (2016) of 47^{+27}_{-40} Myr, the predicted mass for a roughly ∼2050 K object range from ∼10–30 $M_{\rm Jup}$ (e.g., Baraffe et al. 2015). We note that our best-fit surface gravity of 3.8 is too low to be consistent with evolutionary models for this mass range, which predicts $\log g \approx$ 4–4.7. However, our uncertainties allow for gravities up to log(g)∼4.5. The OSIRIS data does not favor $\log g$ greater than 4.5, which argues for an age less than ∼50 Myr. Our derived radius is also on the low end of what is allowed by evolutionary models, which predict R = 1.3 R_{Jup} for older, more massive objects through R = 1.8 R_{Jup} for younger, lower mass objects. Our uncertainties again are sufficient to encompass this range. The implied bolometric luminosity is consistent with Currie et al. (2018), who note that it is similar to other young, substellar objects.

Additional constraints on the temperature, cloud properties, and radius in the future via additional photometry, spectra, or modeling could yield tighter constraints on the mass of κ And b. κ And b is an excellent candidate for moderate-resolution spectroscopy at shorter wavelengths to look for lines from higher atomic number species beyond carbon and oxygen. With future measurements of highly gravity sensitive lines, like potassium in the J-band if detectable, stronger limits can be placed spectroscopically on $\log g$, which will provide a more robust age. Further mass constrains could also come from astrometric measurements with *Gaia* or more radial velocity measurements that include velocity measurements for the star, although the precision of such RVs may be limited.

Given the size and separation of κ And b, its formation pathway is of considerable interest. Our measurement of C/O here provides one possible diagnostic of formation. We note that in a

number of recent works, it has been demonstrated that the C/O ratio is impacted by a variety of phenomena beyond formation location in the disk. These include the grain size distribution (Piso et al., 2015), migration of grains or pebbles (Booth et al., 2017), migration of planets themselves (Cridland et al., 2020), and whether the accreted material is from the midplane (Morbidelli et al. 2014; Batygin 2018). Current studies are therefore incorporating more chemical and physical processes into models to get a better idea of what impacts the C/O ratio and what exactly the ratio tells us about formation.

With these studies in mind, we turn to the C/O ratio we have measured for κ And b. Although our current uncertainties allow for somewhat elevated C/O ratios, the most likely scenario is that C/O is roughly consistent with the Sun. This result diagnostically points to a very rapid formation process, potentially through either gravitational instability or common gravitational collapse similar to a binary star system. The complication, however, is that the comparison must be made to the host star in order to draw definitive conclusions about formation. The C/O ratio of the host star, κ And A, has not been measured or reported in the literature. As a late B-type star, probing these abundances is challenging, although certainly possible (Takeda & Honda, 2016). However, the rapid rotation of κ And A ($\sim$162 km s^{-1}; Royer et al. 2007), may make abundance determinations difficult. High resolution optical spectroscopy for the star would be able to probe potential diagnostic lines, such as the OI triplet at 7771 Å. Until individual abundance estimates for C and O are available, however, we can only conclude that the evidence points to roughly similar values for the host star and the companion if the star has similar abundances to the Sun.

In terms of overall metallicity, the [Fe/H] abundance of κ And A was estimated by Wu et al. (2011) to be subsolar, [M/H] = $-0.32\pm$ 0.15. However, Jones et al. (2016) argue this is unlikely to be the true internal metallicity of the star, instead adopting a roughly solar abundance range of [M/H] = 0.00 ± 0.14 based on the range of metallicities in nearby open clusters. Interestingly, our slightly subsolar best-fit metallicity for κ And b may suggest that indeed the star is metal poor overall. A number of theoretical works have suggested that formation

via gravitational instability would preferentially occur around low metallicity stars. Metal poor gas allows for shorter cooling timescales, allowing planets to quickly acquire sufficient density to avoid sheering (e.g., Boss 2002; Cai et al. 2006; Helled & Bodenheimer 2011). Since metals are difficult to measure in high mass hosts like κ And A, direct metallicity measurements of the planets themselves could provide insight into measurements for the host star. We note that the derived abundances could be impacted by non-equilibrium chemistry effects in the *K*-band, and measuring atomic abundances can mitigate this issue and may be preferable (e.g., Nikolov et al. 2018). Additional metallicity measurements for directly imaged planets will also help probe the intriguing trend that the correlation of planet occurrence and metallicity breaks down at $\sim$4 M_{Jup} (Santos et al., 2017). The apparently low metallicity of κ And b is certainly consistent with this finding.

κ And b now represents a fourth case of a directly imaged planet, in addition to three of the the HR 8799 planets (Konopacky et al., 2013; Barman et al., 2015; Mollière et al., 2020), where the C/O ratio formation diagnostic did not reveal ratios that clearly point to formation via core/pebble accretion. The scenario certainly cannot be ruled out given the uncertainties in the data and the range of possible C/O ratios predicted by models (e.g., Madhusudhan 2019). Because of this uncertainty, other probes of formation will be needed to shed additional light on this fascinating population of companions. That includes the suggestion that the the high eccentricity of κ And b is a result of scattering with another planetary mass object. Our results cannot shed light on potential formation closer to the star using C/O as a diagnostic until we can improve our uncertainties. Since the C/O ratio is largely a function of the amount of solids incorporated into the atmosphere, it is possible that the massive size of these planets simply implies that they very efficiently and rapidly accreted their envelopes. This could have included enough solid pollution in the envelope to return the C/O ratio to the original value. Indeed, there are pebble accretion scenarios proposed in which it is possible to achieve slightly superstellar C/H and C/O, but stellar O/H ratios via significant accretion of large, metal-rich grains (Booth et al., 2017), which is consistent with our results for κ And b.

The next steps for the κ And system going forward will be confirmation of the high eccentricity solutions currently favored using more RVs, and continued monitoring with astrometry using consistent instrumentation to limit astrometric systematics. The strong CO lines and favorable contrast make κ And b an excellent candidate for high-resolution, AO-fed spectroscopy with instruments like KPIC on Keck, IRD on Subaru, or CRIRES on the VLT (e.g., Snellen et al. 2014; Wang et al. 2018a). We can also determine whether the bulk population of directly imaged planets show C/O ratios consistent with solar/stellar values by continuing to obtain moderate or high-resolution spectra of these companions. If the population of directly imaged planets shows C/O distinct from what has been seen with closer in giant planets probed via transmission spectroscopy, this could point to distinct formation pathways for these sets of objects.

Chapter 2, in full, is a reproduction of the material as it appears in The Astronomical Journal 2020, Hoch, K. K. W., Konopacky, Q. M., Barman, T. S., Theissen, C. A, Ruffio, J.-B., Brock, L., Macintosh, B., Marois, C., 160, 207. I (the dissertation author) was the primary investigator and author of this publication.

Chapter 3

Moderate-Resolution K-Band Spectroscopy of the Substellar Companion VHS 1256 b

We present moderate-resolution ($R \sim 4000$) K band spectra of the planetary-mass companion VHS 1256 b. The data were taken with the OSIRIS integral field spectrograph at the W.M. Keck Observatory. The spectra reveal resolved molecular lines from H_2O and CO. The spectra are compared to custom *PHOENIX* atmosphere model grids appropriate for young, substellar objects. We fit the data using a Markov Chain Monte Carlo forward modeling method. Using a combination of our moderate-resolution spectrum and low-resolution, broadband data from the literature, we derive an effective temperature of 1240 K, with a range of 1200–1300 K, a surface gravity of $\log g = 3.25$, with a range of 3.25–3.75 and a cloud parameter of $\log P_{cloud} = 6$, with a range of 6.0–6.6. These values are consistent with previous studies, regardless of the new, larger system distance from GAIA EDR3 ($22.2^{+1.1}_{-1.2}$ pc). We derive a C/O ratio of $0.590^{+0.280}_{-0.354}$ for VHS 1256b. Both our OSIRIS data and spectra from the literature are best modeled when using a larger 3 μm grain size for the clouds than used for hotter objects, consistent with other sources in the L/T transition region. VHS 1256 b offers an opportunity to look for systematics in the modeling process that may lead to the incorrect derivation of properties like C/O ratio in the high contrast regime.

3.1 Introduction

Direct imaging of exoplanets has revealed a population of Jupiter-like objects that orbit at wide separations ($\sim$10–100 au; Bowler, 2016; Nikolov et al., 2018; Vigan et al., 2021). In some cases, massive Jovians are found at separations of hundreds of au (e.g., Bailey et al., 2013). This population of widely-separated giants remains a puzzle for planet formation models. The orbits are too large for conventional core accretion models to make massive planets, while large-scale disk instabilities would create many more brown dwarf companions at wide separations than have been discovered in surveys around young stars (e.g., Rameau et al., 2013; Biller et al., 2013; Galicher et al., 2016; Nielsen et al., 2019; Vigan et al., 2021).

Directly imaged exoplanets are difficult to observe in detail because they are faint compared to their bright host stars. Young, free floating and/or widely separated substellar and planetary mass objects often share the same color space as directly imaged gas giants (Faherty et al., 2013; Liu et al., 2016). These objects are extremely useful because of the ease in observation and insight they provide into atmospheric properties of gas giant exoplanets.

Formation of molecules and condensates are the dominant opacity sources of the atmospheres of giant planets and brown dwarfs. Prominent molecules include H_2O, H_2, CO, CH_4, NH_3, CrH, FeH, and CaH and their absorption features establish much of the L and T spectral shapes. As these materials condense in the atmospheres, clouds are expected to form. Clouds are a nearly ubiquitous feature of substellar objects, but have remained difficult to model. The presence of clouds is a function of both temperature and surface gravity, which makes directly imaged companions, that can span the L/T transition, excellent candidates for cloud characterization.

Brown dwarfs have similar spectral features as young directly imaged planets, and therefore are excellent test cases for verifying modeling procedures that result in atmospheric characterization. In particular, brown dwarfs that are members of binary systems are extremely useful, as they offer a means to verify properties such as metallicity if their companion is stellar

(Wang et al., 2022). Additionally, since they formed from the same material, brown dwarfs that form in binary systems of two substellar companions should at least have the same relative composition. Many brown dwarfs also have existing constraints on effective temperature, surface gravity, and composition. Processes that impact the atmospheric abundances such as mixing and condensation vary with effective temperature and gravity, so it is important for those parameters to be constrained with independent data.

VHS J125601.92-125723.9b (VHS 1256 b, Gauza et al. 2015) is a wide orbit (8" separation) substellar companion to the late M dwarf binary star system VHS 1256-1257 AB (Stone et al., 2016). The age of this system has not been determined, but weak absorption from neutral gases (Na and K) and collision-induced absorption by H_2 detected in VHS 1256 b's atmosphere indicate low surface gravity and therefore suggests a young age (Gauza et al., 2015). Gaia EDR3 measured a new parallax for VHS 1256 AB b which yielded a new distance, $22.2^{+1.1}_{-1.2}$ pc, adjusted from the previous estimate 12.7±1.0 pc (Gauza et al., 2015). This change in distance has the potential to affect the temperature and mass measurements of VHS 1256 b. This object is also highly variable and can cause some uncertainty when interpreting atmospheric parameters. The rotation ($v \sin i$) of VHS 1256 b was measured by Bryan et al. (2018) to be $13.5^{+3.6}_{-4.1}$ km s^{-1}. The apparent redness of this object and previous modeling of the optical to mid infrared photometric data suggests that VHS 1256 b has a very cloudy atmosphere (Rich et al., 2016). Gauza et al. (2015) estimated that VHS 1256 b is an L7.0±1.5 object, right in the L/T transition. Miles et al. (2018) presented *L*-band spectra of the object that shows signs of weak methane absorption and a thick cloudy atmosphere. This companion is also a target in an ERS program for the James Webb Space Telescope (Hinkley et al., 2017). A summary of the VHS 1256 system parameters and photometry is given in Table 3.1.

Here, we present $R \sim 4000$ *K*-band spectra of VHS 1256 b using the OSIRIS instrument on the W.M. Keck Telescope. In Section 3.2 we report our observations and data reduction methods. In Section 3.3 we use atmosphere model grids and forward modeling Markov Chain Monte Carlo methods to determine the best-fit effective temperature, surface gravity, and metallicity of

both the VHS 1257 b and VHS 1256 AB. We use our best-fit parameters and *PHOENIX* models with scaled molecular mole fractions to derive a C/O ratio for VHS 1256 b and basic atmospheric parameters for the host star. In Section 3.4 we discuss the implications of our results and future work.

3.2 Data Reduction

VHS 1256 b was observed on 2017 June 10 with the OSIRIS integral field spectrograph (IFS) on the W.M. Keck I telescope (Larkin et al., 2006). We used the *K* broadband mode (1.965–2.381 μm) with a spatial sampling of 20 milliarcseconds per lenslet. Since the primary star in the system is faint (V$\sim$18), we used the Keck I facility laser guide star adaptive optics system to achieve close to diffraction-limited performance (Chin et al., 2012). The primary star was used as the tip/tilt reference (R$\sim$15), while the laser was used for all other corrections. We acquired the primary, and then offset to the location of the companion, since the OSIRIS field of view in 20 milliarcsecond mode is only $0.32'' \times 0.28''$. In total, we integrated on the object for 70 minutes (7 exposures of 10 minutes each, where we dithered up and down by a between exposures). Observations of an A0V telluric standard (HIP 67139) were obtained close in time to the data. We also obtained dark frames with exposure times matching our dataset. We did not obtain separate sky exposures, electing instead to nod the object up and down on the detector for efficiency and then use the nod pairs for sky subtraction. The data were reduced using the OSIRIS data reduction pipeline (DRP; Krabbe et al., 2004; Lockhart et al., 2019). Data cubes are generated using the standard method in the OSIRIS DRP, using rectification matrices provided by the observatory. At the advice of the DRP working group, we did not use the Clean Cosmic Rays DRP module (T. Do, priv. comm). We did not use scaled sky subtraction.

After extracting one-dimensional spectra for the telluric sources, we used the DRP to remove hydrogen lines, divide by a blackbody spectrum, and combine all standard star spectra for each respective night. Once the standard star spectra were combined, a telluric calibrator

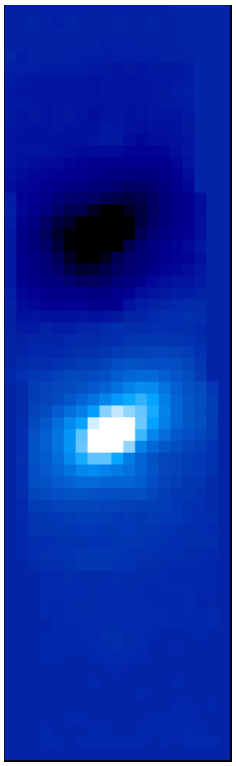

Figure 3.1: An example data cube image frame, collapsed in wavelength via median, from our OSIRIS VHS 1256 b data set. The field of view is 0.32″ x 1.28″. The dark spot represents the negative value from the companion subtraction at the other nod position. The bright spot shows the companion clearly visible without any need for speckle removal. The elongation of the PSF is due to the imperfect LGS AO correction, but does not impact the resulting extracted spectra, which are created by summing the spectra from multiple spaxels around the core of the PSF.

spectrum was obtained. The telluric correction for VHS 1256 b was then done by dividing the final combined telluric calibrator spectrum from all object frames.

Once the object data cubes are nod subtracted and fully reduced, we identify the location of the target. In high contrast observations with OSIRIS, the location of a companion can be challenging to find due to the brightness of the speckles. For VHS 1256 b, the starlight from the host star is not bright enough to impact the spectrum of the companion, and identification is straightforward (see Figure 3.1).

We extract the object spectrum using a box of 3×3 spatial pixels (spaxels). Once we extracted the VHS 1256 b spectra from each frame for all data, we then normalize each individual spectrum to account for PSF and background fluctuations. Finally, we median-

combine all 7 individual spectra. To calibrate the flux of our spectra we calculated the flux at each wavelength such that, when integrated, the flux matches the most recent K-band apparent magnitude (14.665 ± 0.01) from Gauza et al. (2015).

We note that the telluric correction in the blue portion of the spectrum appears to leave some residual telluric signal. In our previous work, simultaneous telluric correction was possible using the speckles from the early-type host stars (Wilcomb et al., 2020). This is not the case for the well-isolated VHS 1256b. We attempt to mitigate the impact of the imperfect telluric removal in our subsequent analysis.

Uncertainties were determined by calculating the RMS between the individual spectra at each wavelength. These uncertainties include contributions from statistical error in the flux of the planet as well as some additional error in the blue end of the spectrum due to the residual telluric features in this region. The OH sky lines are well-subtracted and have a negligible contribution to the uncertainties. The median uncertainty for our spectrum with the continuum included is $\sim$7%.

By removing the continuum, narrow spectral features are more easily analyzed by avoiding low spatial frequency errors that impact the overall continuum shape. We remove the continuum from our fully reduced and flux calibrated spectra using a similar continuum removal strategy we have employed in the past for OSIRIS data (e.g., Barman et al. 2015; Wilcomb et al. 2020). To remove the continuum, we apply a high-pass filter with a kernel size of 200 spectral bins to each of the individual spectra. Then we subtract the smoothed spectrum from the original spectra. Once all the individual spectra are continuum subtracted, we median combine them and find the uncertainties by calculating the RMS of the individual spectra at each wavelength. The median uncertainty on our flattened spectrum is 0.4%, much smaller than the uncertainty on the spectrum with the continuum included.

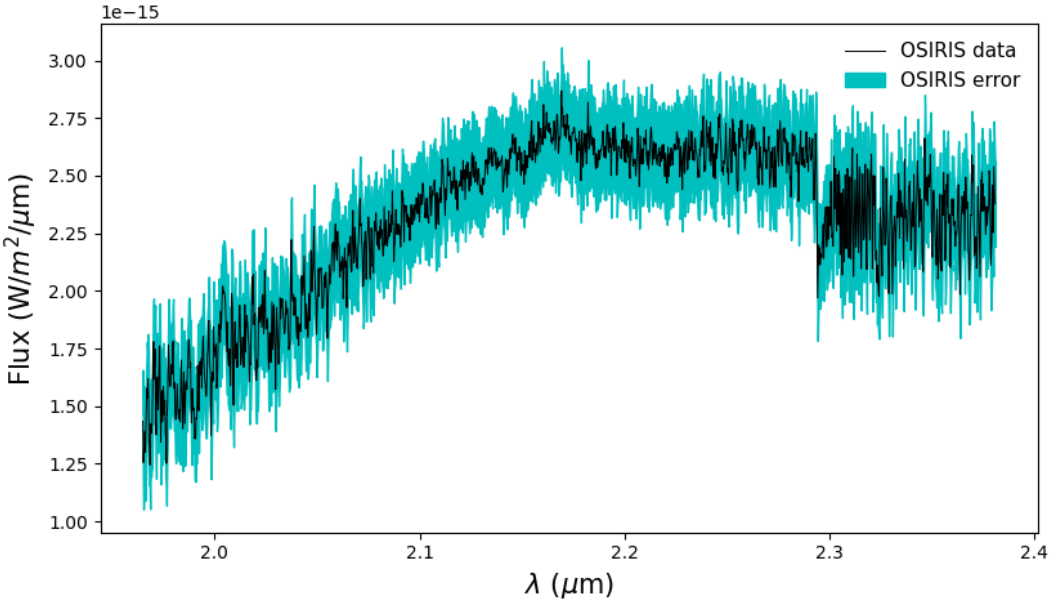

Figure 3.2: Our fully reduced, combined, and flux calibrated moderate-resolution OSIRIS *K*-band spectra of VHS 1256 b. The errors are derived from the RMS of the individual spectra at each wavelength. Such as error includes uncertainties in both the continuum and the lines, the former of which tends to be larger and is removed via continuum subtraction in portions of our analysis. These total spectral uncertainties are represented as a shaded blue region. The median uncertainty is $\sim$7% in flux. The CO bandhead is clearly visible at 2.3 μm.

3.3 Spectral Modeling

3.3.1 Synthetic Spectra

In order to determine the atmospheric properties of VHS 1256b, we use models computed through the *PHOENIX* model atmosphere code (Hauschildt et al., 1999). The atmospheric properties for young gas giants and brown dwarfs are notoriously complex, with cloud modeling being particularly challenging. In our modeling framework, we are able to parameterize clouds in several different ways. They are incorporated as a thick cloud layer with a log-normal ISM-like grain size distribution in all three types of cloud models; DUSTY (Allard et al., 2001), COND (Allard et al., 2001), and an Intermediate Cloud Model (ICM) (Barman et al., 2011). DUSTY models have inefficient gravitational settling so dust is still in the atmosphere, and COND models

Table 3.1: Summary of VHS 1256 AB b System

Parameter	Central Binary	Companion	Reference
Distance (pc)	$22.2^{+1.1}_{-1.2}$	-	a
Separation (arcsec)	0.109 ± 0.0018	8.06 ± 0.03	b,*c*
Projected Separation (au)	2.42 ± 0.0399	102 ± 9	b,*c*
Spectral Type	M7.5±0.5	L7.0±1.5	c
Apparent Magnitudes			
2MASS *J*-band	11.018±0.023	16.662±0.287	d
2MASS *H*-band	10.473±0.023	15.595±0.209	d
2MASS K_s-band	10.044±0.021	14.568±0.121	d
VHS *Y*-band	< 11.72	18.558±0.051	e
VHS *J*-band	< 11.36	17.136±0.020	e
VHS *H*-band	< 11.02	15.777±0.015	e
VHS K_s-band	< 10.42	14.665±0.010	e
Subaru/IRCS *L*-band	9.76±0.03	12.99±0.04	f

References. — (a) Dupuy et al. (2020), (b) Stone et al. (2016), (c) Gauza et al. (2015), (d) Skrutskie et al. (2006), (e) McMahon et al. (2013), (f) Rich et al. (2016)

have efficient gravitational settling therefore no dust is left in the atmosphere. For VHS 1256 b, we used an ICM approach that has a base pressure set by equilibrium chemistry. The vertical extent of the cloud is parameterized by a pressure value that, when above the value, allows the cloud particles number density to fall off exponentially. The cloud particle sizes follow a log normal distribution that is characterized by a median grain size. We will therefore refer to the custom grid constructed here as *PHOENIX-ICM* to distinguish it from other models based on the *PHOENIX* framework. We also used two other grids to fit the data; *PHOENIX-ACES*, the custom grid used for κ And b (Wilcomb et al., 2020), and *PHOENIX-HR8799*, the custom grid used in Ruffio et al. (2021). We explore the results of our choice of cloud model and describe the fits from a few other models in Section 2.5.

Our first goal is to constrain the temperature, surface gravity, and cloud parameters of VHS 1256 b. In order to do this, we must construct a model grid that spans the expected values of these parameters. In a number of previous works on VHS 1256 b, the temperature was estimated to be in the range of 800–1200 K and the surface gravity ($\log g$) 3.2–4.5 (e.g., Miles et al., 2018; Gauza et al., 2015).

Based on these measurements, we generated a custom *PHOENIX* grid. The details on the

computation of this grid are described in Barman et al. (2011, 2015), with the updated methane line list from Hargreaves et al. (2020) and the optical opacities from Karkoschka & Tomasko (2010). The grid spans a temperature range 800–2100 K, a $\log g$ range of 3.5–5.5 dex, and a cloud property range P_{cloud} dyne/cm^2 of 5×10^5–4×10^6, which encompasses the values previously reported for VHS 1256 b. Vertical mixing (Kzz) was modeled in Miles et al. (2018) and was determined to be $\sim 10^8$ cm^{2}s^{-1} because with a cooler object of about 1200 K some of the C will still be in CH_4, and therefore CO will not be constant with height. This custom grid also varied grain size, but initially we used a fixed mean grain size of 0.5 μm.

The synthetic spectra from the grid were calculated with a wavelength sampling of 0.05 Å from 1.4 to 2.4 μm. Each spectrum was convolved with a Gaussian kernel with a FWHM that matched the OSIRIS spectral resolution (Barman et al., 2011). Both flux calibrated and continuum subtracted data were modeled and analyzed. The synthetic spectra were flux calibrated and continuum subtracted using the same routines as the data.

3.3.2 Forward Modeling

To determine the best-fit model for each grid, we use a forward-modeling approach following Blake et al. (2010), Burgasser et al. (2016), Hsu et al. (2021), and Theissen et al. (2022) The effective temperature ($T_{\rm eff}$), surface gravity ($\log g$), and cloud parameter ($\log P_{cloud}$) are inferred using a Markov Chain Monte Carlo (MCMC) method built on the `emcee` package that uses an implementation of the affine-invariant ensemble sampler (Goodman & Weare, 2010; Foreman-Mackey et al., 2013). The assumptions and description of the MCMC calculations are described in Wilcomb et al. (2020).

We also forward modeled the primary, VHS 1256 AB, spectra from Gauza et al. (2015). The data span 0.47–1.35 μm, 1.48–1.78 μm, and 1.95–2.41 μm. Since they are a late-M binary pair, we used the Göttingen spectral library (Husser et al., 2013) that varies the effective temperature ($T_{\rm eff}$), surface gravity ($\log g$), and metallicity ([M/H]) and covers the range of values expected for an M star. The results show that the host binary has approximately solar

metallicity. The best fit parameters for VHS1256AB from K-band data are $T_{\rm eff} = 2756^{+13}_{-15}$ K, $\log g = 4.99^{+0.0076}_{-0.013}$, and [M/H] = $0.0093^{+0.012}_{-0.0063}$. For the short wavelength data the best fit parameters are $T_{\rm eff} = 2668^{+8}_{-7}$ K, $\log g = 3.57 \pm 0.060$, and [M/H] = 0.20 ± 0.040. The H-band data best fit parameters are $T_{\rm eff} = 2758^{+15}_{-18}$ K, $\log g = 3.92^{+0.090}_{-0.40}$, and [M/H] = $0.39^{+0.14}_{-0.35}$. Since there is no higher resolution data available for the host binary, our precision in metallicity or abundance measurements is limited and further discussion about the systematics in the uncertainties is in Section 3.3.3. We report the allowed values of these fits to be an effective temperature of 2661 – 2773 K, a surface gravity of 3.51 – 5.00, and an [M/H] of 0.0030 – 0.53. The full results of the fits are shown in Table 3.2.

Table 3.2: Summary of atmospheric parameters derived from MCMC fits for the Primary.

Spectra VHS 1256 b	Effective Temperature $T_{\rm eff}$ (K)	Surface Gravity $\log g$	Metallicity M/H
Göttingen PHOENIX Spectral Library			
Gauza Primary K-band	2756^{+13}_{-15}	$4.99^{+0.0076}_{-0.015}$	$0.0093^{+0.012}_{-0.0063}$
Gauza Primary Optical+J band	2668^{+8}_{-7}	3.57 ± 0.060	0.20 ± 0.040
Gauza Primary H-band	2758^{+15}_{-18}	$3.92^{+0.090}_{-0.40}$	$0.39^{+0.14}_{-0.35}$
Allowed Range of Values	2661 - 2773	3.51 - 5.00	0.0030 - 0.53

3.3.3 Temperature, Gravity, and Cloud Parameters

We ran our MCMC fitting procedure on both the flux calibrated spectrum and the continuum-subtracted spectrum of VHS 1256b. Objects like VHS 1256b that straddle the L/T transition are notoriously difficult to fit with an unconstrained MCMC, primarily due to the complexity of modeling the clouds at low surface gravities (e.g., Barman et al. 2011). Therefore, we constrained the bounds of the fits via two methods. First, we used previously derived literature values for temperature and surface gravity as a starting point for a plausible range of values (e.g., Gauza et al. 2015; Miles et al. 2018). Then, we plotted the models in those temperature ranges over the data to verify by-eye that the matches were reasonable before running the full MCMC. We therefore narrowed the prior ranges for the temperature to be between 1000-1300 K and a

$\log g$ between 3.0-3.5. The best-fit parameters for our flux calibrated data are $T_{\rm eff} = 1240^{+1}_{-2}$ K, $\log g = 3.25^{+0.01}_{-0.1}$, and $\log P_{cloud} = 6 \pm 0.01$. For the radius, which comes from the multiplicative flux parameter, we found R = 1.00 $\pm$ 0.02 R_{Jup}. For our continuum-subtracted data the best-fit parameters were $T_{\rm eff} = 1223^{+1}_{-2}1$ K, $\log g = 3.6^{+0.02}_{-0.01}$, and $\log P_{cloud} = 6.6^{+0.07}_{-0.05}$. Radii cannot be derived for the continuum-subtracted data. Figures 3.3 through 3.5 show the best-fit spectra overplotted on our data, the residuals from the fits, and the resulting corner plot from our MCMC analysis for the continuum-subtracted spectra.

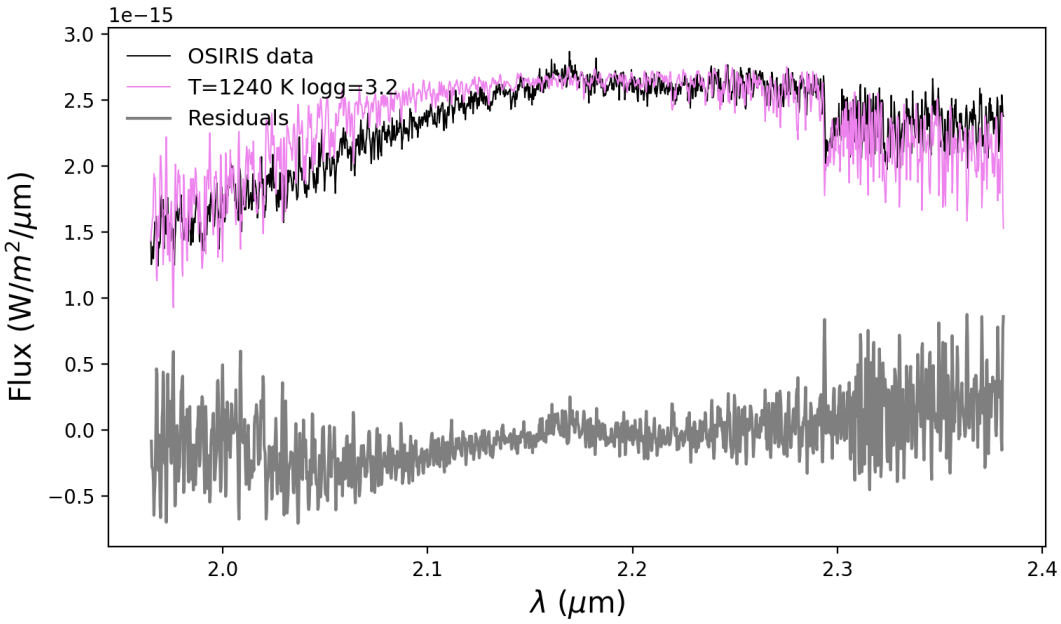

Figure 3.3: Our fully reduced, combined, and flux calibrated moderate-resolution OSIRIS *K*-band spectra of VHS 1256 b in black plotted alongside our best-fit model in pink. The residuals are shown below in gray. Even our custom *PHOENIX-ICM* had trouble fitting the continuum of our spectrum, specifically on the bluer end. However, this grid still provided the lowest residuals of any we considered.

In order to verify that the temperature estimates we derived from the OSIRIS spectra are robust, we ran our MCMC fitting code using the three custom *PHOENIX* grids on the Gauza et al. (2015) optical, *J*-band, *H*-band, and *K*-band spectra and the Miles et al. (2018) *L*-band spectra shown in Table 2. We adjusted our MCMC parameters for the Gauza et al. (2015) spectra by setting the line-spread function (LSF) to 229.77 km s^{-1}, which we derived from the data. We

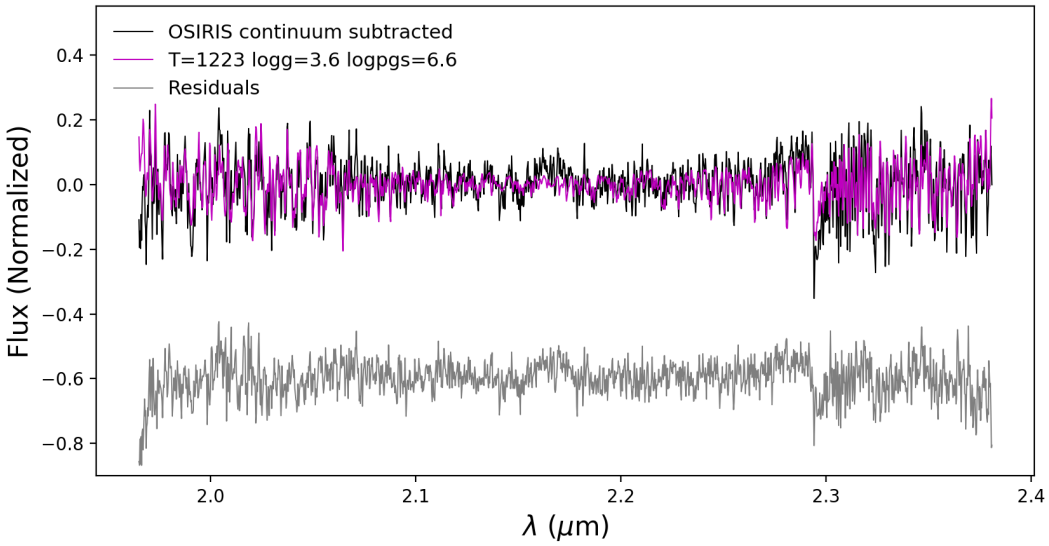

Figure 3.4: Our OSIRIS continuum subtracted K-band spectra in black plotted against our MCMC best-fit model in magenta. The bump in the center of the spectrum between 2.1 and 2.2 μm is due to residual telluric. By removing the continuum, we remove uncertainties that were tied to the continuum, thus the residuals for the flatted fit are much smaller.

fit each band in the data set separately and obtained $T_{\rm eff} = 1201^{+2}_{-1}$ K, $\log g = 4.81 \pm 0.06$, and $\log P_{cloud} = 6.59 \pm 0.01$ for the optical+J band spectra, $T_{\rm eff} = 1281^{12}_{-23}$ K, $\log g = 3.67^{+0.05}_{-0.04}$, and $\log P_{cloud} = 6.06 \pm 0.02$ for the K-band spectra, and $T_{\rm eff} = 1201^{+2}_{-1}$ K, $\log g = 3.51 \pm 0.01$, and $\log P_{cloud} = 5.97^{+0.02}_{-0.03}$ for the H-band spectra using our custom *PHOENIX-ICM* grid. We also adjusted our MCMC parameters for the Miles et al. (2018) by using an LSF of 106.95 km s^{-1} to account for the lower resolution of the data and obtained an $T_{\rm eff} = 1205^{+7}_{-4}$ K, $\log g = 3.53^{+0.03}_{-0.02}$, and $\log P_{cloud} = 6.23 \pm 0.02$.

Since our subsequent analysis of the chemical abundances of VHS 1256 b relies on knowledge of the temperature and gravity, we did additional modeling to look at the comparison between our custom cloud model grid and similar grids with different treatment of clouds. In addition to differences in cloud parameters, each grid of models incorporates different assumptions that lead to systematic differences in the output spectra for the same parameters such as temperature and gravity (e.g., Oreshenko et al. 2020). These systematics are not captured

in the uncertainties that come from each MCMC run output, and therefore those uncertainties, while reported here for completeness, are underestimates of the true uncertainties. These systematics also partially explain why fitting different parts of the spectra give slightly different best fit values, a very common occurrence for substellar object fits (e.g.,Cruz et al. 2018). We attempt to account for these systematics by looking at the range of values given from the three *PHOENIX* grids.

We incorporated our *PHOENIX-ACES* grid from Wilcomb et al. (2020) and the custom *PHOENIX-HR8799* grid from Ruffio et al. (2021) into our MCMC analysis code, and fit our OSIRIS spectrum using the same procedure described above. The best-fit using *PHOENIX-ACES* yielded $T_{\rm eff} = 1500 \pm 5$ K and $\log g = 3.92^{+0.06}_{-0.08}$. The *PHOENIX-HR8799* models generally provided poor matches to the higher resolution data, yielding much higher residuals than other grids. With this grid, we found $T_{\rm eff} = 820^{+2}_{-2}$ K and $\log g = 3.01^{+0.02}_{-0.01}$ as best-fit parameters. We found no fits with *PHOENIX-HR8799* that properly captured the continuum shape of our OSIRIS data. The fits to the continuum were generally poor across all grids, including the *PHOENIX-ICM* grid, and we speculated that this was due to our assumption about grain size in the models (see Section 3.3.3). We also fit the three Gauza et al. (2015) spectra and the Miles et al. (2018) spectra with these additional grids. The *PHOENIX-HR8799* grid did a poor job of fitting the Miles et al. (2018) spectra, while the *PHOENIX-ACES* grid fit the data well but gave unphysical parameters when the radii were derived shown in Table 3.3.3. Overall, the *PHOENIX-ICM* grid fit the spectra of this object the best and we adopt the values from these fits in this paper.

Table 3.3 shows the results for all atmospheric parameters derived in this paper. We use the range of best-fit values from the OSIRIS continuum-included data to define the adopted parameters for temperature, gravity, and cloud parameter, as the resolved line information coupled with the continuum offers the most constraints on those parameters. To derive more robust uncertainties on the atmospheric parameters that account for the systematics described above, we consider the range of values from all fits using the *PHOENIX-ICM* grid when deriving th allowed values for VHS 1256b. We adopt values of $T_{\rm eff} = 1240$ K, with a range of 1200–

1300 K, $\log g = 3.25$, with a range of 3.25–3.75, and $\log P_{cloud} = 6.0$, with a range of 6.0–6.6. For radius, we use the median value from the OSIRIS continuum-included data and the Gauza et al. (2015) spectra to arrive at $R = 1.0\ R_{Jup}$, with a range of 1.0–1.2 R_{Jup}. This yields an implied bolometric luminosity of $\log(L/L_{\odot}) = 4.67$, with a range of 4.60 to 4.70. These values are all in excellent agreement with previous studies (Gauza et al., 2015; Miles et al., 2018).

Cloud Grain Size

VHS 1256 b is an L/T transition object, and these objects spectra are strongly impacted by the depth of clouds and the grain size in the atmosphere (Brock et al., 2021). Since our custom *PHOENIX-ICM* grid also varied in grain size, we explored different mean grain sizes to get a better fit to the continuum in our OSIRIS data, as well as a better match to data in all wavebands. We held all other parameters constant, except for the multiplicative factor that is a proxy for radius, and allowed the mean grain size to vary from 0.5 μm to 3 μm. For our OSIRIS data, the best fit grain size was about $3^{+0}_{0.1}\mu$m, which did hit the edge of our grid. For the Gauza et al. (2015) spectra, the best fit grain size was $0.51^{+0.02}_{-0.0094}\mu$m at the short wavelengths, $0.50^{+0.010}_{-0.0048}\mu$m for the H-band spectrum, and $0.99^{+0.018}_{-0.032}$ for the K-band spectrum. The best fit grain size for the Miles et al. (2018) spectrum was $0.51^{+0.11}_{-0.01}\mu$m.

Since the fits to the short and long wavelength data yielded different preferred grain sizes than the OSIRIS data, we examined both 0.5 μm and 3.0 μm models across the full range of available wavelengths simultaneously. Figure 3.2 shows all available spectral and photometric data for VHS 1256 b. Overplotted are the two *PHOENIX-ICM* models with two different grain sizes, 0.5 μm and 3 μm. The models are scaled to match the continuum flux at K-band, which in turn is derived using the K-band magnitude in Gauza et al. ($K_s = 14.665 \pm 0.01$; 2015). First, we note that the lower resolution K band spectra from Gauza et al. (2015) spectra are a good overall match to the OSIRIS data. We note that when we look at the model in comparison to the flux calibrated shorter wavelength data, the 3 μm grain size model is a good match overall though not a perfect match to the continuum shape. However, the 0.5 μm model, the model

strongly underpredicts the short wavelength flux if it is scaled to match K band. This means that the best-fit of 0.5 μm at these short wavelengths was dependent on scaling the radius to much larger values was required for the K band. Indeed, with a the best-fit value for K band is a radius of $\sim$1 R_{Jup}, whereas the best fit at short wavelengths with a small grain size is $\sim$1.4 R_{Jup}. This implies that the fits were being pulled by the continuum shape when performed individually, and a comprehensive look at data at all wavelengths is more appropriate for determining the grain size. We do note that in the case of the long wavelength data from Miles et al. (2018) spectra and the photometry from Rich et al. (2016), the red side of the spectrum matches the 0.5 μm model better, and the radius is consistent with K band and roughly the same for either grain size. However, the overall shape of the Miles et al. (2018) spectrum does not match either model. Taken together, we conclude that a larger median grain size of 3.0 μm is appropriate for this object.

3.3.4 Mole Fractions of CO, H_2O, and CH_4

With best fit values for temperature, surface gravity, and clouds, we can derive abundances of CO, H_2O, and CH_4 using our OSIRIS K-band spectra. Once best fit values were determined for $T_{\rm eff}$, $\log g$, and $\log P_{cloud}$, we fixed those parameters to generate a grid of spectra with scaled mole fractions of these molecules, which are visible in the K-band (Barman et al., 2015). We used solar metallicity for this grid because there is no evidence for non-solar metallicity. Therefore, the unscaled mixing ratios in this grid will match the composition and mole fractions of the Sun. The molecular abundances of CO, CH_4, and H_2O were scaled relative to their initial values from 0 to 1000 using a uniform logarithmic sampling, resulting in 25 synthetic spectra. We fit for the mole fraction of H_2O first, holding CO and CH_4 at their initial values. Next, the H_2O mole fraction was set to its nominal value, and we fit for scaled CO. We did the same analysis for CH_4.

Figure 3.7 shows the resulting χ^2 distribution as a function of CO, H_2O, and CH_4 mole fraction. The models with the lowest χ^2 when compared to the flattened data gave us the best-fits for both H_2O and CO. For CH_4, there is no change in χ^2 with any change in the mole fraction,

Table 3.3: Summary of atmospheric parameters derived from MCMC fits.

Spectra VHS 1256 b	Effective Temperature $T_{\rm eff}$ (K)	Surface Gravity $\log g$	Cloud Layer $\log P_{cloud}$	Grain size μm	Radius ($R_{\rm Jup}$)	Luminosity $\log_{10}\left(\frac{L}{L_\odot}\right)$
PHOENIX-ACES						
OSIRIS Including Continuum	1500^{+5}_{-5}	$3.92^{+0.06}_{-0.08}$	n/a	n/a	0.64	–4.73
OSIRIS Continuum Subtracted	1500^{+5}_{-5}	$4.47^{+0.01}_{-0.02}$	n/a	n/a	n/a	n/a
Gauza K-band	1839^{+6}_{-7}	$4.83^{+0.01}_{-0.02}$	n/a	n/a	0.41	–4.76
Gauza Optical+J band	1659^{+3}_{-3}	$3.72^{+0.01}_{-0.01}$	n/a	n/a	0.52	–4.73
Gauza H-band	1658^{+2}_{-2}	$4.65^{+0.02}_{-0.02}$	n/a	n/a	0.54	–4.70
Miles L-band	1096^{+12}_{-13}	$4.38^{+0.11}_{-0.13}$	n/a	n/a	1.18	–4.74
PHOENIX-ICM						
OSIRIS Including Continuum	1240^{+1}_{-2}	$3.25^{+0.01}_{-0.1}$	6.0 ± 0.01	3.0 ± 0.1	1.0	–4.67
OSIRIS Continuum Subtracted	1223^{+1}_{-2}	$3.6^{+0.02}_{-0.01}$	$6.6^{+0.07}_{-0.05}$	$2.9^{+0.001}_{-0.01}$	n/a	n/a
Gauza K-band	1281^{+12}_{-23}	$3.67^{+0.05}_{-0.04}$	6.06 ± 0.02	$0.99^{+0.018}_{-0.032}$	0.92	–4.69
Gauza Optical+J-band	1201^{+2}_{-1}	$4.81^{+0.06}_{-0.06}$	6.59 ± 0.01	$0.51^{0.02}_{0.0094}$	1.2	–4.57
Gauza H-band	1201^{+2}_{-1}	$3.51^{+0.01}_{-0.01}$	$5.97^{+0.02}_{-0.03}$	$0.05^{+0.010}_{-0.0048}$	1.18	–4.58
Miles L-band	1205^{+7}_{-4}	$3.53^{+0.03}_{-0.02}$	6.23 ± 0.02	$0.51^{+0.11}_{-0.01}$	1.13	–4.61
PHOENIX-HR8799						
OSIRIS Including Continuum	820^{+2}_{-2}	$3.01^{+0.02}_{-0.01}$	5.7^{+0}_{-0}	n/a	2.9	–4.46
OSIRIS Continuum Subtracted	1300^{+1}_{-2}	$3.0^{+0.02}_{-0.0}$	$6.0^{+0.01}_{-0.01}$	n/a	n/a	n/a
Gauza K-band	1298^{+1}_{-3}	$3.28^{+0.02}_{-0.02}$	$5.7^{+0.01}_{-0.0}$	n/a	0.9	–4.68
Gauza Optical+J-band	1097^{+17}_{-21}	$3.28^{+0.28}_{-0.16}$	$5.96^{+0.14}_{-0.13}$	n/a	1.8	–4.37
Gauza H-band	1031^{+9}_{-10}	$3.01^{+0.02}_{-0.01}$	$5.84^{+0.04}_{-0.03}$	n/a	1.8	–4.48
Miles L-band	836^{+7}_{-5}	$3.06^{+0.01}_{-0.01}$	$5.71^{+0.02}_{-0.01}$	n/a	2.1	–4.71
Adopted Values	1240	3.25	6.0	3.0	1.0	-4.67
Allowed Range of Values	1200 - 1300	3.25 - 3.75	6.0 - 6.6	1.0 - 3.0	1.0 - 1.2	-4.60 - -4.70

⁻Based on our fitting and a comparison of all datasets, we have chosen to adopt the best-fit values from the PHOENIX-ICM fit to the OSIRIS data with the continuum included. However, we allow for uncertainties that encompass the range of most fits to all datasets using the PHOENIX-ICM grid, excluding the surface gravity value from the Gauza et al. (2015) optical data, which is an outlier.

suggesting that if any methane is present in the spectrum, it is below the detection threshold of our data. We exclude CH_4 from further analysis. The best fit for H_2O had a scaling of $0.215^{+0.784}_{-0.187}$, and the best fit for CO had a scaling of $0.599^{+1.061}_{-0.384}$. To calculate the 1-σ uncertainties in each mole fraction value, we used the values from models within ± 1 of our lowest χ^2.

Because of the potential issues with telluric correction in the blue side of the spectrum mentioned in Section 3.2, we explored the mole fractions on different portions of the spectra, splitting it in half and performing the fit again. Shown in the left panel of Figure 3.8, for the first half of the spectrum, the best fit H_2O mole fraction is 0.215 and CO is unchanging as there are no CO features in this section of the spectra. For the second half of the OSIRIS spectra, shown in right panel of Figure 3.8, the H_2O scaled mole fraction is higher at 0.599 and the uncertainties encompass the lowest χ^2 from the full spectrum analysis. The lowest χ^2 CO matches the values

found when fitting the full spectrum (Figure 3.7). Because of concerns about the blue half of the spectrum, we elect to use the C and O values from the second half of the spectrum. This yields an H_2O mole fraction of $0.599^{+0.401}_{-0.384}$ and a CO mole fraction of $0.599^{+1.061}_{-0.384}$.

3.3.5 C/O Ratios

In our previous work, we have used OSIRIS data to constrain the C/O ratios of directly imaged companions to massive stars such as HR 8799 b, c, and d, and κ Andromedae b (e.g., Konopacky et al. 2013; Wilcomb et al. 2020; Ruffio et al. 2021). For giant planets formed by rapid gravitational instabilities, their atmospheres should have elemental abundances that are the same as their host stars (Helled & Schubert, 2009). If giant planets form by a multi-step core accretion process, it has been suggested that there could be a range of elemental abundances possible (Öberg et al., 2011; Madhusudhan, 2019). In this scenario, the abundances of giant planets' atmospheres formed by core/pebble accretion are highly dependent on the location of formation relative to CO, CO_2, and H_2O frost lines and the amount of solids acquired by the planet during runaway accretion phase. This can be diagnosed using the C/O ratio.

For VHS 1256 b, a substellar companion to a small binary pair, it is unclear if C/O is a useful formation diagnostic, as it is likely to have formed like a binary star rather than a planet (see Section 3.4). However, we still compute the ratio here and discuss the implications below.

The C/O ratio dependence on atmospheric mole fractions (N) is

$$\frac{C}{O} = \frac{N(CH_4)+N(CO)}{N(H_2O)+N(CO)},$$

and for small amounts of CH_4, as in VHS 1256 b's case, the C/O ratio can be determined by H_2O and CO alone (Barman et al., 2015). The C/O ratio we derive for VHS 1256 b is $0.590^{+0.280}_{-0.384}$. The large uncertainties encompass potential systematics and any differences in C/O ratio from the two halves of the spectrum. Variability of the object is unlikely to affect the measurement of C/O because CO is formed higher in the atmosphere than the predicted location of cloud decks.

The variability at K band has been shown to be less significant than at other wavelengths (e.g., Vos et al. 2019; Bowler et al. 2020). Figure 3.9 shows our lowest χ^2 model in the center panel and two extreme cases to illustrate the sensitivity our OSIRIS moderate resolution spectra has to the C/O ratio.

3.4 Discussion and Conclusions

Moderate resolution spectroscopy has expanded our knowledge of young directly imaged planet atmospheres. VHS 1256 b provides an interesting diagnostic because of the low contrast between the companion and the host system, and the thick cloudy atmosphere. Our results of $T_{\rm eff}$ = 1240 K, with a range of 1200–1300 K, and $\log g$ = 3.25, with a range of 3.25–3.75 agree with the results from Gauza et al. (2015) that posit VHS 1256 b is a low surface gravity object and is likely a planetary mass object in a youthful system. Our effective temperature is also in agreement with the literature regardless of the new distance measured by Gaia EDR3, $22.2^{+1.1}_{-1.2}$ pc, which changed the distance from 12.7±1.0 pc (Gauza et al., 2015). Dupuy et al. (2020) also found a distance 22.22 ± 1.19 pc from CFHT parallax measurements. We did not detect methane in our *K*-band spectra, which is in agreement with very weak methane absorption in the *L*-band spectra pointing towards non-equilibrium chemistry from Miles et al. (2018).

Our OSIRIS data on VHS 1256 b, coupled with data from the literature, preferred a thick-cloud model, $\log P_{cloud}$ = 6.0 with a range of 6.0–6.6, with a 3 μm mean grain size. Recent works have demonstrated that earlier L-type objects have higher-altitude clouds with smaller grains (0.25–0.50 μm), and later T-type objects exhibit deeper clouds and larger grains ($\geq$ 1 μm; Brock et al. 2021). We conclude that VHS 1256 b has deep clouds with a large mean grain size that is consistent with being near or just beyond the L/T transition, as indicated by its L7 spectral type.

Cloudy atmospheres of these Jovian-like objects are not well understood. Data at longer wavelengths can more deeply probe these cloud parameters and can inform the models to better

understand the processes occurring in cloudy giant planet atmospheres. VHS 1256 b is also extremely variable with near infrared photometry in 2MASS J, H, and K/K_s that varies by $\sim$37, $\sim$13, and $\sim$3 percent respectively (Miles et al., 2018). This can lead to different colors and flux calibrations that can influence interpreted atmospheric parameters. Understanding the variability of this object is important for further constraints on effective temperature and other atmospheric parameters. Our derivation of cloud properties, including a notional grain size distribution, will inform studies of variability of VHS 1256 b.

Formation of objects in the gas giant planet mass regime is of considerable interest, whether the companion orbits a low or high mass star. Formation diagnostics such as C/O ratio can provide context and potentially point to a formation pathway, although interpretation of the C/O ratio is complicated by a variety of phenomena (e.g., Madhusudhan 2019). The mass ratio of the system is 0.16, which is significantly larger than other directly imaged planets such as HR 8799 ($q \sim 5 \times 10^{-3}$; Fabrycky & Murray-Clay 2010) suggesting that the companion was likely too large to form in a protoplanetary disk around the primary (Rich et al., 2016). In measuring the C/O ratio here for VHS 1256 b, we seek instead to use observations of a similar object to the directly imaged planets to look for systematics in our modeling that could suggest any biases in computation of C/O. We derived a C/O ratio of $0.590^{+0.280}_{-0.384}$ for VHS 1256 b. Our finding of a roughly solar C/O ratio implies that these systematics are not present, which would be suggested by a ratio that is very different from solar. An unusual C/O ratio compared to the stellar value in a low mass binary is unexpected, and would suggest issues with modeling L/T transition objects. It is likely that VHS 1256 b formed like a binary star rather than a planet. There are studies that claim metallicity measurements could constrain formation location for these types of objects, but future work is needed to obtain these measurements for the host binary and the wide orbit companion (Liu et al., 2021). While we do not measure a C/O ratio for the host star because we did not have moderate resolution spectroscopy for it, there is no indication that a non-solar metallicity is required to describe the spectra in hand (Gauza et al., 2015). Thus, we are confident our methodology is sound and reliably provides C/O ratios for directly imaged companions.

Indeed, Figure 3.9 shows that very large or small C/O ratios are easily probed and ruled out by moderate-to-high resolution data, and are thus more trustworthy than values computed on low resolution spectra.

VHS 1256 b now represents an eighth case of an imaged planetary mass object, in addition to the four HR 8799 planets (Konopacky et al., 2013; Barman et al., 2015; Mollière et al., 2020; Ruffio et al., 2021), κ And b (Wilcomb et al., 2020), HIP 65426 b (Petrus et al., 2021), and TYC 8998-760-1 b (YSES-1 b Zhang et al. 2021), where the C/O ratio formation diagnostic did not reveal ratios that clearly point to formation via core/pebble accretion. The scenario cannot be completely ruled out given the uncertainties in the data and the range of possible C/O ratios predicted by models (e.g., Madhusudhan 2019). Therefore, other probes of formation such as the ^{12}CO/^{13}CO isotope ratio (Zhang et al., 2021) and metallicity, will be needed to shed more light on this intriguing population of giant companions.

VHS 1256 b has already been targeted with a higher resolution instrument, NIRSPEC at the Keck II 10 m telescope, which allowed for measurements of radial velocity and rotational velocity (Bryan et al., 2018). The next steps for the VHS 1256 system will be space-based spectroscopy to verify the C/O ratio and other atmospheric properties. VHS 1256 b is a target for the High Contrast Imaging of Exoplanets and Exoplanetary Systems with JWST Early Release Science (ERS) Program (Hinkley et al., 2017). VHS 1256 b will be studied using NIRSpec and MIRI to analyze the atmosphere at longer wavelengths to constrain non-equilibirum chemistry, C/O ratio, and variability of the object. We can also determine whether the bulk population of directly imaged planets show C/O ratios consistent with solar/stellar values by continuing to obtain moderate- or high-resolution spectra of these wide orbit, self-luminous companions. If the population of these objects show distinct C/O from closer in transit giant planets, this could point towards differing formation pathways for these companions.

Chapter 3, in full, has been accepted and is in preparation for publication of the material as it may appear in The Astronomical Journal, 2022, Hoch, K. K. W., Konopacky, Q. M., Barman, T. S., Theissen, C. A, Brock, L., Perrin, M. D., Ruffio, J.-B. Macintosh, B., Marois, C. I (the

dissertation author) was the primary investigator and author of this publication.

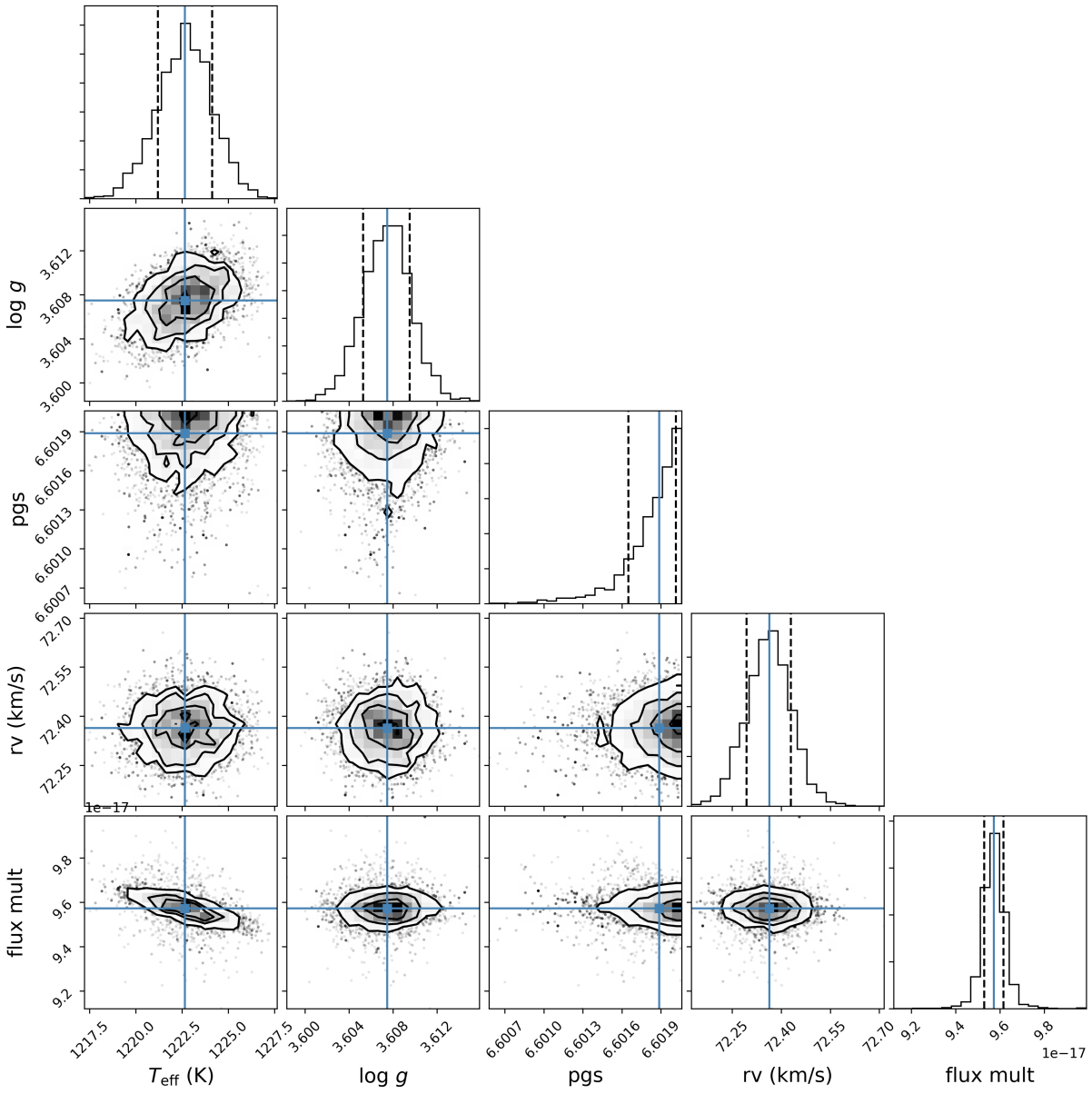

Figure 3.5: Corner plot from our MCMC fits for our continuum subtracted OSIRIS K-band spectra. The diagonal shows the marginalized posteriors. The covariances between all the parameters are in the corresponding 2-d histograms. The blue lines represent the 50 percentile, and the dotted lines represent the 16 and 84 percentiles. The "flux mult" corresponds to the dilution factor that scales the model by $(radius)^2(distance)^{-2}$. Our fit prefers a value near the edge of the grid for pgs, or, P_{cloud}.

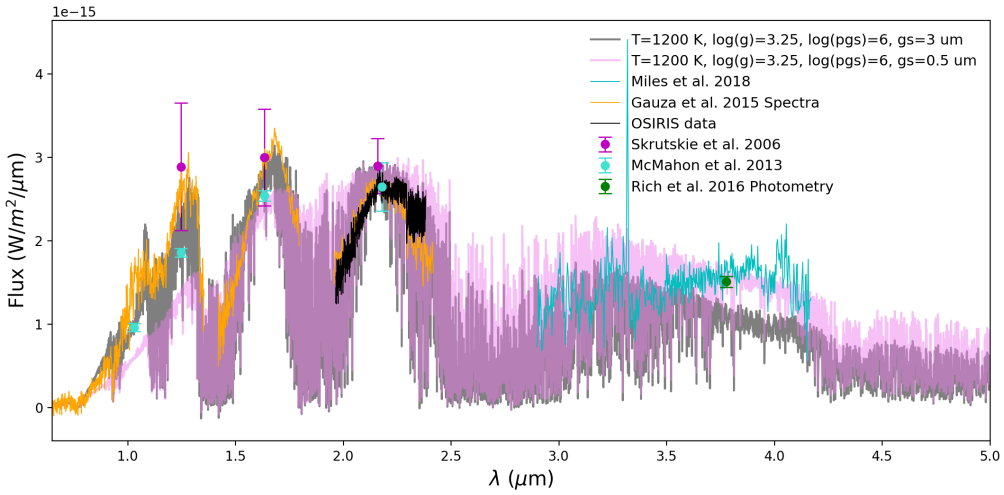

Figure 3.6: Our fully reduced, combined, and flux calibrated moderate-resolution OSIRIS K-band spectra of VHS 1256 b in black, plotted alongside our best fit model with two different grain sizes, 3μm in gray and 0.5μm in pink, and spectra from Miles et al. (2018) in blue, spectra from Gauza et al. (2015), and magnitudes from Rich et al. (2016), Skrutskie et al. (2006), and McMahon et al. (2013). The 3 μm grain size model fits the majority of the data except for the red end of the L-band spectra and the Rich et al. (2016) photometry point. The 0.5 μm grain size model underpredicts the flux in the optical, J-, and H-band, but does fit the L-band spectra and photometry point. We adopt the 3 μm model as the best-fit for the majority of the available data.

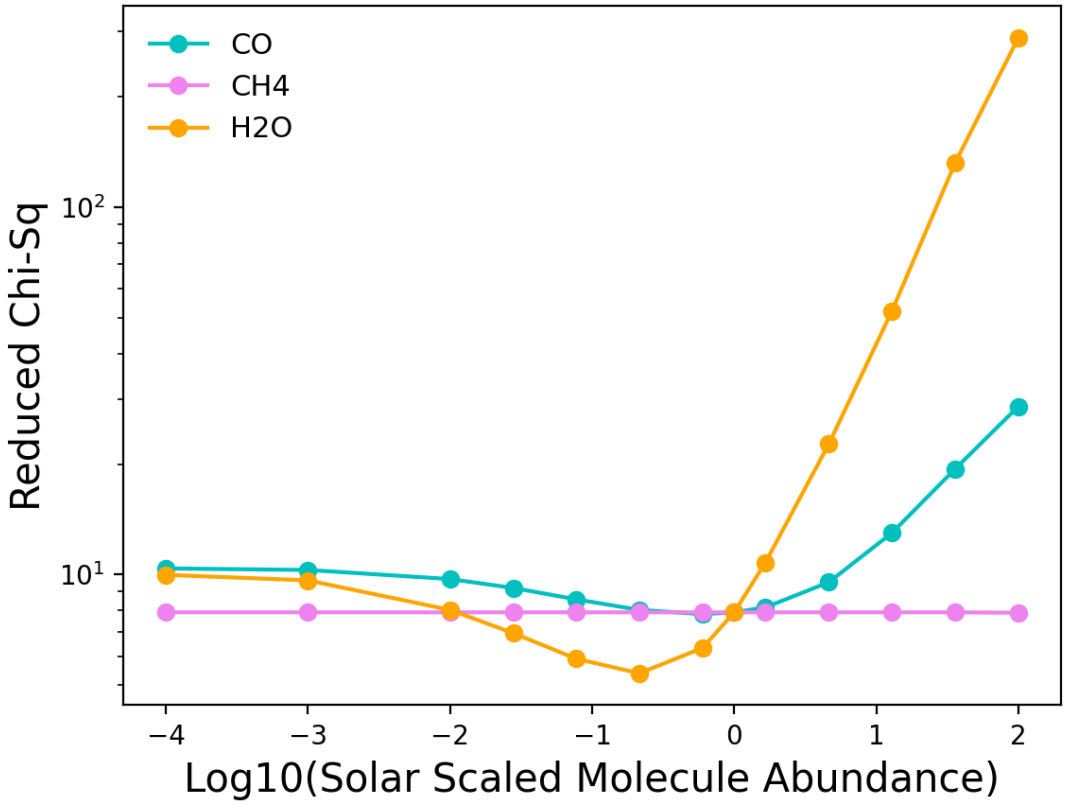

Figure 3.7: Results of $T_{\rm eff}$ = 1240 K, $\log g$ = 3.25, $\log P_{cloud}$ = 6, and grain size = 3 μm model fits with varying mole fractions for both H_2O, CO, and CH_4 to our continuum-subtracted OSIRIS spectrum. The mole fractions are given in units relative to the ratio in the Sun, such that a value of zero implies the solar value. The scalings of CO prefer solar/subsolar and the scalings of H_2O prefer values subsolar. From these fits we find C/O = $0.869^{+0.09}_{-0.24}$.

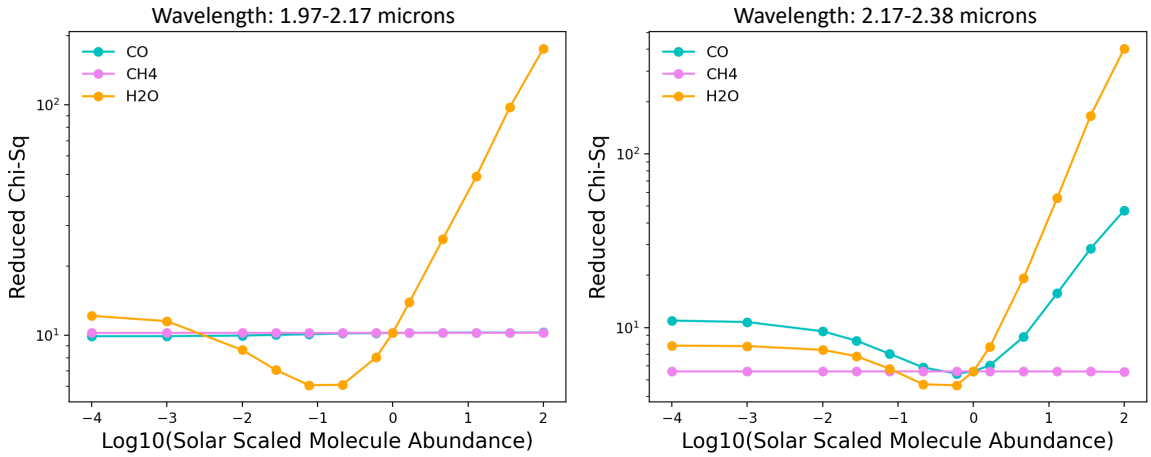

Figure 3.8: **Left:** The results of our χ^2 analysis on the first half of our continuum subtracted OSIRIS data. The CO abundances vary minimally during this analysis because of the lack of CO lines in the first half of our spectra. The best-fit water is still subsolar, with the lowest χ^2 values not including solar. **Right:** The results of our χ^2 analysis on the second half of our continuum subtracted OSIRIS data. The values allowed by the χ^2 analysis include the solar abundance model, with the best-fit H_2O molecular abundance being slightly subsolar.

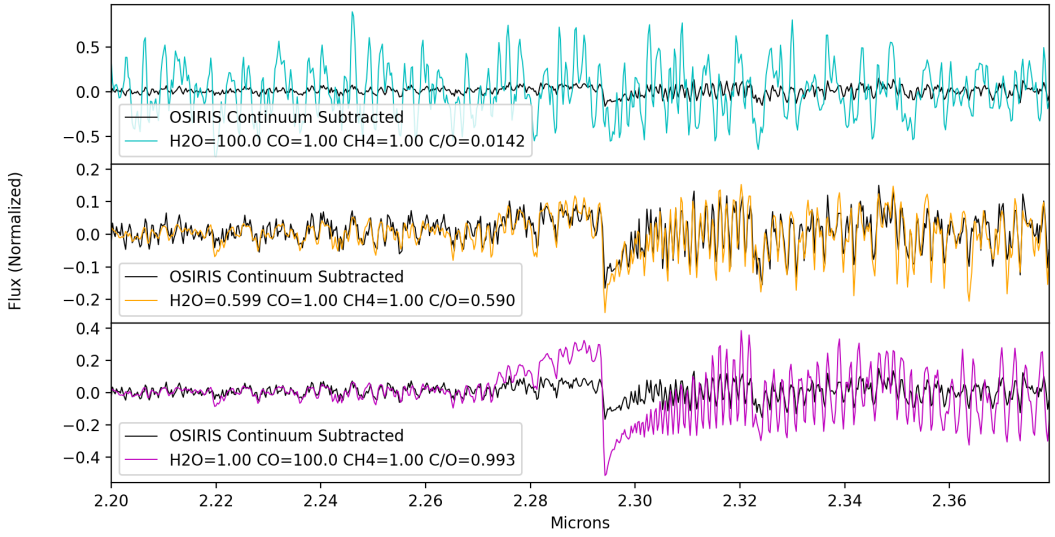

Figure 3.9: Our fully reduced, combined, and continuum subtracted moderate resolution OSIRIS *K*-band spectra of VHS 1256 b plotted alongside three models of T=1240 K and $\log g$=3.2 with varying C/O. The top panel shows the super-solar H_2O model with C/O=0.0142 in blue. The middle panel shows our best fit model with subsolar H_2O and solar CO and CH_4, which gives C/O=0.590. The bottom panel shows a supersolar CO model with C/O=0.993. This demonstrates how well moderate resolution spectroscopy can constrain C/O ratios of planetary mass objects.

Chapter 4

Directly Imaged Planets: C/O Ratio Formation Diagnostic and Comparisons to other Exoplanet Populations

We present moderate resolution ($R \sim 4000$) K band spectra of the substellar companion HD 284149 b. The data were taken with the OSIRIS integral field spectrograph at the W.M. Keck Observatory. We used a Markov Chain Monte Carlo forward modeling approach coupled with models from Husser et al. (2013) to fit our moderate resolution spectra. We derive an effective temperature of $T_{\rm eff}$ = 2469 K, with a range of 2443–2624 K, a surface gravity of $\log g$ = 4.58, with a range of 4.27–4.98, and a metallicity [M/H] = 0.57, with a range of 0.04–0.83. These values are in agreement with previous studies done by Bonavita et al. (2014, 2017). We derive a C/O of $0.737^{+0.148}_{-0.442}$ for HD 284149 b. Given the fairly large number of C/O ratios measured for directly imaged planets, we can now begin to look at the population as a whole in comparison to closer in planets. We therefore compare all measured C/O ratios from our work and from the literature for directly imaged planets with those available for transiting exoplanets. There seems to be a trend in C/O ratio with companion mass ($M_{\rm Jup}$), with a break seen around 4 $M_{\rm Jup}$. We ran a Kolmogorov-Smirnov test and an Anderson-Darling test on planets above and below this mass boundary, and find that they are distinct. This could provide further evidence of two distinct populations possibly having two different formation pathways, with mass as a primary indicator of most likely formation scenario.

4.1 Introduction

Over 4,700 exoplanets are now known, and only about 80 of these objects have atmospheric data from the Hubble Space Telescope (HST), the Spitzer Space Telescope, and/or various ground-based observatories. There are a few main methods to obtaining atmospheric information on these companions such as direct imaging and transit or eclipse technique (Sing et al., 2016; Tsiaras et al., 2018; Pinhas et al., 2019; Mansfield et al., 2021). Direct imaging of exoplanets and substellar companions has revealed a unique population of Jupiter-like objects that have masses $\sim$2–14 M_{Jup}, and are widely separated (5–100 au) from their host stars. Revealing these gas giant companions has inspired a number of novel and complex formation theories such as core/pebble accretion (Johansen & Lambrechts, 2017), dynamical scattering (Rasio & Ford, 1996; Weidenschilling & Marzari, 1996; Chatterjee et al., 2008), disk instability (Kuiper, 1951; Cameron, 1978), and cloud fragmentation (Toomre, 1964) to help determine how these objects formed. These objects still remain a mystery for many of these formation mechanisms, in the case of core/pebble accretion, the distance that these objects orbit is too large to create planets of their masses.

Transiting or eclipsing gas giant planets are often considered "Hot Jupiters" with temperatures around 1000–2500 K. They orbit close to their host stars (1 au), and can have a variety of masses spanning from a percent of a Jupiter mass to 30 Jupiter masses. They are thought to form through a three step process starting from core accretion, to runaway gas accretion to form the atmosphere, and then migration inwards to replicate what we see today (Mizuno et al., 1980; Bodenheimer & Pollack, 1986; Ikoma et al., 2000). The core accretion step is thought to occur in the outskirts of the protoplanetary disk where an abundance of solid material leads to rapid growth of a planetary core before gas dispersal in the disk. With this scenario in mind, the composition of these exoplanets should be sub-stellar in C and O because they would be sequestered in the cores. However, measured bulk metallicities of Jupiter, Saturn, and some exoplanets are shown to be super-stellar, which complicates tracing the formation scenario from

composition of the atmospheres.

Spectral characterization of exoplanets and substellar companions can shed light on how they may have formed. It has been suggested that how a planet formed can be traced by the composition of the planets' atmosphere. For the directly imaged companions, they are young (200 Myr), so it is believed their atmospheres have not undergone immense evolution and could point towards how and where they formed in the protoplanetary disk. For the transit planets, there is a more complicated picture that involves evolution of the atmosphere, accretion of the atmosphere, and migration of the planets inward, but atmospheric composition measurements would still greatly improve our knowledge of their formation. One of these measurements is the C/O ratio. Elemental abundances such as the C/O ratio has been postulated to be fundamental properties of the composition of exoplanet atmospheres and their protoplanetary disks (Madhusudhan, 2019; Cridland et al., 2020). The C/O ratio measurement in particular may be able to trace the formation location of these objects and how they collected gas and solids in their evolving protoplanetary disks (Madhusudhan et al., 2017; Mordasini et al., 2016; Booth et al., 2017; Cridland et al., 2019; Eistrup et al., 2018).

Detailed observations of exoplanets are difficult to obtain because the planets are faint and the stars they orbit are bright. Brown dwarfs tend to be hotter and more luminous than more high contrast exoplanets, therefore they are easier to disentangle from the host star light and they can provide insight into atmospheric properties of gas giant exoplanets. Widely separated brown dwarf companions are also excellent objects to compare to young directly imaged planets because of their similar spectra features and atmospheric parameters. Many brown dwarfs have existing constraints on atmospheric properties such as effective temperature, surface gravity, and molecular composition. HD 284149 b is a substellar companion orbiting at $\sim 3.6''$ from the F8 star HD 284149 A and a stellar companion HD 284149 B discovered by Bonavita et al. (2014, 2017). The HD 284149 ABb system has been proposed to be a part of the Taurus-Ext association (Luhman et al., 2017; Kraus et al., 2017; Daemgen et al., 2015) with an age estimate by Bonavita et al. (2014) of 25^{+25}_{-10} Myr. Bonavita et al. (2017) found an effective temperature of 2395 $\pm$

113 K, a spectral type of M9 $\pm$ 1, and a mass of 26 $\pm$ 3 M_{Jup} for the substellar companion HD 284149 b.

Here, we present $R \sim 4000$ K-band spectra of HD 284149 b using the OSIRIS instrument on the W.M. Keck Telescope and a compilation and statistical analysis of the C/O ratio formation tracer. In Section 4.2 we report our observations and data reduction methods. In Section 4.3 we use atmosphere model grids and forward modeling Markov Chain Monte Carlo methods to determine the best-fit effective temperature, surface gravity, and metallicity of HD 284149 b. We use our best-fit parameters and *PHOENIX* models with scaled C and O abundances to derive a C/O ratio for HD 284149 b. In Section 4.5 we compare C/O ratios of 25 transiting planets from Changeat et al. (2022) to C/O ratios of the directly imaged planets. We find a slight trend between C/O ratio and companion mass and compute two metrics to determine if the planets originate from the same underlying population. In Section 2.5 we discuss the implications of our results and future work.

4.2 Data Reduction

HD 284149 b was observed on 2017 November 3 with the OSIRIS integral field spectrograph (IFS) on the W.M. Keck I telescope (Larkin et al., 2006). We used the K broadband mode (1.965–2.381 μm) with a spatial sampling of 20 milliarcseconds per lenslet. We integrated on the object for 50 minutes via 5 exposures of 10 minutes each, where we dithered up and down by a 2-3 pixels between exposures. Observations of a blank patch of sky and of our A0V telluric standard (HIP 16095) were obtained close in time with the object data. We also obtained dark frames with exposure times matching our dataset. The data were reduced using the OSIRIS data reduction pipeline (DRP; Krabbe et al., 2004; Lockhart et al., 2019). Data cubes (x, y, λ) were generated using the OSIRIS DRP using rectification matrices provided by the observatory for the correct time frame of the observations. At the advice of the DRP working group, we did not use the Clean Cosmic Rays DRP module (T. Do, priv. comm) and we did not use scaled sky

subtraction.

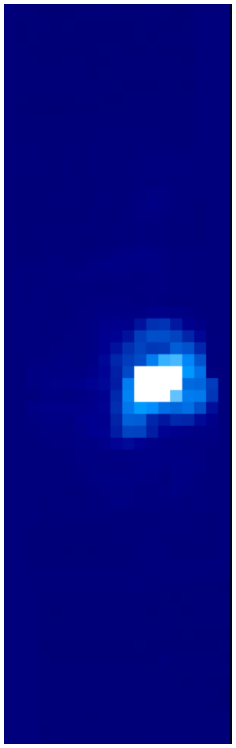

Figure 4.1: An example data cube image frame, collapsed in wavelength via median, from our OSIRIS HD 284149 b dataset. The field of view is 0.32″ x 1.28″. The bright spot shows the companion clearly visible without any need for speckle removal.

Once the one-dimensional spectra for the telluric sources were extracted, we used the DRP to remove hydrogen lines, divide by a blackbody spectrum of the appropriate temperature, and combine all standard star spectra. The individual telluric spectra were median combined and produced a telluric calibrator spectrum. The telluric correction for HD 284149 b was then completed by dividing the final telluric calibrator spectrum from all object frames.

Once the object data cubes are fully reduced, we identify the location of the target. When conducting high contrast observations with OSIRIS, the location of a companion can be challenging to find due to the brightness of the speckles from the host star. For HD 284149 b, the separation from the host star is wide enough and the companion is bright enough that the speckles from the host star do not impact the spectrum of the companion, and identification is straightforward (see Figure 4.1).

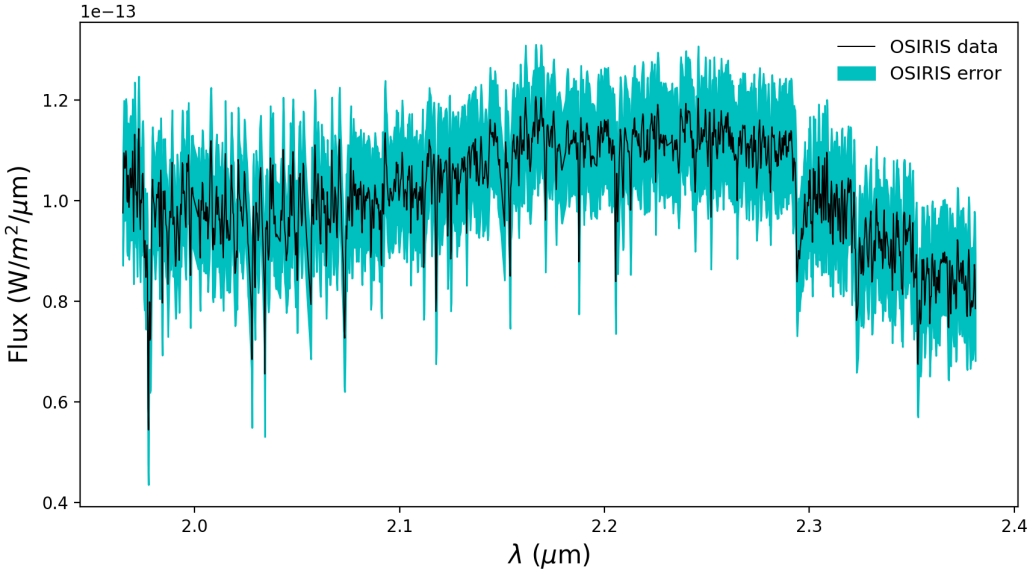

Figure 4.2: Our fully reduced, combined, and flux calibrated, moderate-resolution OSIRIS K-band spectra of HD 284149 b. The errors are calculated from the RMS of the individual spectra at each wavelength. The error includes uncertainties in both the continuum and the lines. The total spectral uncertainties are represented as a shaded blue region. The CO bandhead is distinctly visible at 2.3 μm.

We extract the object spectrum from the data cubes using a box of 3×3 spatial pixels (spaxels). Once we extracted the HD 284149 b spectra from each frame for all data cubes, we then normalize each individual spectrum to account for PSF and background fluctuations. Finally, we median-combine all 5 individual spectra, and do a barycentric correction on the individual spectra. To calibrate the flux of our spectra we calculated the flux at each wavelength such that, when integrated, the flux matches the most recent K-band apparent magnitude (14.332 ± 0.04) from Bonavita et al. (2014).

Uncertainties were calculated by determining the RMS between the individual spectra at each wavelength. These uncertainties include contributions from statistical error in the flux of the planet and the molecular lines. The OH sky lines are subtracted extremely well and have a negligible contribution to the uncertainties. The final combined and flux calibrated spectrum is shown in Figure 4.2.

Narrow spectral features are more easily analyzed by removing the continuum because we can avoid low spatial frequency errors (from residual and/or faint speckles) that affect the continuum shape. We remove the continuum from our fully reduced and flux calibrated spectra using a similar continuum removal process we have used in the past for OSIRIS data (e.g., Barman et al. 2015; Wilcomb et al. 2020; Hoch et al. 2022). To remove the continuum, we employ a high-pass filter with a kernel size of 200 spectral bins to each of the individual spectra. We then subtract the smoothed spectrum without spectral lines from the original spectra. Once all the individual spectra are flattened, we median combine them using the method for the continuum spectra and find the uncertainties by determining the RMS of the individual spectra at each wavelength.

4.3 Spectral Modeling

To determine the effective temperature ($T_{\rm eff}$), surface gravity ($\log g$), and metallicity ([M/H]) of HD 284149 b we used the *PHOENIX* model-based Göttingen spectral library (Husser et al., 2013) that varies these three parameters and covers the range of values expected for HD 284149 b based on previous studies. We chose to use the Göttingen spectral library because they are *PHOENIX* models that cover the estimated temperature and surface gravity of HD 284149 b, therefore there was no need to create additional custom *PHOENIX* models.

Here, we use a forward-modeling process following Blake et al. (2010), Burgasser et al. (2016), Hsu et al. (2021), and Theissen et al. (2022) to determine the best-fit model from the grid. The effective temperature ($T_{\rm eff}$), surface gravity ($\log g$), and metallicity ([M/H]) are inferred using a Markov Chain Monte Carlo (MCMC) method built on the `emcee` package that uses an implementation of the affine-invariant ensemble sampler (Goodman & Weare, 2010; Foreman-Mackey et al., 2013). The assumptions and description of the MCMC calculations are described in Wilcomb et al. (2020).

The results show that HD 284149 b has slightly super-solar metallicity. The best fit

parameters from our continuum K-band OSIRIS data are $T_{\rm eff} = 2469^{+25}_{-26}$ K, $\log g = 4.58^{+0.26}_{-0.31}$, and [M/H] = $0.57^{+0.26}_{-0.24}$. The temperature results are in great agreement with the temperature from Bonavita et al. (2017), which was 2395 $\pm$ 113 K. Figures 4.3-4.4 show the best-fit model for the continuum data and the corresponding corner plot from our MCMC analysis.

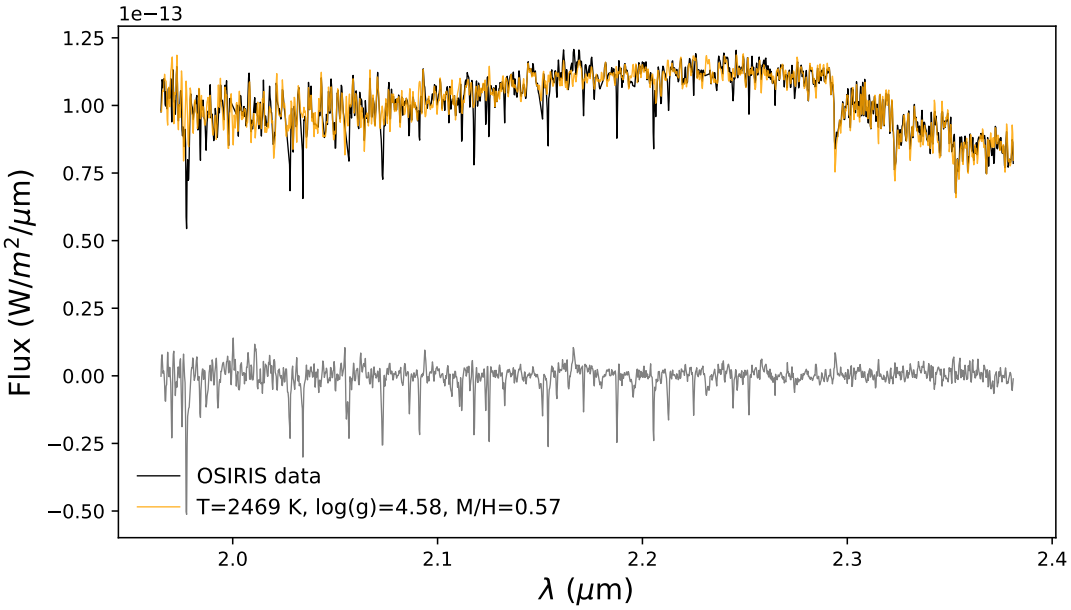

Figure 4.3: Our fully reduced, combined, and flux calibrated moderate-resolution OSIRIS K-band spectra of HD 284149 b in black plotted against the best-fit model in orange. The residuals are plotted below in gray.

We then ran our fitting procedure on the continuum subtracted data using the same grid. We employed the same filtering code used to flatten the data on the model grid to flatten the models. The best fit parameters from our continuum subtracted K-band OSIRIS data are $T_{\rm eff} = 2605^{+19}_{-13}$ K, $\log g = 4.91^{+0.060}_{-0.074}$, and [M/H] = $0.11^{+0.076}_{-0.067}$. Figures 4.5-4.6 show the best-fit model for the continuum subtracted data and the corresponding corner plot from our MCMC analysis. Our continuum subtracted results are similar to our continuum results, but are not within the same error bars. Therefore, we adopt values of $T_{\rm eff} = 2469$ K, with a range of 2443–2624 K, $\log g = 4.58$, with a range of 4.27–4.98, and [M/H] = 0.57, with a range of 0.04–0.83.

4.3.1 C and O Abundances

With best fit values for temperature, surface gravity, and metallicity, we can derive abundances of C and O using our OSIRIS *K*-band spectra. We chose the best-fit values from the continuum fits of the data because the residuals were smaller. We constructed a mini-grid that holds our derived parameters the same, but varies the abundance of C and O. We used the Husser et al. (2013) grid again, and varied C and O abundances. C and O were each varied from 0 to 1000 using a uniform logarithmic sampling, resulting in 12 synthetic spectra. We fit for the abundance of C first, holding O at its initial value. Next, the C abundance was set to its nominal value, and we fit for O.

Figure 4.7 shows the resulting χ^2 distribution as a function of C and O abundance. The models with the lowest χ^2 when compared to the flattened data gave us the best-fits for both C and O. The best fit for C had an abundance scaling of $1.25^{+0.25}_{-0.75}$, and the best fit for O had an abundance scaling of solar or $1.00^{+1.00}_{-0.00}$. To calculate the 1-σ uncertainties in each mole fraction value, we used the values from models within ± 1 of our lowest χ^2.

4.3.2 C/O Ratio for HD 284149b

In our previous work, we have used OSIRIS data to constrain the C/O ratios of directly imaged companions such as HR 8799 b, c, and d, κ Andromedae b and VHS 1256 b (e.g., Konopacky et al. 2013; Wilcomb et al. 2020; Ruffio et al. 2021; Hoch et al. 2022). For giant planets formed by rapid gravitational instabilities, their atmospheres should have elemental abundances that are similar to their host stars (Helled & Schubert, 2009). If giant planets form by a core/pebble accretion process, there could be a range of elemental abundances possible (Öberg et al., 2011; Madhusudhan, 2019). In this framework, the abundances of giant planets' atmospheres formed by core/pebble accretion are highly dependent on the location of formation relative to CO, CO_2, and H_2O frost lines and the amount of solids collected during runaway accretion phase. This can be diagnosed using the C/O ratio.

The C/O ratio is dependent on the abundances of C and O in the atmosphere, the equation used for this derivation is

$$\frac{C}{O} = \frac{10^{\epsilon c - 12}}{10^{\epsilon o - 12}},$$

where ϵ is the scaled abundance relative to Solar. The C/O ratio we derive for HD 284149 b is $0.737^{+0.148}_{-0.442}$. The next step for this object and for the C/O ratio diagnostic is to study the metallicity and C/O ratio of the host star and stellar companion.

4.4 Non-Detections

For our Imaging Spectroscopy Survey of Exoplanetary Atmospheres with Keck/OSIRIS we took data on nine directly imaged planets; κ And b, VHS 1256 b, HR 8799 bcd, HD 284149 b, GJ 504 b, and 51 Eri b. GJ 504 b and 51 Eri b were not detected in our OSIRIS data and details of the observations are in Table 4.4. GJ 504 b is a Jovian planet of $4^{+4.5}_{-1.0}$ M_{Jup} orbiting at a projected separation of 43.5 au around the Sun-like G0-type star, GJ 504 (Kuzuhara et al., 2013). The host star is 1.2 $M_\odot$ and is 160^{+350}_{-60} Myr old. GJ 504 b is significantly cooler than other imaged exoplanets with an effective temperature of about 510^{+30}_{-20} K. GJ 504 b is also the first directly imaged planet around a metal-rich host star. 51 Eri b is a gas giant planet that was discovered orbiting the $\sim$20 Myr 51 Eridani star at 13 au (Macintosh et al., 2015). 51 Eri b is about 600-750 K with a mass of about 2-12 M_{Jup}. Both of these planets are lower temperature and lower mass than the majority of the directly imaged companions, and would be excellent candidates for atmospheric characterization to compare to their hotter counterparts.

For GJ 504 b, we used the OSIRIS integral field spectrograph (IFS) on the W.M. Keck I telescope (Larkin et al., 2006). We conducted observations in the *K* broadband mode (1.965–2.381 μm) with a spatial sampling of $0.050''$ per lenslet for this object with the hope of enhancing its detectability via coarser spatial sampling. We observed a telluric calibrator star (HIP 65599) and obtained sky frames in close time to observations of the object. Data cubes (x, y, λ) were

generated after operating the OSIRIS DRP using the observatory provided rectification matrices for the same time frame of the observations, following the steps described in section 4.2. After reduction and telluric correction, we tried to locate the planet in the data cubes. The separation of GJ 504b means that the speckles were not as bright as some of our other targets, so our attempt to locate the planet was primarily without any speckle removal. We did not see a clear signal when looking at the datacubes. We then tried a cross-correlation approach using a *PHOENIX* model of similar atmospheric parameters (Ruffio et al. (2019)) and still did not see a clear signal in our OSIRIS data.

For 51 Eri b, we conducted observations in the *K* broadband mode (1.965–2.381 μm) with a spatial sampling of $0.020''$ per lenslet, observed a telluric standard star (HIP 25453) and sky frames in close time to object observations. Data cubes were generated using the OSIRIS DRP as with the other sources. We did not see a clear signal in the raw data, and we also tried a cross-correlation approach using a *PHOENIX* model of similar atmospheric parameters and did not detect the planet. Given that the detections of these targets is currently beyond what we can achieve with OSIRIS, both GJ 504 b and 51 Eri b would be great candidates for JWST and upcoming extremely large telescopes (ELTs) that may have better sensitivity to objects of high contrast and/or low temperature.

Table 4.1: Log of two non-detected planets observed for the Imaging Spectroscopy Survey of Exoplanetary Atmospheres with Keck/OSIRIS.

Companion	Band	Spatial Sampling (mas)	Int. Time per Frame (sec)	Total Number of Frames	Total Int. Time (mins)	Dates Taken
51 Eri b	*K*	0.02	600	68	680	Nov 6-8, 2016 & Nov 3-4 2017
GJ 504 b	*K*	0.05	900	18	435	May 14, 2017 & May 26-27, 2019

4.5 C/O Ratio Population Analysis

Direct imaging spectroscopy has allowed for the C/O ratio measurements of many imaged substellar companions. Mollière et al. (2020) derived a C/O ratio of $0.60^{+0.07}_{-0.08}$ for HR 8799 e

through atmospheric retrievals using their code *petitRADTRANS* (Mollière et al., 2019) with the added effect of multiple scattering to better treat cloudy objects. They ran retrievals on *K*-band GRAVITY data (Gravity Collaboration et al., 2017) and archival SPHERE and GPI data. Petrus et al. (2021) calculated an upper limit for the C/O ratio of HIP 65426 b to be $\leq$0.55 using a bayesian inference with BTSETTL with the ForMoSA code on SINFONI medium-resolution *K*-band data (Petrus et al., 2020). A C/O ratio for TYC 8998-760-1 b (YSES-1 b) was derived to be $0.52^{+0.04}_{-0.03}$ by Zhang et al. (2021) using Bayesian retrieval analysis on SINFONI medium-resolution *K*-band data with *petitRADTRANS*. Our group has derived C/O ratios for six directly imaged companions using the OSIRIS IFU. C/O ratios for the other HR 8799 planets, HR 8799 b, c, and d were derived by Ruffio et al. (2021) to be $0.578^{+0.004}_{-0.005}$, 0.562 ± 0.004, and $0.551^{+0.005}_{-0.004}$ respectively. Ruffio et al. (2021) used a custom *PHOENIX* model grid and a forward modeling approach on OSIRIS IFU data to derive these ratios. Wilcomb et al. (2020) derived the C/O ratio for κ And b to be $0.704^{+0.09}_{-0.24}$ following a forward modeling approach on the OSIRIS data using custom *PHOENIX* model grid. We measured VHS 1256 b's C/O ratio as $0.590^{+0.28}_{-0.354}$ in Hoch et al. (2022) following the same approach as Wilcomb et al. (2020) using custom *PHOENIX* models that included a cloud parameter to treat the thick clouds of an "L/T" transition object. In this work, we follow the same procedures from Wilcomb et al. (2020) and Hoch et al. (2022) to calculate a C/O ratio of $0.737^{+0.148}_{-0.442}$ for the substellar companion HD 284149 b using models from Husser et al. (2013).

Transiting exoplanets can occasionally offer low-resolution spectra that can, in turn, allow for the derivation of atmospheric properties such as the C/O ratio. Low-resolution data cannot reveal individual spectral lines, unlike moderate resolution data, so retrievals are often used to derive these properties. Changeat et al. (2022) reanalyzed HST WFC3 G141 Grism data using their open-source pipeline, *Iraclis* (Tsiaras et al., 2016), and Spitzer data of 25 "Hot Jupiters." The free retrieval code used was *Alfnoor* (Changeat et al., 2020), and the equilibrium chemistry retrievals were conducted using the GGChem code (Woitke et al., 2018). Furthermore, Changeat et al. (2022) used the two retrieval methods on HST and Spitzer data and on them individually to

obtain C/O ratio measurements for all 25 exoplanets in their sample.

We compiled and compared various parameters of both the directly imaged and transiting systems such as projected separation (au), companion mass (M_{Jup}), host star mass ($M_{\odot}$), and age (Myr) against C/O ratios of the respective planets. We also compiled the same parameters and C/O ratios of transit planets with retrieval analysis from Changeat et al. (2022). In particular, we chose Changeat et al. (2022) C/O ratio values that were derived through equilibrium chemistry retrieval (eq) on the combination of Spitzer and HST data. If the object did not have a measurement with both, we chose the HST only measurement equilibrium retrieval. We plotted these two populations against one another, shown in figures 4.9-4.12, and saw a trend when plotting companion mass against C/O ratio shown in Figure 4.9. All companions that are about 4 M_{Jup} or above have C/O ratios around 0.7 ± 0.2, and companions with masses less than 4 M_{Jup} exhibit a wider spread of C/O ratios of up to 1.6.

There seemed to be two distinct populations from Figure 4.9, separated by about 3–5 M_{Jup}. To verify this distinction, we performed a few statistical tests. We decided to conduct the Kolmogorov–Smirnov Test (KS Test), and the Anderson-Darling Test (AD Test) because they are well-established tests of similarity to see if two distributions come from the same parent distribution. We first randomly sampled 100,000 values from each parameter (C/O ratio and companion mass) using a Gaussian distribution centered on the central value with a width defined by the uncertainty. We chose 4 M_{Jup} as the distinguishing mass, the central value between 3 and 5 M_{Jup}. We then split the sample into two components, those with mass below 4 M_{Jup} and the other equal to or greater 4 M_{Jup}. The two subsamples, with random C/O ratio values and corresponding random masses were then put through the KS Test using the scipy.stats.ks_2samp python code and the AD Test using the scipy.stats.anderson_ksamp python code. This generated 100,000 p values and significance values from each test. We show the resulting distributions in Figure 4.13. The results show that both p values and significance values are less than 1%, indicating that the two populations were distinct and statistically unlikely drawn from the same underlying population.

4.6 Discussion and Conclusions

Direct imaging and moderate resolution spectroscopy have greatly expanded our knowledge of young, intricate, gas giant atmospheres. HD 284149 b is an interesting case for detailed atmospheric characterization because of it's wide separation, youth, and brightness. Objects that are easier to observe can provide insights into higher contrast systems that make it difficult to obtain moderate resolution spectra. Our results of $T_{\rm eff}$ = 2469 K, with a range of 2443–2624 K, $\log g$ = 4.58, with a range of 4.27–4.98, and [M/H] = 0.57, with a range of 0.04–0.83 agree with the results from Bonavita et al. (2014, 2017) that posit HD 284149 b is likely a brown dwarf mass object, in a youthful system. We compared our results to Baraffe et al. (2015) evolutionary models assuming an age of 25 Myr and found a corresponding mass range of 27–38 $M_{\rm Jup}$, which is fully consistent with 26 ± 3 $M_{\rm Jup}$ from Bonavita et al. (2017)

Formation of objects in the gas giant planet mass and low mass brown dwarf regime is of considerable interest because formation models have trouble producing these types of objects. Formation diagnostics such as C/O ratio can provide context as to where and potentially how these substellar objects have formed. HD 284149 b shares properties with imaged objects like AB Pic b (Chauvin et al., 2005) and ROXs 42Bb (Kraus et al., 2014), which place HD 284149 b between the planetary mass object regime and the lowest mass brown dwarfs imaged to date. HD 284149 b represents a challenge in our understanding of formation of low-mass companions at extremely wide separations. The high mass ratio of this system might point towards a planet-like formation scenario such as core/pebble accretion, but its estimated mass is above the deuterium burning limit, which could suggest a star-like rapid formation process such as gravitational instability. Measuring the C/O ratio of HD 284149 b provides one possible diagnostic for figuring out how this object formed. The C/O ratio is slightly elevated but the errors do still include Solar, just like κ And b. This result points to a very rapid formation process, potentially through either gravitational instability or common gravitational collapse similar to a binary star system. However, this diagnostic involves a comparison to the host star in order to

draw definitive conclusions about formation. We do not have a C/O ratio of the host star because the data available were low resolution. The slightly elevated metallicity could shed some light on formation, but host star metallicity is still required. Until atmospheric characterization is conducted on HD 284149 A, we can only conclude that the evidence points to roughly similar values for the host star and the companion if the star has similar abundances to Solar.

HD 284149 b now represents a ninth directly imaged substellar companion, in addition to the four HR 8799 planets (Konopacky et al., 2013; Barman et al., 2015; Mollière et al., 2020; Ruffio et al., 2021), κ And b (Wilcomb et al., 2020), VHS 1256 b (Hoch et al., 2022), HIP 65426 b (Petrus et al., 2021), and TYC 8998-760-1 b (YSES-1 b Zhang et al. 2021), with an approximately Solar C/O ratio and diagnostic that did not reveal formation via core/pebble accretion. The scenario certainly cannot be ruled out given the uncertainties in the data and the range of possible C/O ratios predicted by models (e.g., Madhusudhan 2019).

All of the directly imaged planets with C/O ratios have estimated masses of >4 M_{Jup}. Santos et al. (2017) postulated that there may be two distinct populations of exoplanets that split at 4 M_{Jup} when comparing stellar metallicity [Fe/H] to companion mass M_{Jup}. When we looked at C/O ratio versus a range of other parameters, the only one that showed a potential pattern or correlation was mass. Interestingly, the split is around 4 M_{Jup}, exactly the same as in Santos et al. (2017). The results of our KS test and AD test show that these populations are distinct populations and could possibly point to two different formation mechanisms. There are a few directly imaged planets with estimated masses below 4 M_{Jup} (e.g., 51 Eri, Macintosh et al. (2015)), but they have not yet had their C/O ratios measured. Such measurements, which should be possible with the newer generation of instruments such as KPIC on Keck Delorme et al. (2021), may reveal whether the trend with mass holds.

Our sample of directly imaged planets and Changeat et al. (2022)'s sample of transiting planets show a possible trend between C/O ratio and companion mass that could probe if there are indeed two distinct populations of exoplanets. However, there are some outliers in our samples and in particular there is a large spread in C/O with the planets under 4 M_{Jup}. This

spread could have a physical meaning, or it could mean better constraints on C/O ratios are needed. Indeed, the large spread in C/O ratio demonstrated in Changeat et al. (2022) based on the dataset used for retrieval highlights the potential for systematic errors using currently available transit spectroscopy. *JWST*, and future facilities such as *ARIEL* and Extremely Large Telescopes (ELTs) will obtain tighter constraints on atmospheric species that trace the C/O value and narrow this spread.

There are other mechanisms that can impact the C/O ratio that should be studied before connecting composition to formation of directly imaged planets. Migration has been postulated as a mechanism for the final location of planets paired with core/pebble accretion, but taking into account chemical evolution of the protoplanetary disk could show that less migration is needed to explain the chemical properties of the atmospheres (Mollière et al., 2022). When considering pebble accretion, the drift, evaporation, and accretion of pebbles is able to reproduce planetary C/O values, but it is uncertain whether it can reproduce high atmospheric metallicities that have been seen in some directly imaged planets such as HR 8799 e (Mollière et al., 2022). Therefore, it is important to have an understanding of the chemical composition and evolution of the protoplanetary disk to understand the composition of the disk gas and solids that ultimately build the planets. Measuring the C/O ratio of planets is still important, but tracing a formation pathway with these measurements require better constraints on elemental abundances and more detailed evolutionary models of the disk composition.

Population studies of exoplanets and their formation pathways still remain difficult due to detection biases from each of the discovery methods and the need for a more detailed understanding of chemical and physical evolution of the protoplanetary disks. C/O ratio measurements are also very difficult to measure and constrain using ground-based observatories. However, the Imaging Spectroscopy Survey of Exoplanetary Atmospheres with Keck/OSIRIS has provided six out of the nine measured C/O ratios for directly imaged companions. The work presented here will pave the way for future studies based on the next generation of space telescopes, high resolution spectrographs, and ELTs.

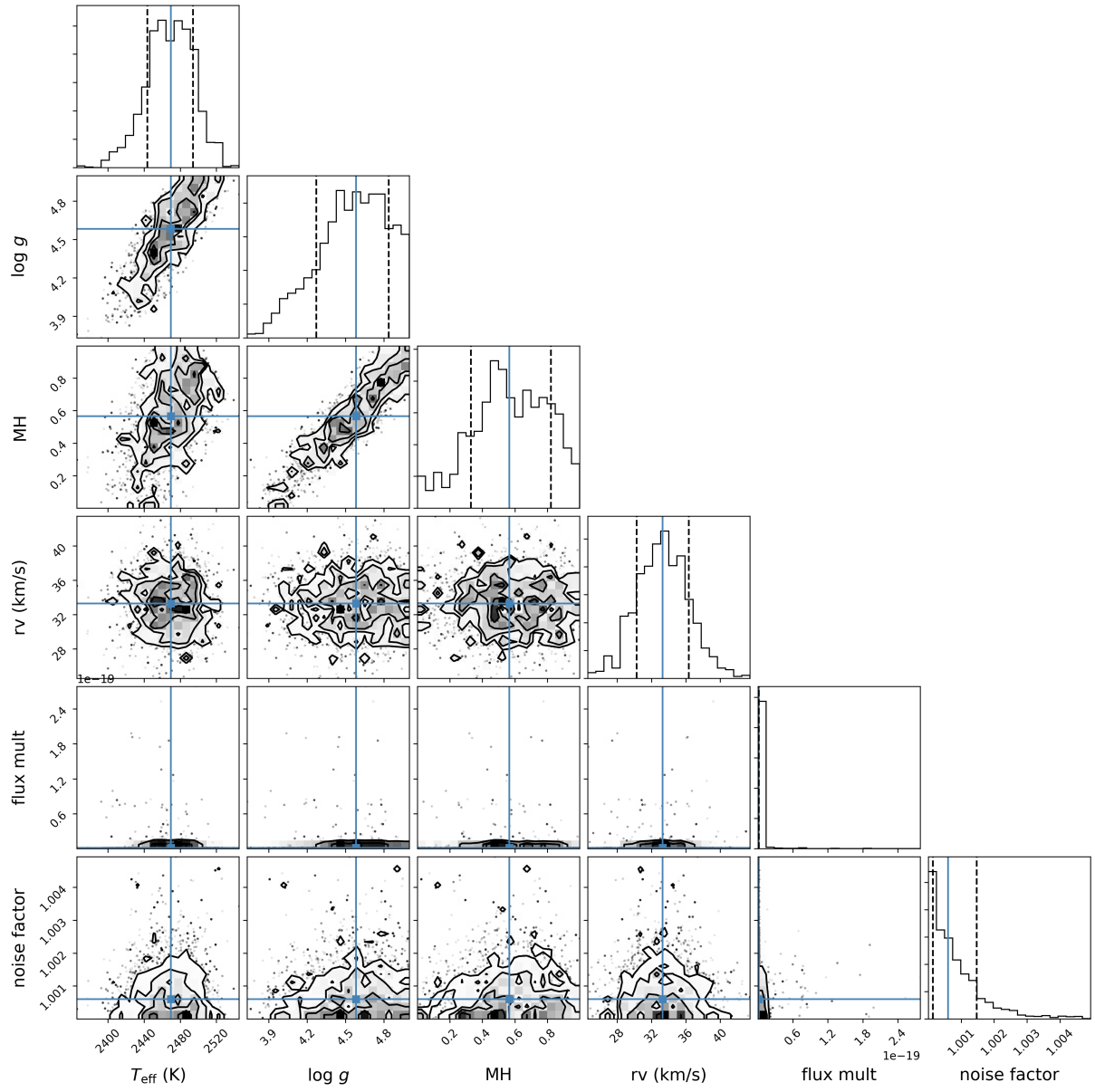

Figure 4.4: Corner plot from our MCMC fits for our continuum OSIRIS K-band spectra. The diagonal shows the marginalized posteriors. The covariances between all the parameters are in the corresponding 2-d histograms. The blue lines represent the 50 percentile, and the dotted lines represent the 16 and 84 percentiles. The "flux mult" corresponds to the dilution factor that scales the model by $(radius)^2(distance)^{-2}$.

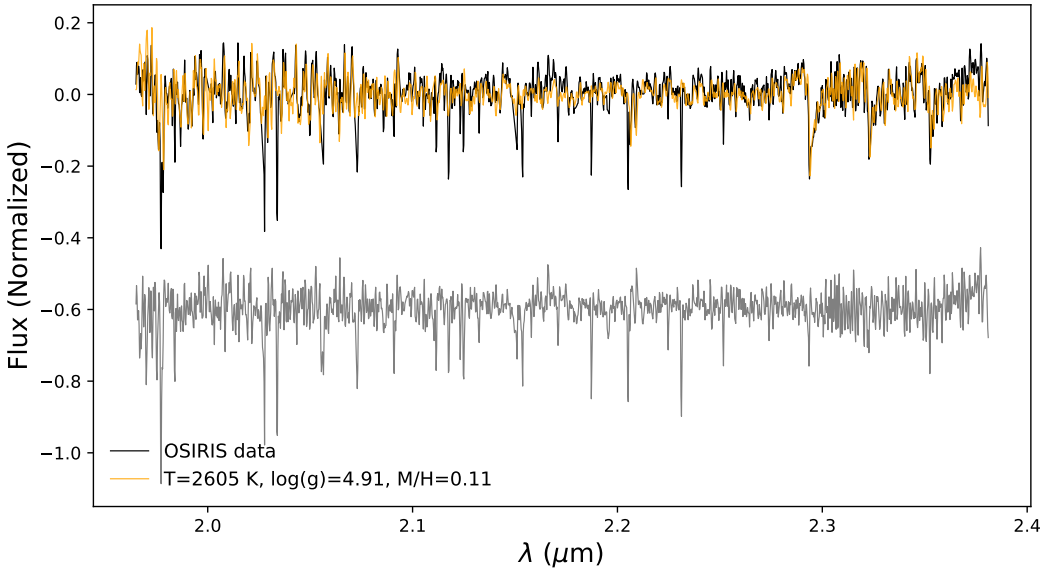

Figure 4.5: Our fully reduced, combined, and continuum subtracted moderate resolution OSIRIS K-band spectra of HD 284149 b in black plotted against the best-fit model in orange. The residuals are plotted below in gray.

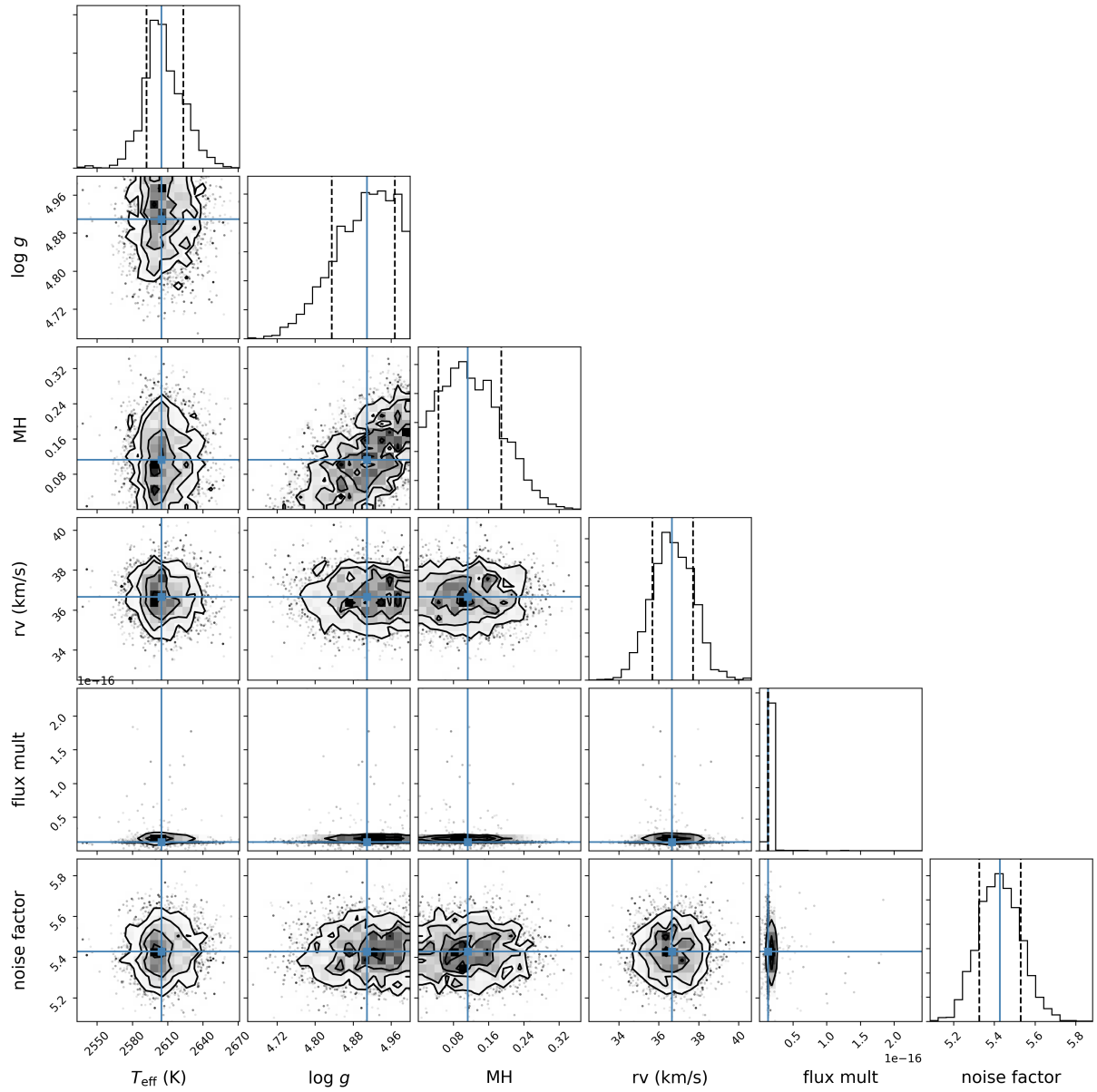

Figure 4.6: Corner plot from our MCMC fits for our continuum subtracted OSIRIS *K*-band spectra.

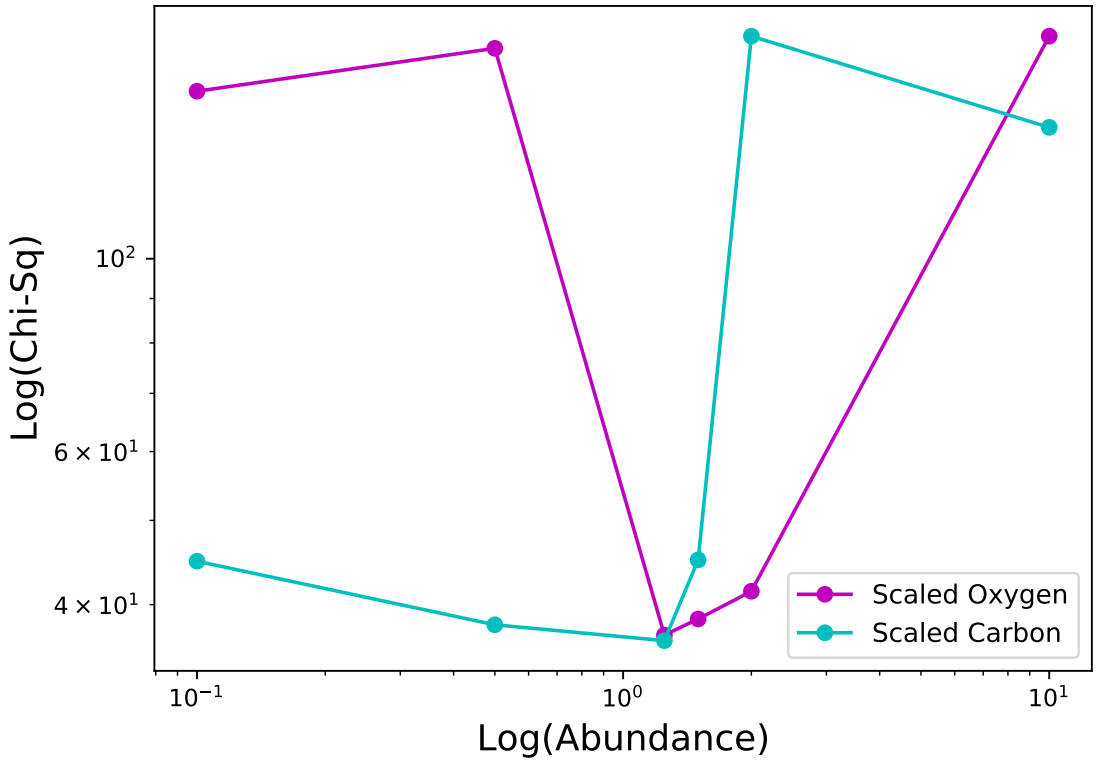

Figure 4.7: Results of $T_{\rm eff} = 2469^{+25}_{-26}$ K, $\log g = 4.58^{+0.26}_{-0.31}$, and [M/H] $= 0.57^{+0.26}_{-0.24}$ model fits with varying abundances for both C and O to our continuum-subtracted OSIRIS spectrum. The abundances are given in units relative to the ratio in the Sun, such that a value of zero implies the solar value. The scalings of C prefer super-solar/solar and the scalings of O prefer solar values. From these fits we find C/O $= 0.737^{+0.148}_{-0.442}$.

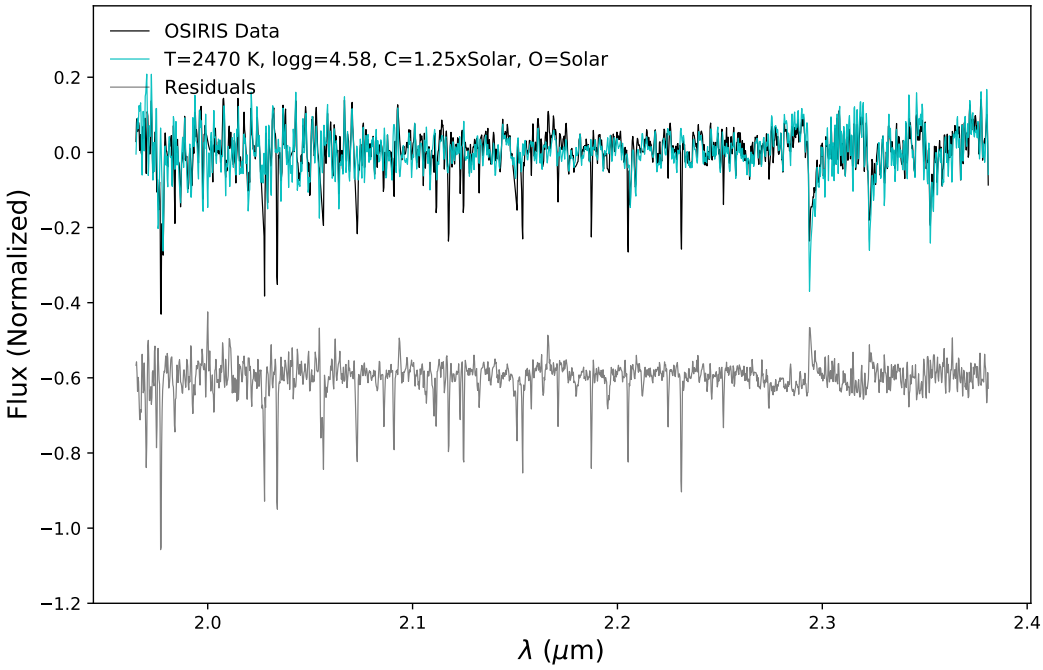

Figure 4.8: The best-fit model from the χ^2 results with a C of 1.25$\times$Solar and a O of Solar. The model is plotted in blue, the data are in black, and the residuals are shown below in gray.

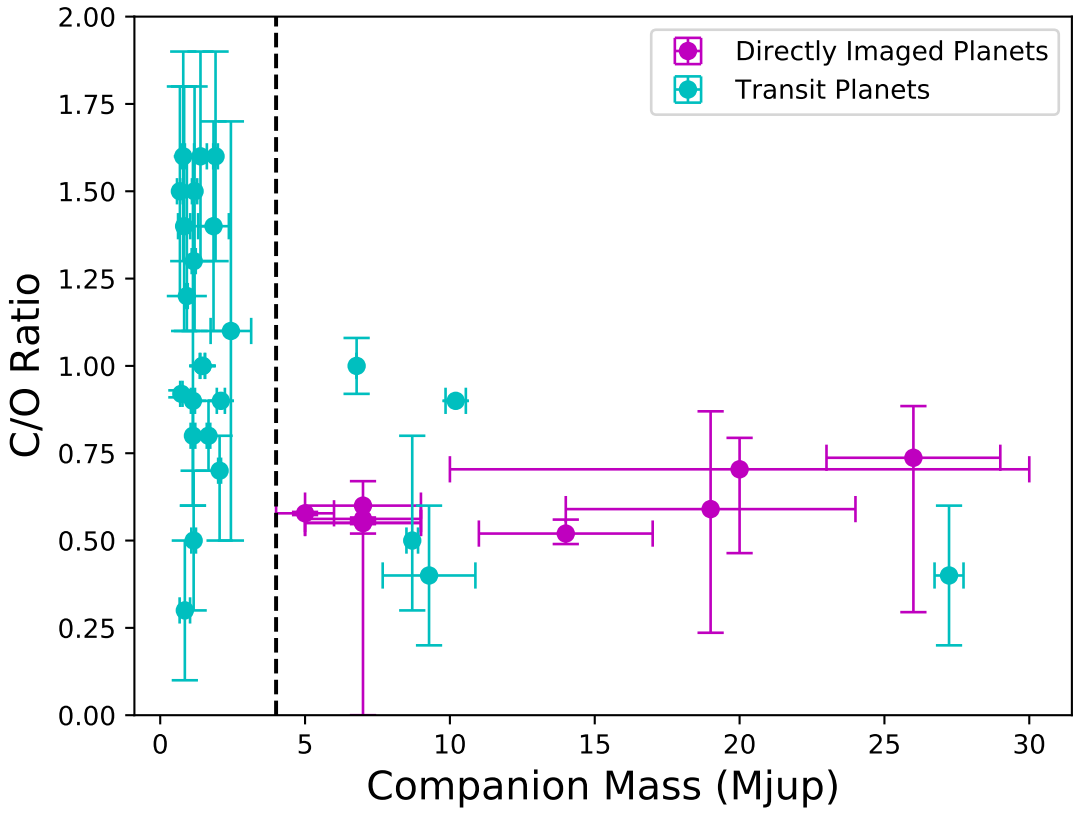

Figure 4.9: Population of 25 retrieval exoplanets in blue and 9 directly imaged planets in magenta. Here are their C/O ratios plotted against the companion masses in M_{Jup}. There appear to be two groupings of planets, one with masses below 4 M_{Jup} and one with masses greater than or equal to 4 M_{Jup}, which is shown by the vertical dashed black line. We ran two tests, a KS Test and an AD Test on 100,000 randomly sampled C/O ratios and companion masses within the error bars of the objects plotted. The two tests came back with p values and significance values less than 1% indicating these two populations are distinct.

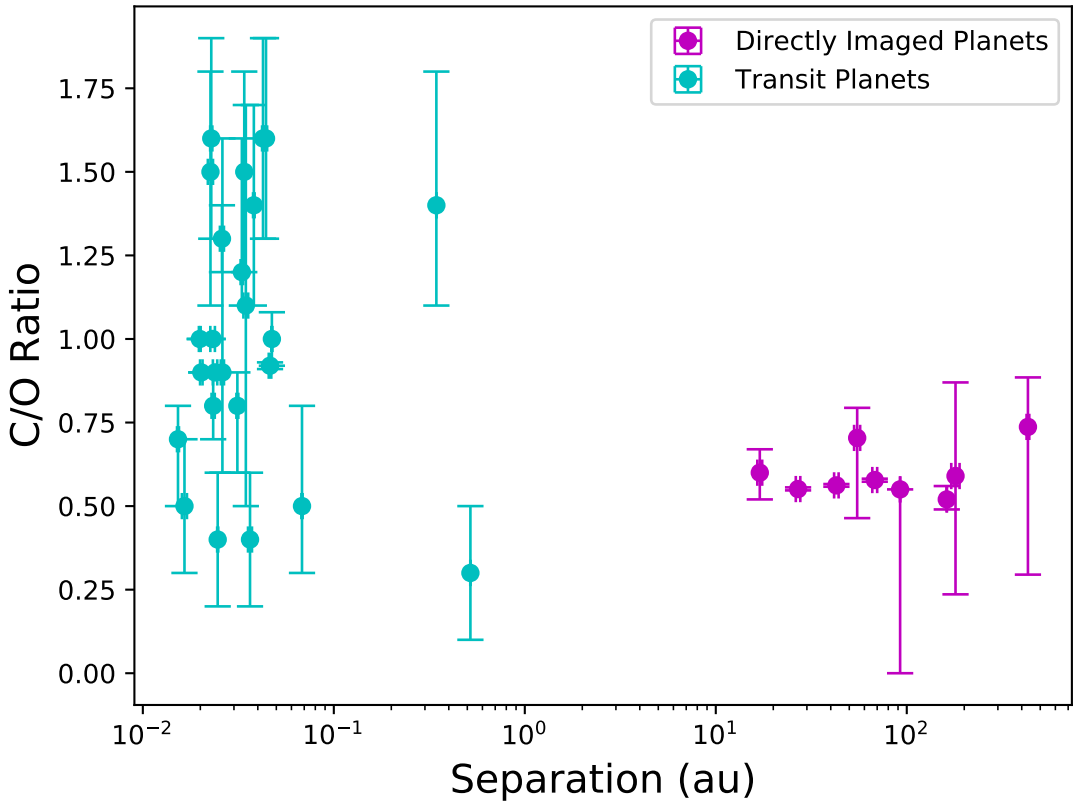

Figure 4.10: Population of 25 retrieval exoplanets in blue and 9 directly imaged planets in magenta. Here are their C/O ratios plotted against their projected separation in au from their host star/system. This plot most likely illustrates the detection bias in separation between the two populations.

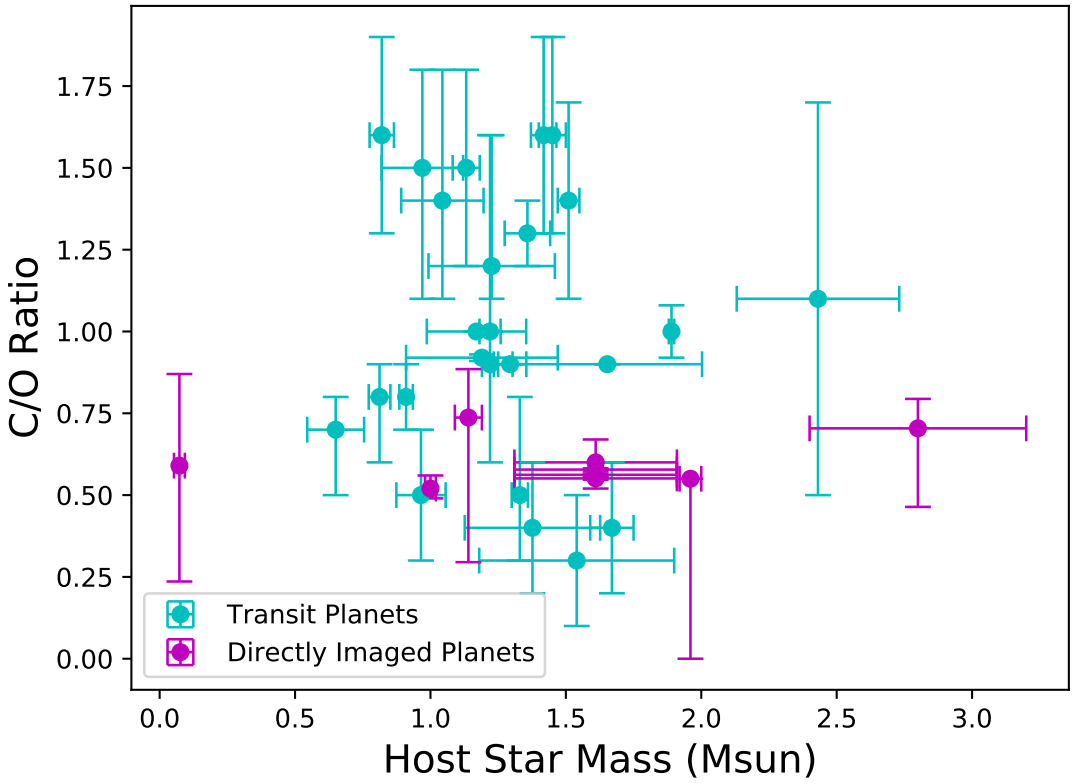

Figure 4.11: Population of 25 retrieval exoplanets in blue and 9 directly imaged planets in magenta. Here are their C/O ratios plotted against the host star masses in $M_{\odot}$. There seems to be no visible correlation between these parameters.

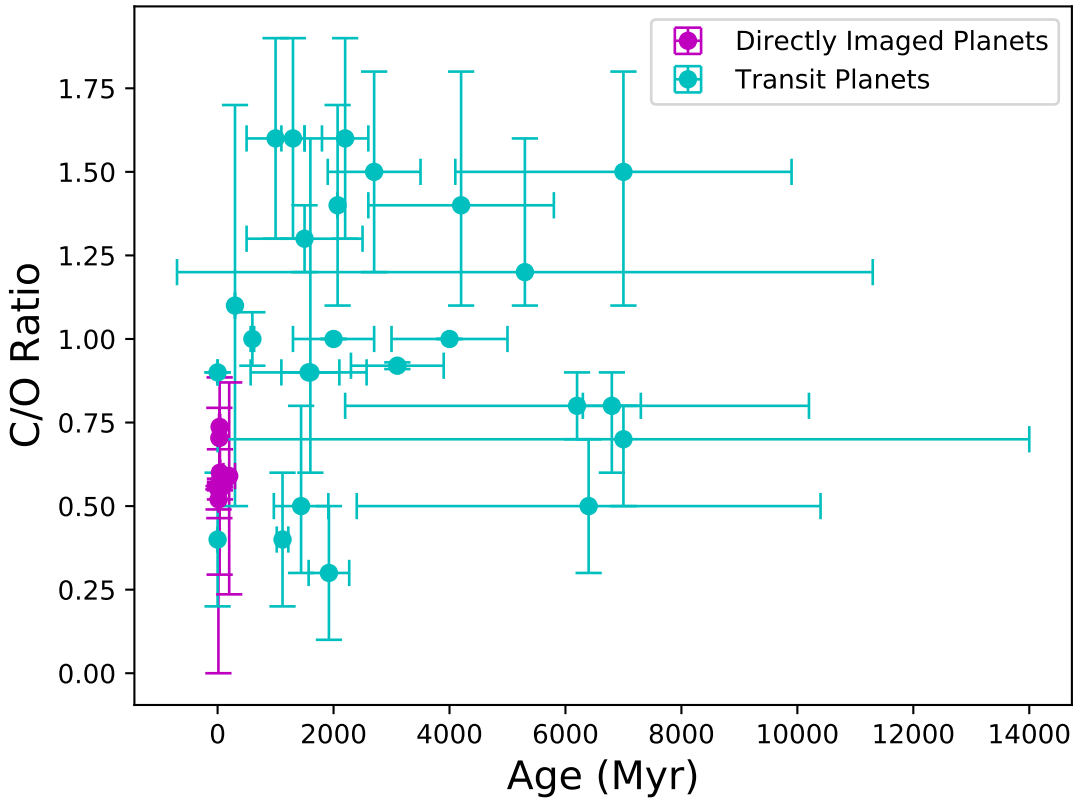

Figure 4.12: Population of 25 retrieval exoplanets in blue and 9 directly imaged planets in magenta. Here are their C/O ratios plotted against the system age in Myr. This most likely illustrates the differences in the two populations, with the directly imaged planets being younger because they are more luminous and more easily detectable with direct imaging.

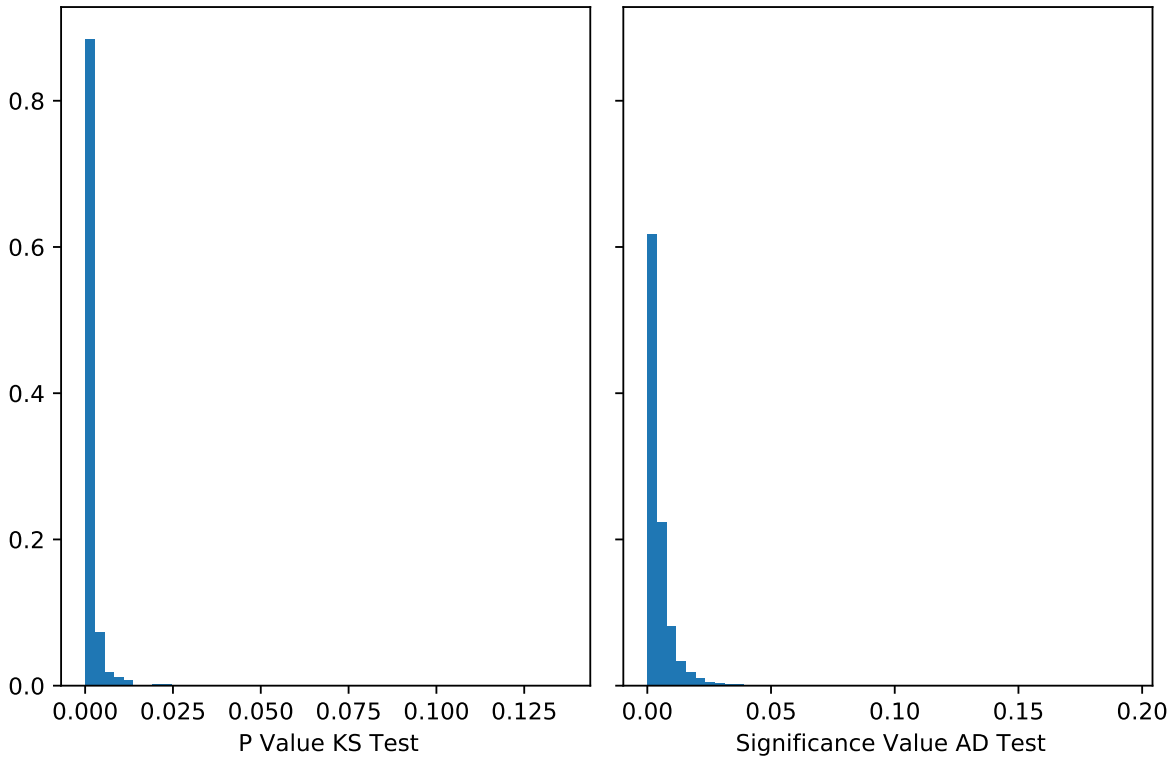

Figure 4.13: A histogram of p values from the KS Test and significance values from the AD Test. The results seem to show that both p values and significance values are less than 1% indicating that the two populations were distinct and not from the same underlying population.

Chapter 5

Summary and Future Work

5.1 Summary of Results and Conclusions

Moderate resolution spectroscopy of directly imaged planets using OSIRIS has greatly improved our knowledge of their intricate atmospheres. The OSIRIS IFU on the W. M. Keck Telescope was used to obtain moderate resolution K-band spectroscopy of three new directly imaged companions; κ And b, discussed in Chapter 2, VHS 1256 b, discussed in Chapter 3, and HD 284149 b, discussed in Chapter 4. This new data increased the number of C/O ratios for directly imaged planets by 50%, allowing us to perform a new statistical analysis on C/O ratios of directly imaged planets and transit/eclipse planets. The main conclusions are discussed here:

1. For κ And b, we used our forward modeling procedure and derived atmospheric parameters for effective temperature, $T_{\rm eff}$ = 2050 K, with a range of 1950–2150 K, surface gravity, $\log g$ = 3.8, with a range of 3.5–4.5, and metallicity, [M/H] = −0.1, with a range of -0.2–0.0.

2. Most studies of the κ And system have led to the conclusion that it is young, as originally predicted by Carson et al. (2013). Our derivation of low surface gravity ($\log g$ <4.5) using our OSIRIS spectrum is another piece of evidence in favor of a young age.

3. The C/O ratio we derive for κ And b is $0.70^{+0.09}_{-0.24}$. Although our current uncertainties allow for slightly elevated C/O ratios, the most likely scenario is that the C/O ratio is roughly consistent with the Sun.

4. We obtained a slightly subsolar best-fit metallicity for κ And b, and this may suggest that the host star is metal poor overall. A number of theoretical works have suggested that formation via gravitational instability would preferentially occur around low metallicity stars.

5. For VHS 1256 b, we derive an effective temperature of 1240 K, with a range of 1200–1300 K, a surface gravity of $\log g = 3.25$, with a range of 3.25–3.75 and a cloud parameter of $\log P_{cloud} = 6$, with a range of 6.0–6.6. These values are consistent with previous studies, regardless of the new, larger system distance from GAIA EDR3 ($22.2^{+1.1}_{-1.2}$ pc).

6. We conclude that VHS 1256 b has deep clouds with a large mean grain size of 3 μm that is consistent with being near or just beyond the L/T transition, as indicated by its L7 spectral type.

7. We derive a C/O ratio of $0.590^{+0.280}_{-0.354}$ for VHS 1256b. It is likely that VHS 1256 b formed like a binary star rather than a planet.

8. For HD 284149 b, we derive an effective temperature of $T_{\rm eff} = 2469$ K, with a range of 2443–2624 K, a surface gravity of $\log g = 4.58$, with a range of 4.27–4.98, and a metallicity [M/H] = 0.57, with a range of 0.04–0.83.

9. The C/O ratio for HD 284149 b was $0.737^{+0.148}_{-0.442}$. There is no known C/O ratio for the host star, so a full formation diagnostic was not achieved. However, the C/O ratio is elevated but the errors do still include Solar, similar to κ And b.

10. All directly imaged planets with measured C/O ratios are consistent with solar, which could either mean the diagnostic is not as helpful as we previously thought, that all formed via gravitational instability, or that further theoretical work is needed to interpret the results. Many studies have shown that the C/O ratio could be impacted by grain size (Piso et al., 2015), migration of grains or pebbles (Booth et al., 2017), migration of planets themselves

(Cridland et al., 2020), and whether the accreted material is from the midplane (Morbidelli et al. 2014; Batygin 2018).

11. Some transiting planets have retrieval derived C/O ratios that vary well beyond the Solar value. We conducted a statistical analysis of 25 transit planets and 9 directly imaged planets across various parameters such as companion mass (M_{Jup}), host star mass ($M_{\odot}$), and projected separation (au) against their C/O ratios. We found a possible trend with companion mass versus C/O ratio seeing two distinct groups; planets less than $4M_{Jup}$ and planets with masses equal to or greater than M_{Jup}. We conducted a KS test and an AD test and the results show that the two groups are indeed distinct from one another. This is an interesting result because other works have also shown that there may be two distinct populations of exoplanets separated around $4M_{Jup}$, which could suggest a formation mechanism difference near this boundary.

5.2 Future Work

The future of direct characterization of exoplanets lies in increasing the wavelength coverage of moderate resolution spectra, but to increase the coverage to long wavelengths we need to utilize a space-based observatory. Many exoplanets, and exoplanet analogues will be imaged with the James Webb Space Telescope (JWST). Our team has guaranteed time observations (GTO) of HR 19647 with JWST's NIRSpec IFU. While not considered a directly imaged exoplanet, this "benchmark brown dwarf" IFU data will be an important step to test the algorithms prepared for high contrast imaging and provide a direct comparison for the incoming exoplanet data. Additionally, one of the Early Release Science programs (ERS) will use the NIRSpec IFU to image VHS 1256 b, a companion that was analyzed using OSIRIS in this thesis. We will analyze and characterize this object again using algorithms adapted for NIRSpec from the OSIRIS survey and combine the datasets for a complete atmospheric characterization.

Furthermore, our team led a successful proposal in the very competitive Cycle 1 to

conduct a comprehensive spectroscopic characterization of the young, directly imaged multi-planet system TYC 8998-760-1 (YSES-1). We will target these two recently-discovered Jovian exoplanets to obtain (1) complete low-resolution spectra spanning 1–12 μm, for highly precise measurement of fundamental planetary properties through atmospheric retrievals, and (2) moderate-resolution (R$\sim$2700) spectra across 3–5 μm to measure elemental abundances and cloud properties as tracers of planet formation processes. The brightness and wide separation (1.7$''$ and 3.4$''$) of these planets make this system an extraordinary target for JWST as shown in Figure 5.1. These observations will enable detailed comparative planetology by assessing the atmospheres and formation pathways of these worlds against one another, other directly imaged planets, and young field brown dwarfs.

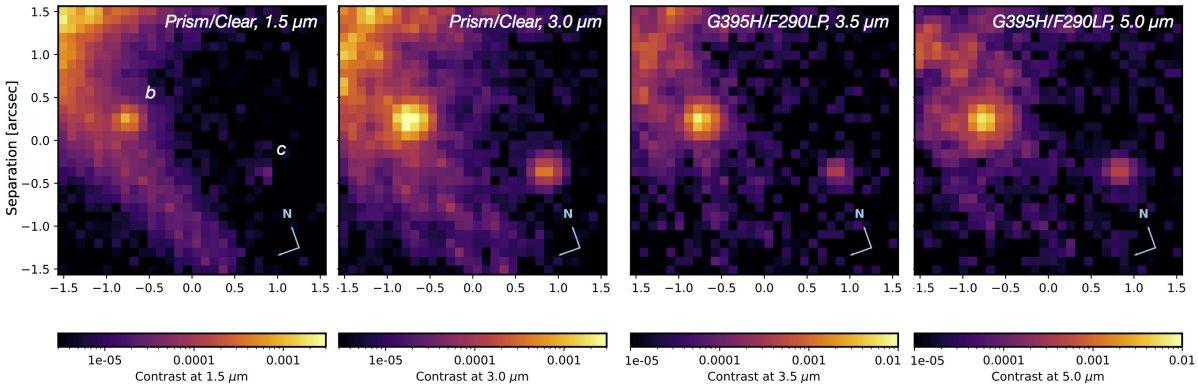

Figure 5.1: Simulated data cube slices for our planned NIRSpec IFU pointing. Both companions are obvious at all wavelengths even before PSF subtraction. This hybrid simulation was generated by combining ETC simulated cubes containing the planets plus a diffractive model for light from the star entering the IFU aperture.

TYC 8998-760-1 (hereafter TYC 8998) is one of the newest multiplanet directly imaged system. Two widely-separated planets orbit a solar-mass star at 160 and 320 au (Bohn et al., 2020a,b). Multiplanet systems offer a key laboratory for exoplanet studies, as common age and formation environment eliminates uncertainties that can plague comparisons between objects in different systems. The inner and more massive TYC 8998 b has an estimated effective temperature of $\sim$1700 K, while TYC 8998 c has an effective temperature of $\sim$1200 K. Their inferred masses are 16 M_{Jup} and 12 M_{Jup}, respectively, therefore likely spanning the deuterium

burning limit and the canonical “L/T" transition in substellar objects, key boundaries in terms of classification and atmospheric characterization.

Data that span the full near- to mid-infrared are highly advantageous, allowing for accurate measurements of effective temperature, bolometric luminosity, radius, surface gravity, and cloud properties. OSIRIS, and other ground based instruments cannot provide full wavelength coverage, especially not beyond 3 μm, where water vapor in the Earth's atmosphere dominates the opacity.

5.2.1 Low-resolution, full infrared spectra

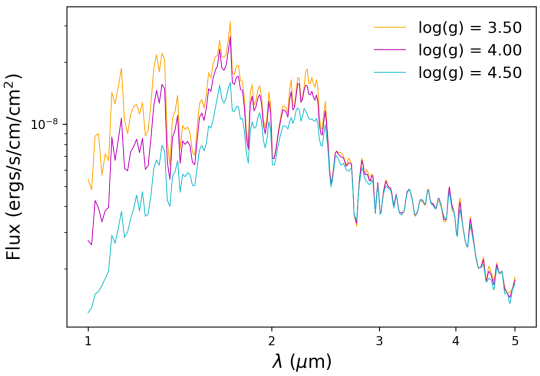

Figure 5.2: Simulated PHOENIX model spectra for TYC 8998 b at three different surface gravities.

NIRSpec prism's wavelength range from 1–2.5 μm is highly gravity sensitive (Fig 5.2). This stems from alkali lines that have formed the basis of the gravity classification scheme often used for brown dwarfs of similar temperatures (Allers & Liu, 2013). From low-resolution spectra with SNR $>$ 50, we will be able to constrain surface gravity within $<$ 0.1 dex. At the same time, we will constrain metallicity because of the alkali sensitivity, which cannot be done precisely with existing photometry.

Longer wavelengths provide an exciting opportunity to explore cloud properties. Clouds are a nearly ubiquitous feature of substellar and planetary-mass objects, but have remained difficult to model. The presence of clouds is both a function of temperature and surface gravity,

this is why objects such as TYC 8998 c can have temperatures consistent with T dwarfs but spectra clearly impacted by clouds. Data between 5–12 μm will be sensitive to a variety of cloud features that are not reachable with ground-based NIR bands. Various absorption features from species such as enstatite, forsterite, and corundum are visible at 9–11 μm, with the strength of these features dependent on the structure of the grains (Luna & Morley, 2019). The obtained low-resolution MIRI spectra will easily distinguish between the presence or absence of such cloud types, with high sensitivity to grain composition and cloud optical depth.

For the low-resolution data, retrievals will be used to derive the properties of these planets. Retrievals are an effective way to infer atmospheric composition, providing robust estimates of temperature, luminosity, gravity, cloud properties, and abundances (Burningham et al., 2017; Line et al., 2017; Gonzales et al., 2020)).

5.2.2 Moderate-Resolution, NIR spectra

Even the newest models of pebble accretion that incorporate the impact of migration have difficulty explaining wide orbit multiplanet systems such as HR 8799 (Johansen & Lambrechts, 2017). For TYC, 8998, now the widest known multiplanetary system, there is potential to distinguish between formation mechanisms such as core accretion and gravitational instability via constraints from metallicity and abundance ratios. Similar to the OSIRIS directly imaged planets, we will measure the C/O ratio of the TYC 8998 planets. Although this formation diagnostic is proving to be less reliable than previously thought, obtaining these measurements will help characterize the directly imaged planet population. Preliminary estimates from the VLT/X-Shooter spectra show that the TYC 8998 star has solar metallicity (V. Dorazi, priv. comm.). Planned observations with HARPS will determine the stellar C/O. The next step is to measure the planetary abundances for comparison. This can be done in a similar manner to the OSIRIS data, but with SINFONI and only for spectroscopy of TYC 8998 b. TYC 8998 c is dim enough to be a difficult target for even 8-m telescopes.

We will also target a new formation diagnostic, the ^{12}CO/^{13}CO isotope ratio from Zhang

et al. 2021. They measured the first $^{12}CO/^{13}CO$ isotope ratio in an exoplanet atmosphere (TYC 8998 b). This ratio varies as a function of separation to the host star within the protoplanetary disk. Previous work has shown that TYC 8998 b is enriched in ^{13}CO compared to terrestrial and galactic standards, which suggests formation beyond the CO ice line at ∼20 au. This information is critical to inform formation models and narrow down formation pathways for widely separated giant planets.

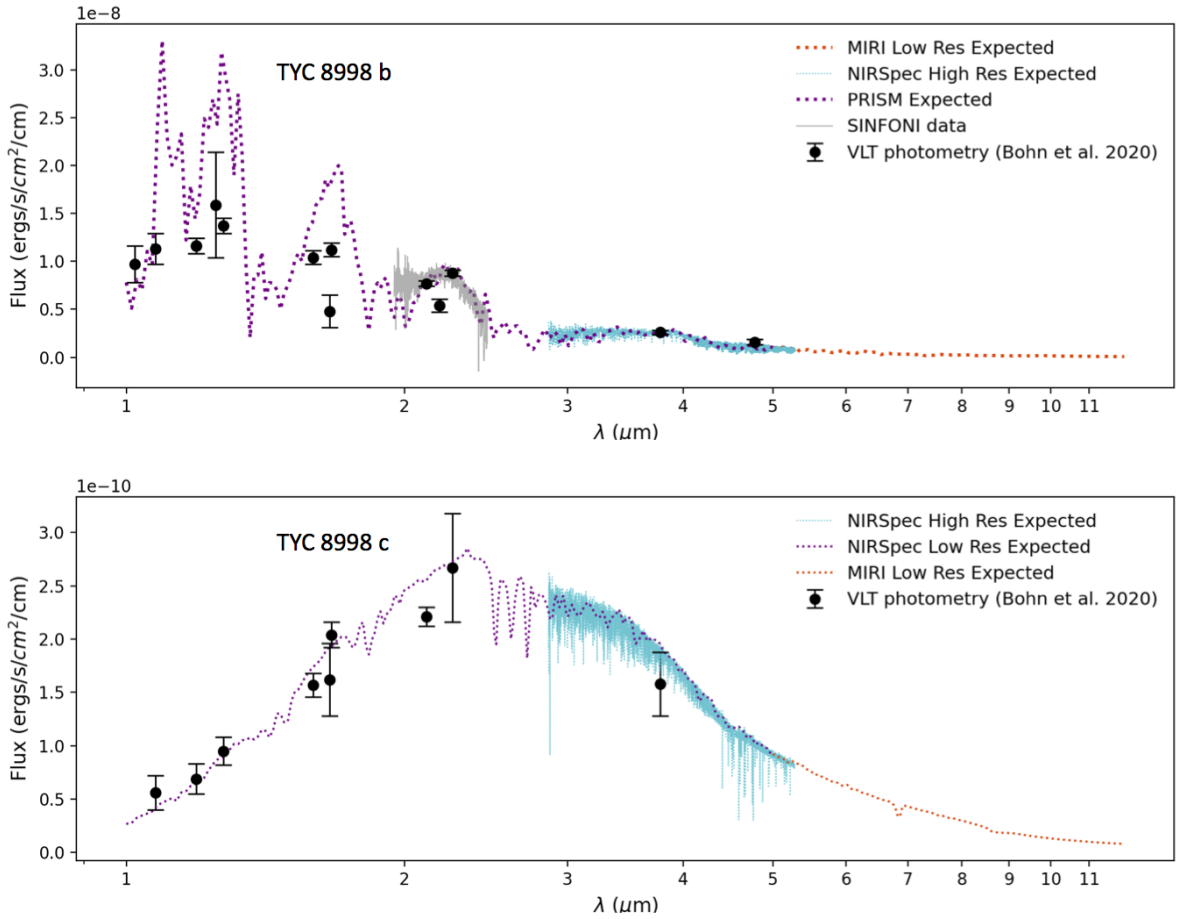

Figure 5.3: Current and proposed data for TYC8998 b and c, including photometry (black points, Bohn et al., 2020b,a), and a recent R∼ 5000 spectrum in K-band from SINFONI for TYC8998 b. Simulated examples of the data expected are shown with dotted lines, demonstrating the massive increase in spectral information enabled by JWST. The model shown for TYC 8998 c, the best fit BT-Settl model from Bohn et al. 2020b, is unusual compared to typical L/T atmospheres, potentially due to thick clouds.

Longer wavelengths accessible only from space are a critical regime for confirming

non-equilibrium chemistry between CO and CH_4, which is otherwise degenerate with parameters such as the C/O ratio as assessed by CO lines in the K-band. For example, the relative strengths of the CO features at 2.29 μm are impacted by the overall abundance of carbon and the amount of it that may be locked in CH_4, which is difficult to measure in the K-band (Barman et al., 2015). On the other hand, the Q-branch bandhead of CH_4 peaks in opacity at 3.3 μm (Noll et al., 2000; Cushing et al., 2005; Kirkpatrick, 2005), therefore this region is an extremely sensitive measure of non-equilibrium chemistry (Miles et al., 2020). Theoretical work demonstrates that vertical mixing (parameterized by Kzz) can displace methane from the photosphere with warmer, CO-dominated gas (Hubeny & Burrows, 2007; Zahnle & Marley, 2014). Once we constrain Kzz at 3.3 μm, we will obtain accurate estimates of C/O using the strength of individual molecular lines and a forward modeling approach to fit for atmospheric parameters (e.g., Ruffio et al. 2019). Figure 5 shows the immense amount of spectral data that will be obtained on the TYC 8998 system. The combination of low and moderate resolution data is powerful, as results from retrievals and forward modeling can be compared for verifying abundances found in retrievals.

5.2.3 Continuation of the Imaging Spectroscopy Survey of Exoplanetary Atmospheres with Keck/OSIRIS

Looking forward, we will continue collaborative efforts with the Imaging Spectroscopy Survey of Exoplanetary Atmospheres with Keck/OSIRIS. We will be continuing our efforts in the *K*-band, but will also be obtaining *J*-band data of directly imaged planets to build a comprehensive spectral library of (R$\sim$4,000). By pushing to shorter wavelengths, we will be able to measure metallicities more precisely than with just the K-band data. This is in an effort to explore bulk metallicity as a diagnostic of formation that offers a critical tool beyond the C/O ratio. We will also be adding the results with JWST NIRSpec directly imaged planets to this library in an effort to create a larger, more comprehensive library to aid in characterizing this unique population of exoplanets.

Bibliography

Allard, F., Hauschildt, P. H., Alexander, D. R., Tamanai, A., & Schweitzer, A. 2001, The Limiting Effects of Dust in Brown Dwarf Model Atmospheres, , 556, 357

Allard, F., Homeier, D., & Freytag, B. 2012, Models of very-low-mass stars, brown dwarfs and exoplanets, Philosophical Transactions of the Royal Society of London Series A, 370, 2765

Allers, K. N., & Liu, M. C. 2013, A Near-infrared Spectroscopic Study of Young Field Ultracool Dwarfs, , 772, 79

Bailey, V., Hinz, P. M., Currie, T., Su, K. Y. L., Esposito, S., Hill, J. M., Hoffmann, W. F., Jones, T., Kim, J., Leisenring, J., Meyer, M., Murray-Clay, R., Nelson, M. J., Pinna, E., Puglisi, A., Rieke, G., Rodigas, T., Skemer, A., Skrutskie, M. F., Vaitheeswaran, V., & Wilson, J. C. 2013, A Thermal Infrared Imaging Study of Very Low Mass, Wide-separation Brown Dwarf Companions to Upper Scorpius Stars: Constraining Circumstellar Environments, , 767, 31

Baraffe, I., Chabrier, G., & Barman, T. 2008, Structure and evolution of super-Earth to super-Jupiter exoplanets. I. Heavy element enrichment in the interior, , 482, 315

Baraffe, I., Homeier, D., Allard, F., & Chabrier, G. 2015, New evolutionary models for pre-main sequence and main sequence low-mass stars down to the hydrogen-burning limit, , 577, A42

Barman, T. S., Konopacky, Q. M., Macintosh, B., & Marois, C. 2015, Simultaneous Detection of Water, Methane, and Carbon Monoxide in the Atmosphere of Exoplanet HR8799b, , 804, 61

Barman, T. S., Macintosh, B., Konopacky, Q. M., & Marois, C. 2011, Clouds and Chemistry in the Atmosphere of Extrasolar Planet HR8799b, , 733, 65

Batygin, K. 2018, On the Terminal Rotation Rates of Giant Planets, , 155, 178

Becker, J. C., Johnson, J. A., Vanderburg, A., & Morton, T. D. 2015, Extracting Radial Velocities of A- and B-type Stars from Echelle Spectrograph Calibration Spectra, , 217, 29

Bell, C. P. M., Mamajek, E. E., & Naylor, T. 2015, A self-consistent, absolute isochronal age scale for young moving groups in the solar neighbourhood, , 454, 593

Biller, B. A., Liu, M. C., Wahhaj, Z., Nielsen, E. L., Hayward, T. L., Males, J. R., Skemer, A., Close, L. M., Chun, M., Ftaclas, C., Clarke, F., Thatte, N., Shkolnik, E. L., Reid, I. N., Hartung, M., Boss, A., Lin, D., Alencar, S. H. P., de Gouveia Dal Pino, E., Gregorio-Hetem, J., & Toomey, D. 2013, The Gemini/NICI Planet-Finding Campaign: The Frequency of Planets around Young Moving Group Stars, , 777, 160

Birnstiel, T., Dullemond, C. P., & Brauer, F. 2010, Gas- and dust evolution in protoplanetary disks, , 513, A79

Blake, C. H., Charbonneau, D., & White, R. J. 2010, The NIRSPEC Ultracool Dwarf Radial Velocity Survey, , 723, 684

Blunt, S., Nielsen, E. L., De Rosa, R. J., Konopacky, Q. M., Ryan, D., Wang, J. J., Pueyo, L., Rameau, J., Marois, C., Marchis, F., Macintosh, B., Graham, J. R., Duchêne, G., & Schneider, A. C. 2017, Orbits for the Impatient: A Bayesian Rejection-sampling Method for Quickly Fitting the Orbits of Long-period Exoplanets, , 153, 229

Bodenheimer, P., & Pollack, J. B. 1986, Calculations of the accretion and evolution of giant planets: The effects of solid cores, , 67, 391

Bohn, A. J., Kenworthy, M. A., Ginski, C., Manara, C. F., Pecaut, M. J., de Boer, J., Keller, C. U., Mamajek, E. E., Meshkat, T., Reggiani, M., Todorov, K. O., & Snik, F. 2020a, The Young Suns Exoplanet Survey: Detection of a wide-orbit planetary-mass companion to a solar-type Sco-Cen member, , 492, 431

Bohn, A. J., Kenworthy, M. A., Ginski, C., Rieder, S., Mamajek, E. E., Meshkat, T., Pecaut, M. J., Reggiani, M., de Boer, J., Keller, C. U., Snik, F., & Southworth, J. 2020b, Two Directly Imaged, Wide-orbit Giant Planets around the Young, Solar Analog TYC 8998-760-1, , 898, L16

Bonavita, M., Daemgen, S., Desidera, S., Jayawardhana, R., Janson, M., & Lafrenière, D. 2014, A New Sub-stellar Companion around the Young Star HD 284149, , 791, L40

Bonavita, M., D'Orazi, V., Mesa, D., Fontanive, C., Desidera, S., Messina, S., Daemgen, S., Gratton, R., Vigan, A., Bonnefoy, M., Zurlo, A., Antichi, J., Avenhaus, H., Baruffolo, A., Baudino, J. L., Beuzit, J. L., Boccaletti, A., Bruno, P., Buey, T., Carbillet, M., Cascone, E., Chauvin, G., Claudi, R. U., De Caprio, V., Fantinel, D., Farisato, G., Feldt, M., Galicher, R., Giro, E., Gry, C., Hagelberg, J., Incorvaia, S., Janson, M., Jaquet, M., Lagrange, A. M., Langlois, M., Lannier, J., Le Coroller, H., Lessio, L., Ligi, R., Maire, A. L., Meyer, M., Menard, F., Perrot, C., Peretti, S., Petit, C., Ramos, J., Roux, A., Salasnich, B., Salter, G., Samland, M., Scuderi, S., Schlieder, J., Surez, M., Turatto, M., & Weber, L. 2017, Orbiting a binary. SPHERE characterisation of the HD 284149 system, , 608, A106

Bonnefoy, M., Currie, T., Marleau, G. D., Schlieder, J. E., Wisniewski, J., Carson, J., Covey,

K. R., Henning, T., Biller, B., Hinz, P., Klahr, H., Marsh Boyer, A. N., Zimmerman, N., Janson, M., McElwain, M., Mordasini, C., Skemer, A., Bailey, V., Defrère, D., Thalmann, C., Skrutskie, M., Allard, F., Homeier, D., Tamura, M., Feldt, M., Cumming, A., Grady, C., Brandner, W., Helling, C., Witte, S., Hauschildt, P., Kandori, R., Kuzuhara, M., Fukagawa, M., Kwon, J., Kudo, T., Hashimoto, J., Kusakabe, N., Abe, L., Brandt, T., Egner, S., Guyon, O., Hayano, Y., Hayashi, M., Hayashi, S., Hodapp, K., Ishii, M., Iye, M., Knapp, G., Matsuo, T., Mede, K., Miyama, M., Morino, J. I., Moro-Martin, A., Nishimura, T., Pyo, T., Serabyn, E., Suenaga, T., Suto, H., Suzuki, R., Takahashi, Takami, M., Takato, N., Terada, H., Tomono, D., Turner, E., Watanabe, M., Yamada, T., Takami, H., & Usuda, T. 2014, Characterization of the gaseous companion κ Andromedae b. New Keck and LBTI high-contrast observations, , 562, A111

Booth, A. S., van der Marel, N., Leemker, M., van Dishoeck, E. F., & Ohashi, S. 2021, A major asymmetric ice trap in a planet-forming disk. II. Prominent SO and SO_2 pointing to C/O < 1, , 651, L6

Booth, R. A., Clarke, C. J., Madhusudhan, N., & Ilee, J. D. 2017, Chemical enrichment of giant planets and discs due to pebble drift, , 469, 3994

Boss, A. P. 2002, Collapse and Fragmentation of Molecular Cloud Cores. VII. Magnetic Fields and Multiple Protostar Formation, , 568, 743

Bowler, B. P. 2016, Imaging Extrasolar Giant Planets, , 128, 102001

Bowler, B. P., Zhou, Y., Morley, C. V., Kataria, T., Bryan, M. L., Benneke, B., & Batygin, K. 2020, Strong Near-infrared Spectral Variability of the Young Cloudy L Dwarf Companion VHS J1256-1257 b, , 893, L30

Bowler, B. P., Hinkley, S., Ziegler, C., Baranec, C., Gizis, J. E., Law, N. M., Liu, M. C., Shah, V. S., Shkolnik, E. L., Riaz, B., & Riddle, R. 2019, The Elusive Majority of Young Moving Groups. I. Young Binaries and Lithium-rich Stars in the Solar Neighborhood, , 877, 60

Brock, L., Barman, T., Konopacky, Q. M., & Stone, J. M. 2021, Cloud Properties of Brown Dwarf Binaries across the L/T Transition, , 914, 124

Bryan, M. L., Benneke, B., Knutson, H. A., Batygin, K., & Bowler, B. P. 2018, Constraints on the spin evolution of young planetary-mass companions, Nature Astronomy, 2, 138

Burgasser, A. J., Lopez, M. A., Mamajek, E. E., Gagné, J., Faherty, J. K., Tallis, M., Choban, C., Tamiya, T., Escala, I., & Aganze, C. 2016, The First Brown Dwarf/Planetary-mass Object in the 32 Orionis Group, , 820, 32

Burningham, B., Marley, M. S., Line, M. R., Lupu, R., Visscher, C., Morley, C. V., Saumon, D., & Freedman, R. 2017, Retrieval of atmospheric properties of cloudy L dwarfs, , 470, 1177

Cai, K., Durisen, R. H., Michael, S., Boley, A. C., Mejía, A. C., Pickett, M. K., & D'Alessio, P. 2006, Erratum: "The Effects of Metallicity and Grain Size on Gravitational Instabilities in Protoplanetary Disks" (<A href="/abs/2006ApJ.. .636L.149">ApJ 636, L149 [2006]</A>), , 642, L173

Cameron, A. G. W. 1978, Physics of the Primitive Solar Accretion Disk, Moon and Planets, 18, 5

Carson, J., Thalmann, C., Janson, M., Kozakis, T., Bonnefoy, M., Biller, B., Schlieder, J., Currie, T., McElwain, M., Goto, M., Henning, T., Brandner, W., Feldt, M., Kandori, R., Kuzuhara, M., Stevens, L., Wong, P., Gainey, K., Fukagawa, M., Kuwada, Y., Brandt, T., Kwon, J., Abe, L., Egner, S., Grady, C., Guyon, O., Hashimoto, J., Hayano, Y., Hayashi, M., Hayashi, S., Hodapp, K., Ishii, M., Iye, M., Knapp, G., Kudo, T., Kusakabe, N., Matsuo, T., Miyama, S., Morino, J., Moro-Martin, A., Nishimura, T., Pyo, T., Serabyn, E., Suto, H., Suzuki, R., Takami, M., Takato, N., Terada, H., Tomono, D., Turner, E., Watanabe, M., Wisniewski, J., Yamada, T., Takami, H., Usuda, T., & Tamura, M. 2013, Direct Imaging Discovery of a "Super-Jupiter" around the Late B-type Star κ And, , 763, L32

Chabrier, G., & Baraffe, I. 2007, Heat Transport in Giant (Exo)planets: A New Perspective, , 661, L81

Chabrier, G., Baraffe, I., Allard, F., & Hauschildt, P. 2000, Evolutionary Models for Very Low-Mass Stars and Brown Dwarfs with Dusty Atmospheres, , 542, 464

Chambers, J. E. 2009, Planetary Migration: What Does It Mean for Planet Formation?, Annual Review of Earth and Planetary Sciences, 37, 321

Changeat, Q., Al-Refaie, A., Mugnai, L. V., Edwards, B., Waldmann, I. P., Pascale, E., & Tinetti, G. 2020, Alfnoor: A Retrieval Simulation of the Ariel Target List, , 160, 80

Changeat, Q., Edwards, B., Al-Refaie, A. F., Tsiaras, A., Skinner, J. W., Cho, J. Y. K., Yip, K. H., Anisman, L., Ikoma, M., Bieger, M. F., Venot, O., Shibata, S., Waldmann, I. P., & Tinetti, G. 2022, Five Key Exoplanet Questions Answered via the Analysis of 25 Hot-Jupiter Atmospheres in Eclipse, , 260, 3

Chatterjee, S., Ford, E. B., Matsumura, S., & Rasio, F. A. 2008, Dynamical Outcomes of Planet-Planet Scattering, , 686, 580

Chauvin, G., Lagrange, A. M., Dumas, C., Zuckerman, B., Mouillet, D., Song, I., Beuzit, J. L., & Lowrance, P. 2004, A giant planet candidate near a young brown dwarf. Direct VLT/NACO observations using IR wavefront sensing, , 425, L29

Chauvin, G., Lagrange, A. M., Zuckerman, B., Dumas, C., Mouillet, D., Song, I., Beuzit, J. L., Lowrance, P., & Bessell, M. S. 2005, A companion to AB Pic at the planet/brown dwarf boundary, , 438, L29

Chin, J. C. Y., Wizinowich, P., Campbell, R., Chock, L., Cooper, A., James, E., Lyke, J., Mastromarino, J., Martin, O., Medeiros, D., Morrison, D., Neyman, C., Panteleev, S., Stalcup, T., Tucker, P., Wetherell, E., & van Dam, M. 2012, in Society of Photo-Optical Instrumentation Engineers (SPIE) Conference Series, Vol. 8447, Adaptive Optics Systems III, ed. B. L. Ellerbroek, E. Marchetti, & J.-P. Véran, 84474F

Cridland, A. J., Bosman, A. D., & van Dishoeck, E. F. 2020, Impact of vertical gas accretion on the carbon-to-oxygen ratio of gas giant atmospheres, , 635, A68

Cridland, A. J., van Dishoeck, E. F., Alessi, M., & Pudritz, R. E. 2019, Connecting planet formation and astrochemistry. A main sequence for C/O in hot exoplanetary atmospheres, , 632, A63

Cruz, K. L., Núñez, A., Burgasser, A. J., Abrahams, E., Rice, E. L., Reid, I. N., & Looper, D. 2018, Meeting the Cool Neighbors. XII. An Optically Anchored Analysis of the Near-infrared Spectra of L Dwarfs, , 155, 34

Currie, T., Brandt, T. D., Uyama, T., Nielsen, E. L., Blunt, S., Guyon, O., Tamura, M., Marois, C., Mede, K., Kuzuhara, M., Groff, T. D., Jovanovic, N., Kasdin, N. J., Lozi, J., Hodapp, K., Chilcote, J., Carson, J., Martinache, F., Goebel, S., Grady, C., McElwain, M., Akiyama, E., Asensio-Torres, R., Hayashi, M., Janson, M., Knapp, G. R., Kwon, J., Nishikawa, J., Oh, D., Schlieder, J., Serabyn, E., Sitko, M., & Skaf, N. 2018, SCExAO/CHARIS Near-infrared Direct Imaging, Spectroscopy, and Forward-Modeling of κ And b: A Likely Young, Low-gravity Superjovian Companion, , 156, 291

Cushing, M. C., Rayner, J. T., & Vacca, W. D. 2005, An Infrared Spectroscopic Sequence of M, L, and T Dwarfs, , 623, 1115

Daemgen, S., Bonavita, M., Jayawardhana, R., Lafrenière, D., & Janson, M. 2015, Sub-stellar Companions and Stellar Multiplicity in the Taurus Star-forming Region, , 799, 155

David, T. J., & Hillenbrand, L. A. 2015, The Ages of Early-type Stars: Strömgren Photometric Methods Calibrated, Validated, Tested, and Applied to Hosts and Prospective Hosts of Directly Imaged Exoplanets, , 804, 146

Delorme, J.-R., Jovanovic, N., Echeverri, D., Mawet, D., Kent Wallace, J., Bartos, R. D., Cetre, S., Wizinowich, P., Ragland, S., Lilley, S., Wetherell, E., Doppmann, G., Wang, J. J., Morris, E. C., Ruffio, J.-B., Martin, E. C., Fitzgerald, M. P., Ruane, G., Schofield, T., Suominen, N., Calvin, B., Wang, E., Magnone, K., Johnson, C., Sohn, J. M., López, R. A., Bond, C. Z., Pezzato, J., Sayson, J. L., Chun, M., & Skemer, A. J. 2021, Keck Planet Imager and Characterizer: a dedicated single-mode fiber injection unit for high-resolution exoplanet spectroscopy, Journal of Astronomical Telescopes, Instruments, and Systems, 7, 035006

Dodson-Robinson, S. E., Veras, D., Ford, E. B., & Beichman, C. A. 2009, The Formation

Mechanism of Gas Giants on Wide Orbits, , 707, 79

Dupuy, T. J., Liu, M. C., Magnier, E. A., Best, W. M. J., Baraffe, I., Chabrier, G., Forveille, T., Metchev, S. A., & Tremblin, P. 2020, The Parallax of VHS J1256-1257 from CFHT and Pan-STARRS-1, Research Notes of the American Astronomical Society, 4, 54

Eistrup, C., Walsh, C., & van Dishoeck, E. F. 2018, Molecular abundances and C/O ratios in chemically evolving planet-forming disk midplanes, , 613, A14

Fabrycky, D. C., & Murray-Clay, R. A. 2010, Stability of the Directly Imaged Multiplanet System HR 8799: Resonance and Masses, , 710, 1408

Faherty, J. K., Rice, E. L., Cruz, K. L., Mamajek, E. E., & Núñez, A. 2013, 2MASS J035523.37+113343.7: A Young, Dusty, Nearby, Isolated Brown Dwarf Resembling a Giant Exoplanet, , 145, 2

Feroz, F., Hobson, M. P., & Bridges, M. 2009, MULTINEST: an efficient and robust Bayesian inference tool for cosmology and particle physics, , 398, 1601

Foreman-Mackey, D., Conley, A., Meierjurgen Farr, W., Hogg, D. W., Lang, D., Marshall, P., Price-Whelan, A., Sanders, J., & Zuntz, J. 2013, emcee: The MCMC Hammer

Gaia Collaboration, Brown, A. G. A., Vallenari, A., Prusti, T., de Bruijne, J. H. J., Babusiaux, C., Bailer-Jones, C. A. L., Biermann, M., Evans, D. W., Eyer, L., Jansen, F., Jordi, C., Klioner, S. A., Lammers, U., Lindegren, L., Luri, X., Mignard, F., Panem, C., Pourbaix, D., Randich, S., Sartoretti, P., Siddiqui, H. I., Soubiran, C., van Leeuwen, F., Walton, N. A., Arenou, F., Bastian, U., Cropper, M., Drimmel, R., Katz, D., Lattanzi, M. G., Bakker, J., Cacciari, C., Castañeda, J., Chaoul, L., Cheek, N., De Angeli, F., Fabricius, C., Guerra, R., Holl, B., Masana, E., Messineo, R., Mowlavi, N., Nienartowicz, K., Panuzzo, P., Portell, J., Riello, M., Seabroke, G. M., Tanga, P., Thévenin, F., Gracia-Abril, G., Comoretto, G., Garcia-Reinaldos, M., Teyssier, D., Altmann, M., Andrae, R., Audard, M., Bellas-Velidis, I., Benson, K., Berthier, J., Blomme, R., Burgess, P., Busso, G., Carry, B., Cellino, A., Clementini, G., Clotet, M., Creevey, O., Davidson, M., De Ridder, J., Delchambre, L., Dell'Oro, A., Ducourant, C., Fernández-Hernández, J., Fouesneau, M., Frémat, Y., Galluccio, L., García-Torres, M., González-Núñez, J., González-Vidal, J. J., Gosset, E., Guy, L. P., Halbwachs, J. L., Hambly, N. C., Harrison, D. L., Hernández, J., Hestroffer, D., Hodgkin, S. T., Hutton, A., Jasniewicz, G., Jean-Antoine-Piccolo, A., Jordan, S., Korn, A. J., Krone-Martins, A., Lanzafame, A. C., Lebzelter, T., Löffler, W., Manteiga, M., Marrese, P. M., Martín-Fleitas, J. M., Moitinho, A., Mora, A., Muinonen, K., Osinde, J., Pancino, E., Pauwels, T., Petit, J. M., Recio-Blanco, A., Richards, P. J., Rimoldini, L., Robin, A. C., Sarro, L. M., Siopis, C., Smith, M., Sozzetti, A., Süveges, M., Torra, J., van Reeven, W., Abbas, U., Abreu Aramburu, A., Accart, S., Aerts, C., Altavilla, G., Álvarez, M. A., Alvarez, R., Alves, J., Anderson, R. I., Andrei, A. H., Anglada Varela, E., Antiche, E., Antoja, T., Arcay, B., Astraatmadja, T. L., Bach, N., Baker, S. G., Balaguer-Núñez, L., Balm, P., Barache, C., Barata, C., Barbato, D., Barblan, F., Barklem, P. S., Barrado, D., Barros, M., Barstow, M. A.,

Bartholomé Muñoz, S., Bassilana, J. L., Becciani, U., Bellazzini, M., Berihuete, A., Bertone, S., Bianchi, L., Bienaymé, O., Blanco-Cuaresma, S., Boch, T., Boeche, C., Bombrun, A., Borrachero, R., Bossini, D., Bouquillon, S., Bourda, G., Bragaglia, A., Bramante, L., Breddels, M. A., Bressan, A., Brouillet, N., Brüsemeister, T., Brugaletta, E., Bucciarelli, B., Burlacu, A., Busonero, D., Butkevich, A. G., Buzzi, R., Caffau, E., Cancelliere, R., Cannizzaro, G., Cantat-Gaudin, T., Carballo, R., Carlucci, T., Carrasco, J. M., Casamiquela, L., Castellani, M., Castro-Ginard, A., Charlot, P., Chemin, L., Chiavassa, A., Cocozza, G., Costigan, G., Cowell, S., Crifo, F., Crosta, M., Crowley, C., Cuypers, J., Dafonte, C., Damerdji, Y., Dapergolas, A., David, P., David, M., de Laverny, P., De Luise, F., De March, R., de Martino, D., de Souza, R., de Torres, A., Debosscher, J., del Pozo, E., Delbo, M., Delgado, A., Delgado, H. E., Di Matteo, P., Diakite, S., Diener, C., Distefano, E., Dolding, C., Drazinos, P., Durán, J., Edvardsson, B., Enke, H., Eriksson, K., Esquej, P., Eynard Bontemps, G., Fabre, C., Fabrizio, M., Faigler, S., Falcão, A. J., Farràs Casas, M., Federici, L., Fedorets, G., Fernique, P., Figueras, F., Filippi, F., Findeisen, K., Fonti, A., Fraile, E., Fraser, M., Frézouls, B., Gai, M., Galleti, S., Garabato, D., García-Sedano, F., Garofalo, A., Garralda, N., Gavel, A., Gavras, P., Gerssen, J., Geyer, R., Giacobbe, P., Gilmore, G., Girona, S., Giuffrida, G., Glass, F., Gomes, M., Granvik, M., Gueguen, A., Guerrier, A., Guiraud, J., Gutiérrez-Sánchez, R., Haigron, R., Hatzidimitriou, D., Hauser, M., Haywood, M., Heiter, U., Helmi, A., Heu, J., Hilger, T., Hobbs, D., Hofmann, W., Holland, G., Huckle, H. E., Hypki, A., Icardi, V., Janßen, K., Jevardat de Fombelle, G., Jonker, P. G., Juhász, Á. L., Julbe, F., Karampelas, A., Kewley, A., Klar, J., Kochoska, A., Kohley, R., Kolenberg, K., Kontizas, M., Kontizas, E., Koposov, S. E., Kordopatis, G., Kostrzewa-Rutkowska, Z., Koubsky, P., Lambert, S., Lanza, A. F., Lasne, Y., Lavigne, J. B., Le Fustec, Y., Le Poncin-Lafitte, C., Lebreton, Y., Leccia, S., Leclerc, N., Lecoeur-Taibi, I., Lenhardt, H., Leroux, F., Liao, S., Licata, E., Lindstrøm, H. E. P., Lister, T. A., Livanou, E., Lobel, A., López, M., Managau, S., Mann, R. G., Mantelet, G., Marchal, O., Marchant, J. M., Marconi, M., Marinoni, S., Marschalkó, G., Marshall, D. J., Martino, M., Marton, G., Mary, N., Massari, D., Matijevič, G., Mazeh, T., McMillan, P. J., Messina, S., Michalik, D., Millar, N. R., Molina, D., Molinaro, R., Molnár, L., Montegriffo, P., Mor, R., Morbidelli, R., Morel, T., Morris, D., Mulone, A. F., Muraveva, T., Musella, I., Nelemans, G., Nicastro, L., Noval, L., O'Mullane, W., Ordénovic, C., Ordóñez-Blanco, D., Osborne, P., Pagani, C., Pagano, I., Pailler, F., Palacin, H., Palaversa, L., Panahi, A., Pawlak, M., Piersimoni, A. M., Pineau, F. X., Plachy, E., Plum, G., Poggio, E., Poujoulet, E., Prša, A., Pulone, L., Racero, E., Ragaini, S., Rambaux, N., Ramos-Lerate, M., Regibo, S., Reylé, C., Riclet, F., Ripepi, V., Riva, A., Rivard, A., Rixon, G., Roegiers, T., Roelens, M., Romero-Gómez, M., Rowell, N., Royer, F., Ruiz-Dern, L., Sadowski, G., Sagristà Sellés, T., Sahlmann, J., Salgado, J., Salguero, E., Sanna, N., Santana-Ros, T., Sarasso, M., Savietto, H., Schultheis, M., Sciacca, E., Segol, M., Segovia, J. C., Ségransan, D., Shih, I. C., Siltala, L., Silva, A. F., Smart, R. L., Smith, K. W., Solano, E., Solitro, F., Sordo, R., Soria Nieto, S., Souchay, J., Spagna, A., Spoto, F., Stampa, U., Steele, I. A., Steidelmüller, H., Stephenson, C. A., Stoev, H., Suess, F. F., Surdej, J., Szabados, L., Szegedi-Elek, E., Tapiador, D., Taris, F., Tauran, G., Taylor, M. B., Teixeira, R., Terrett, D., Teyssandier, P., Thuillot, W., Titarenko, A., Torra Clotet, F., Turon, C., Ulla, A., Utrilla, E., Uzzi, S., Vaillant, M., Valentini, G., Valette, V., van Elteren, A., Van Hemelryck, E., van Leeuwen, M., Vaschetto, M., Vecchiato, A., Veljanoski, J., Viala, Y., Vicente, D., Vogt, S., von Essen, C., Voss, H., Votruba, V., Voutsinas, S., Walmsley, G., Weiler, M., Wertz, O.,

Wevers, T., Wyrzykowski, Ł., Yoldas, A., Žerjal, M., Ziaeepour, H., Zorec, J., Zschocke, S., Zucker, S., Zurbach, C., & Zwitter, T. 2018, Gaia Data Release 2. Summary of the contents and survey properties, , 616, A1

Galicher, R., Marois, C., Macintosh, B., Zuckerman, B., Barman, T., Konopacky, Q., Song, I., Patience, J., Lafrenière, D., Doyon, R., & Nielsen, E. L. 2016, The International Deep Planet Survey. II. The frequency of directly imaged giant exoplanets with stellar mass, , 594, A63

Gauza, B., Béjar, V. J. S., Pérez-Garrido, A., Zapatero Osorio, M. R., Lodieu, N., Rebolo, R., Pallé, E., & Nowak, G. 2015, Discovery of a Young Planetary Mass Companion to the Nearby M Dwarf VHS J125601.92-125723.9, , 804, 96

Goldreich, P., & Tremaine, S. 1980, Disk-satellite interactions., , 241, 425

Goldreich, P., & Ward, W. R. 1973, The Formation of Planetesimals, , 183, 1051

Gontcharov, G. A. 2006, Pulkovo Compilation of Radial Velocities for 35 495 Hipparcos stars in a common system, Astronomy Letters, 32, 759

Gonzales, E. C., Burningham, B., Faherty, J. K., Cleary, C., Visscher, C., Marley, M. S., Lupu, R., & Freedman, R. 2020, Retrieval of the d/sdL7+T7.5p Binary SDSS J1416+1348AB, , 905, 46

Goodman, J., & Weare, J. 2010, Ensemble samplers with affine invariance, Communications in Applied Mathematics and Computational Science, 5, 65

Gravity Collaboration, Abuter, R., Accardo, M., Amorim, A., Anugu, N., Ávila, G., Azouaoui, N., Benisty, M., Berger, J. P., Blind, N., Bonnet, H., Bourget, P., Brandner, W., Brast, R., Buron, A., Burtscher, L., Cassaing, F., Chapron, F., Choquet, É., Clénet, Y., Collin, C., Coudé Du Foresto, V., de Wit, W., de Zeeuw, P. T., Deen, C., Delplancke-Ströbele, F., Dembet, R., Derie, F., Dexter, J., Duvert, G., Ebert, M., Eckart, A., Eisenhauer, F., Esselborn, M., Fédou, P., Finger, G., Garcia, P., Garcia Dabo, C. E., Garcia Lopez, R., Gendron, E., Genzel, R., Gillessen, S., Gonte, F., Gordo, P., Grould, M., Grözinger, U., Guieu, S., Haguenauer, P., Hans, O., Haubois, X., Haug, M., Haussmann, F., Henning, T., Hippler, S., Horrobin, M., Huber, A., Hubert, Z., Hubin, N., Hummel, C. A., Jakob, G., Janssen, A., Jochum, L., Jocou, L., Kaufer, A., Kellner, S., Kendrew, S., Kern, L., Kervella, P., Kiekebusch, M., Klein, R., Kok, Y., Kolb, J., Kulas, M., Lacour, S., Lapeyrère, V., Lazareff, B., Le Bouquin, J. B., Lèna, P., Lenzen, R., Lévêque, S., Lippa, M., Magnard, Y., Mehrgan, L., Mellein, M., Mérand, A., Moreno-Ventas, J., Moulin, T., Müller, E., Müller, F., Neumann, U., Oberti, S., Ott, T., Pallanca, L., Panduro, J., Pasquini, L., Paumard, T., Percheron, I., Perraut, K., Perrin, G., Pflüger, A., Pfuhl, O., Phan Duc, T., Plewa, P. M., Popovic, D., Rabien, S., Ramírez, A., Ramos, J., Rau, C., Riquelme, M., Rohloff, R. R., Rousset, G., Sanchez-Bermudez, J., Scheithauer, S., Schöller, M., Schuhler, N., Spyromilio, J., Straubmeier, C., Sturm, E., Suarez, M., Tristram, K. R. W., Ventura, N., Vincent, F., Waisberg, I., Wank, I., Weber, J., Wieprecht,

E., Wiest, M., Wiezorrek, E., Wittkowski, M., Woillez, J., Wolff, B., Yazici, S., Ziegler, D., & Zins, G. 2017, First light for GRAVITY: Phase referencing optical interferometry for the Very Large Telescope Interferometer, , 602, A94

Haffert, S. Y., Bohn, A. J., de Boer, J., Snellen, I. A. G., Brinchmann, J., Girard, J. H., Keller, C. U., & Bacon, R. 2019, Two accreting protoplanets around the young star PDS 70, Nature Astronomy, 3, 749

Hargreaves, R. J., Gordon, I. E., Rey, M., Nikitin, A. V., Tyuterev, V. G., Kochanov, R. V., & Rothman, L. S. 2020, An Accurate, Extensive, and Practical Line List of Methane for the HITEMP Database, , 247, 55

Hauschildt, P. H., Allard, F., & Baron, E. 1999, The NextGen Model Atmosphere Grid for 3000<=T_{eff}<=10,000 K, , 512, 377

Hayashi, C., Nakazawa, K., & Nakagawa, Y. 1985, in Protostars and Planets II, ed. D. C. Black & M. S. Matthews, 1100

Helled, R., & Bodenheimer, P. 2011, The effects of metallicity and grain growth and settling on the early evolution of gaseous protoplanets, , 211, 939

Helled, R., & Schubert, G. 2009, Heavy-element Enrichment of a Jupiter-mass Protoplanet as a Function of Orbital Location, , 697, 1256

Hinkley, S., Pueyo, L., Faherty, J. K., Oppenheimer, B. R., Mamajek, E. E., Kraus, A. L., Rice, E. L., Ireland, M. J., David, T., Hillenbrand, L. A., Vasisht, G., Cady, E., Brenner, D., Veicht, A., Nilsson, R., Zimmerman, N., Parry, I. R., Beichman, C., Dekany, R., Roberts, J. E., Roberts, Lewis C., J., Baranec, C., Crepp, J. R., Burruss, R., Wallace, J. K., King, D., Zhai, C., Lockhart, T., Shao, M., Soummer, R., Sivaramakrishnan, A., & Wilson, L. A. 2013, The κ Andromedae System: New Constraints on the Companion Mass, System Age, and Further Multiplicity, , 779, 153

Hinkley, S., Baraffe, I., Biller, B., Bonnefoy, M., Bowler, B., Chen, C., Choquet, E., Currie, T. M., Danielski, C., Fortney, J., Grady, C. A., Greenbaum, A., Hines, D. C., Janson, M. R., Kalas, P. G., Kennedy, G., Kraus, A. L., Lagrange, A.-M., Liu, M. C., Marley, M. S., Marois, C., Matthews, B., Mawet, D., Metchev, S. A., Meyer, M. R., Millar-Blanchaer, M. A., Perrin, M., Pueyo, L., Quanz, S. P., Rameau, J., Rodigas, T. J., Sallum, S., Sargent, B., Schlieder, J., Schneider, G., Skemer, A., Stapelfeldt, K., Tremblin, P., Vigan, A., & Ygouf, M. 2017, High Contrast Imaging of Exoplanets and Exoplanetary Systems with JWST, JWST Proposal ID 1386. Cycle 0 Early Release Science

Hoch, K. K. W., Konopacky, Q. M., Barman, T. S., Theissen, C. A., Brock, L., Perrin, M. D., Ruffio, J.-B., Macintosh, B., & Marois, C. 2022, Moderate-Resolution *K*-Band Spectroscopy of the Substellar Companion VHS 1256 b, arXiv e-prints, arXiv:2207.03819

Hoeijmakers, H. J., Schwarz, H., Snellen, I. A. G., de Kok, R. J., Bonnefoy, M., Chauvin, G., Lagrange, A. M., & Girard, J. H. 2018, Medium-resolution integral-field spectroscopy for high-contrast exoplanet imaging. Molecule maps of the β Pictoris system with SINFONI, , 617, A144

Hsu, C.-C., Burgasser, A. J., Theissen, C. A., Gelino, C. R., Birky, J. L., Diamant, S. J. M., Bardalez Gagliuffi, D. C., Aganze, C., Blake, C. H., & Faherty, J. K. 2021, The Brown Dwarf Kinematics Project (BDKP). V. Radial and Rotational Velocities of T Dwarfs from Keck/NIRSPEC High-resolution Spectroscopy, , 257, 45

Hubeny, I., & Burrows, A. 2007, A Systematic Study of Departures from Chemical Equilibrium in the Atmospheres of Substellar Mass Objects, , 669, 1248

Husser, T. O., Wende-von Berg, S., Dreizler, S., Homeier, D., Reiners, A., Barman, T., & Hauschildt, P. H. 2013, A new extensive library of PHOENIX stellar atmospheres and synthetic spectra, , 553, A6

Ikoma, M., Nakazawa, K., & Emori, H. 2000, Formation of Giant Planets: Dependences on Core Accretion Rate and Grain Opacity, , 537, 1013

Johansen, A., & Lambrechts, M. 2017, Forming Planets via Pebble Accretion, Annual Review of Earth and Planetary Sciences, 45, 359

Johnston, K., Daniel, K., & Besla, G. 2022, in AAS/Division of Dynamical Astronomy Meeting, Vol. 54, AAS/Division of Dynamical Astronomy Meeting, 304.01

Jones, J., White, R. J., Quinn, S., Ireland, M., Boyajian, T., Schaefer, G., & Baines, E. K. 2016, The Age of the Directly Imaged Planet Host Star κ Andromedae Determined from Interferometric Observations, , 822, L3

Kaeufl, H.-U., Ballester, P., Biereichel, P., Delabre, B., Donaldson, R., Dorn, R., Fedrigo, E., Finger, G., Fischer, G., Franza, F., Gojak, D., Huster, G., Jung, Y., Lizon, J.-L., Mehrgan, L., Meyer, M., Moorwood, A., Pirard, J.-F., Paufique, J., Pozna, E., Siebenmorgen, R., Silber, A., Stegmeier, J., & Wegerer, S. 2004, in Society of Photo-Optical Instrumentation Engineers (SPIE) Conference Series, Vol. 5492, Ground-based Instrumentation for Astronomy, ed. A. F. M. Moorwood & M. Iye, 1218

Kalas, P., Graham, J. R., Chiang, E., Fitzgerald, M. P., Clampin, M., Kite, E. S., Stapelfeldt, K., Marois, C., & Krist, J. 2008, Optical Images of an Exosolar Planet 25 Light-Years from Earth, Science, 322, 1345

Karkoschka, E., & Tomasko, M. G. 2010, Methane absorption coefficients for the jovian planets from laboratory, Huygens, and HST data, , 205, 674

Kesseli, A. Y., Kirkpatrick, J. D., Fajardo-Acosta, S. B., Penny, M. T., Gaudi, B. S., Veyette, M., Boeshaar, P. C., Henderson, C. B., Cushing, M. C., Calchi-Novati, S., Shvartzvald, Y., & Muirhead, P. S. 2019, Radii of 88 M Subdwarfs and Updated Radius Relations for Low-metallicity M-dwarf Stars, , 157, 63

Kirkpatrick, J. D. 2005, New Spectral Types L and T, , 43, 195

Kirkpatrick, J. D., Barman, T. S., Burgasser, A. J., McGovern, M. R., McLean, I. S., Tinney, C. G., & Lowrance, P. J. 2006, Discovery of a Very Young Field L Dwarf, 2MASS J01415823-4633574, , 639, 1120

Konopacky, Q. M., Barman, T. S., Macintosh, B. A., & Marois, C. 2013, Detection of Carbon Monoxide and Water Absorption Lines in an Exoplanet Atmosphere, Science, 339, 1398

Krabbe, A., Gasaway, T., Song, I., Iserlohe, C., Weiss, J., Larkin, J. E., Barczys, M., & Lafreniere, D. 2004, in Society of Photo-Optical Instrumentation Engineers (SPIE) Conference Series, Vol. 5492, Ground-based Instrumentation for Astronomy, ed. A. F. M. Moorwood & M. Iye, 1403

Kratter, K. M., Murray-Clay, R. A., & Youdin, A. N. 2010, The Runts of the Litter: Why Planets Formed Through Gravitational Instability Can Only Be Failed Binary Stars, , 710, 1375

Kraus, A. L., Herczeg, G. J., Rizzuto, A. C., Mann, A. W., Slesnick, C. L., Carpenter, J. M., Hillenbrand, L. A., & Mamajek, E. E. 2017, The Greater Taurus-Auriga Ecosystem. I. There is a Distributed Older Population, , 838, 150

Kraus, A. L., Ireland, M. J., Cieza, L. A., Hinkley, S., Dupuy, T. J., Bowler, B. P., & Liu, M. C. 2014, Three Wide Planetary-mass Companions to FW Tau, ROXs 12, and ROXs 42B, , 781, 20

Kuiper, G. P. 1951, On the Origin of the Solar System, Proceedings of the National Academy of Science, 37, 1

Kuzuhara, M., Tamura, M., Kudo, T., Janson, M., Kandori, R., Brandt, T. D., Thalmann, C., Spiegel, D., Biller, B., Carson, J., Hori, Y., Suzuki, R., Burrows, A., Henning, T., Turner, E. L., McElwain, M. W., Moro-Martín, A., Suenaga, T., Takahashi, Y. H., Kwon, J., Lucas, P., Abe, L., Brandner, W., Egner, S., Feldt, M., Fujiwara, H., Goto, M., Grady, C. A., Guyon, O., Hashimoto, J., Hayano, Y., Hayashi, M., Hayashi, S. S., Hodapp, K. W., Ishii, M., Iye, M., Knapp, G. R., Matsuo, T., Mayama, S., Miyama, S., Morino, J. I., Nishikawa, J., Nishimura, T., Kotani, T., Kusakabe, N., Pyo, T. S., Serabyn, E., Suto, H., Takami, M., Takato, N., Terada, H., Tomono, D., Watanabe, M., Wisniewski, J. P., Yamada, T., Takami, H., & Usuda, T. 2013, Direct Imaging of a Cold Jovian Exoplanet in Orbit around the Sun-like Star GJ 504, , 774, 11

Larkin, J., Barczys, M., Krabbe, A., Adkins, S., Aliado, T., Amico, P., Brims, G., Campbell, R.,

Canfield, J., Gasaway, T., Honey, A., Iserlohe, C., Johnson, C., Kress, E., LaFreniere, D., Lyke, J., Magnone, K., Magnone, N., McElwain, M., Moon, J., Quirrenbach, A., Skulason, G., Song, I., Spencer, M., Weiss, J., & Wright, S. 2006, in Society of Photo-Optical Instrumentation Engineers (SPIE) Conference Series, Vol. 6269, Society of Photo-Optical Instrumentation Engineers (SPIE) Conference Series, ed. I. S. McLean & M. Iye, 62691A

Li, C., Ingersoll, A., Bolton, S., Levin, S., Janssen, M., Atreya, S., Lunine, J., Steffes, P., Brown, S., Guillot, T., Allison, M., Arballo, J., Bellotti, A., Adumitroaie, V., Gulkis, S., Hodges, A., Li, L., Misra, S., Orton, G., Oyafuso, F., Santos-Costa, D., Waite, H., & Zhang, Z. 2020, The water abundance in Jupiter's equatorial zone, Nature Astronomy, 4, 609

Lin, D. N. C., & Papaloizou, J. 1986, On the Tidal Interaction between Protoplanets and the Protoplanetary Disk. III. Orbital Migration of Protoplanets, , 309, 846

Line, M. R., Marley, M. S., Liu, M. C., Burningham, B., Morley, C. V., Hinkel, N. R., Teske, J., Fortney, J. J., Freedman, R., & Lupu, R. 2017, Uniform Atmospheric Retrieval Analysis of Ultracool Dwarfs. II. Properties of 11 T dwarfs, , 848, 83

Liu, F., Bitsch, B., Asplund, M., Liu, B.-B., Murphy, M. T., Yong, D., Ting, Y.-S., & Feltzing, S. 2021, Detailed elemental abundances of binary stars: searching for signatures of planet formation and atomic diffusion, , 508, 1227

Liu, M. C., Dupuy, T. J., & Allers, K. N. 2016, The Hawaii Infrared Parallax Program. II. Young Ultracool Field Dwarfs, , 833, 96

Liu, M. C., Magnier, E. A., Deacon, N. R., Allers, K. N., Dupuy, T. J., Kotson, M. C., Aller, K. M., Burgett, W. S., Chambers, K. C., Draper, P. W., Hodapp, K. W., Jedicke, R., Kaiser, N., Kudritzki, R. P., Metcalfe, N., Morgan, J. S., Price, P. A., Tonry, J. L., & Wainscoat, R. J. 2013, The Extremely Red, Young L Dwarf PSO J318.5338-22.8603: A Free-floating Planetary-mass Analog to Directly Imaged Young Gas-giant Planets, , 777, L20

Lockhart, K. E., Do, T., Larkin, J. E., Boehle, A., Campbell, R. D., Chappell, S., Chu, D., Ciurlo, A., Cosens, M., Fitzgerald, M. P., Ghez, A., Lu, J. R., Lyke, J. E., Mieda, E., Rudy, A. R., Vayner, A., Walth, G., & Wright, S. A. 2019, Characterizing and Improving the Data Reduction Pipeline for the Keck OSIRIS Integral Field Spectrograph, , 157, 75

Luhman, K. L., Mamajek, E. E., Shukla, S. J., & Loutrel, N. P. 2017, A Survey for New Members of the Taurus Star-forming Region with the Sloan Digital Sky Survey, , 153, 46

Luhman, K. L., Allen, L. E., Allen, P. R., Gutermuth, R. A., Hartmann, L., Mamajek, E. E., Megeath, S. T., Myers, P. C., & Fazio, G. G. 2008, The Disk Population of the Chamaeleon I Star-forming Region, , 675, 1375

Luna, J. L., & Morley, C. 2019, in AAS/Division for Extreme Solar Systems Abstracts, Vol. 51,

AAS/Division for Extreme Solar Systems Abstracts, 329.13

Macintosh, B., Graham, J. R., Ingraham, P., Konopacky, Q., Marois, C., Perrin, M., Poyneer, L., Bauman, B., Barman, T., Burrows, A. S., Cardwell, A., Chilcote, J., De Rosa, R. J., Dillon, D., Doyon, R., Dunn, J., Erikson, D., Fitzgerald, M. P., Gavel, D., Goodsell, S., Hartung, M., Hibon, P., Kalas, P., Larkin, J., Maire, J., Marchis, F., Marley, M. S., McBride, J., Millar-Blanchaer, M., Morzinski, K., Norton, A., Oppenheimer, B. R., Palmer, D., Patience, J., Pueyo, L., Rantakyro, F., Sadakuni, N., Saddlemyer, L., Savransky, D., Serio, A., Soummer, R., Sivaramakrishnan, A., Song, I., Thomas, S., Wallace, J. K., Wiktorowicz, S., & Wolff, S. 2014, First light of the Gemini Planet Imager, Proceedings of the National Academy of Science, 111, 12661

Macintosh, B., Graham, J. R., Barman, T., De Rosa, R. J., Konopacky, Q., Marley, M. S., Marois, C., Nielsen, E. L., Pueyo, L., Rajan, A., Rameau, J., Saumon, D., Wang, J. J., Patience, J., Ammons, M., Arriaga, P., Artigau, E., Beckwith, S., Brewster, J., Bruzzone, S., Bulger, J., Burningham, B., Burrows, A. S., Chen, C., Chiang, E., Chilcote, J. K., Dawson, R. I., Dong, R., Doyon, R., Draper, Z. H., Duchêne, G., Esposito, T. M., Fabrycky, D., Fitzgerald, M. P., Follette, K. B., Fortney, J. J., Gerard, B., Goodsell, S., Greenbaum, A. Z., Hibon, P., Hinkley, S., Cotten, T. H., Hung, L. W., Ingraham, P., Johnson-Groh, M., Kalas, P., Lafreniere, D., Larkin, J. E., Lee, J., Line, M., Long, D., Maire, J., Marchis, F., Matthews, B. C., Max, C. E., Metchev, S., Millar-Blanchaer, M. A., Mittal, T., Morley, C. V., Morzinski, K. M., Murray-Clay, R., Oppenheimer, R., Palmer, D. W., Patel, R., Perrin, M. D., Poyneer, L. A., Rafikov, R. R., Rantakyrö, F. T., Rice, E. L., Rojo, P., Rudy, A. R., Ruffio, J. B., Ruiz, M. T., Sadakuni, N., Saddlemyer, L., Salama, M., Savransky, D., Schneider, A. C., Sivaramakrishnan, A., Song, I., Soummer, R., Thomas, S., Vasisht, G., Wallace, J. K., Ward-Duong, K., Wiktorowicz, S. J., Wolff, S. G., & Zuckerman, B. 2015, Discovery and spectroscopy of the young jovian planet 51 Eri b with the Gemini Planet Imager, Science, 350, 64

Madhusudhan, N. 2019, Exoplanetary Atmospheres: Key Insights, Challenges, and Prospects, , 57, 617

Madhusudhan, N., Bitsch, B., Johansen, A., & Eriksson, L. 2017, Atmospheric signatures of giant exoplanet formation by pebble accretion, , 469, 4102

Madhusudhan, N., Mousis, O., Johnson, T. V., & Lunine, J. I. 2011, Carbon-rich Giant Planets: Atmospheric Chemistry, Thermal Inversions, Spectra, and Formation Conditions, , 743, 191

Mamajek, E. E., & Meyer, M. R. 2007, An Improbable Solution to the Underluminosity of 2M1207B: A Hot Protoplanet Collision Afterglow, , 668, L175

Mansfield, M., Line, M. R., Bean, J. L., Fortney, J. J., Parmentier, V., Wiser, L., Kempton, E. M. R., Gharib-Nezhad, E., Sing, D. K., López-Morales, M., Baxter, C., Désert, J.-M., Swain, M. R., & Roudier, G. M. 2021, A unique hot Jupiter spectral sequence with evidence for compositional diversity, Nature Astronomy, 5, 1224

Marois, C., Macintosh, B., Barman, T., Zuckerman, B., Song, I., Patience, J., Lafrenière, D., & Doyon, R. 2008, Direct Imaging of Multiple Planets Orbiting the Star HR 8799, Science, 322, 1348

Marois, C., Zuckerman, B., Konopacky, Q. M., Macintosh, B., & Barman, T. 2010, Images of a fourth planet orbiting HR 8799, , 468, 1080

McMahon, R. G., Banerji, M., Gonzalez, E., Koposov, S. E., Bejar, V. J., Lodieu, N., Rebolo, R., & VHS Collaboration. 2013, First Scientific Results from the VISTA Hemisphere Survey (VHS), The Messenger, 154, 35

Meyer, L., Ghez, A. M., Schödel, R., Yelda, S., Boehle, A., Lu, J. R., Do, T., Morris, M. R., Becklin, E. E., & Matthews, K. 2012, The Shortest-Known-Period Star Orbiting Our Galaxy's Supermassive Black Hole, Science, 338, 84

Miles, B. E., Skemer, A. J., Barman, T. S., Allers, K. N., & Stone, J. M. 2018, Methane in Analogs of Young Directly Imaged Exoplanets, , 869, 18

Miles, B. E., Skemer, A. J. I., Morley, C. V., Marley, M. S., Fortney, J. J., Allers, K. N., Faherty, J. K., Geballe, T. R., Visscher, C., Schneider, A. C., Lupu, R., Freedman, R. S., & Bjoraker, G. L. 2020, Observations of Disequilibrium CO Chemistry in the Coldest Brown Dwarfs, , 160, 63

Mizuno, H., Nakazawa, K., & Hayashi, C. 1980, Dissolution of the primordial rare gases into the molten Earth's material, Earth and Planetary Science Letters, 50, 202

Mohanty, S., Jayawardhana, R., Huélamo, N., & Mamajek, E. 2007, The Planetary Mass Companion 2MASS 1207-3932B: Temperature, Mass, and Evidence for an Edge-on Disk, , 657, 1064

Mollière, P., Wardenier, J. P., van Boekel, R., Henning, T., Molaverdikhani, K., & Snellen, I. A. G. 2019, petitRADTRANS. A Python radiative transfer package for exoplanet characterization and retrieval, , 627, A67

Mollière, P., Stolker, T., Lacour, S., Otten, G. P. P. L., Shangguan, J., Charnay, B., Molyarova, T., Nowak, M., Henning, T., Marleau, G. D., Semenov, D. A., van Dishoeck, E., Eisenhauer, F., Garcia, P., Garcia Lopez, R., Girard, J. H., Greenbaum, A. Z., Hinkley, S., Kervella, P., Kreidberg, L., Maire, A. L., Nasedkin, E., Pueyo, L., Snellen, I. A. G., Vigan, A., Wang, J., de Zeeuw, P. T., & Zurlo, A. 2020, Retrieving scattering clouds and disequilibrium chemistry in the atmosphere of HR 8799e, , 640, A131

Mollière, P., Molyarova, T., Bitsch, B., Henning, T., Schneider, A., Kreidberg, L., Eistrup, C., Burn, R., Nasedkin, E., Semenov, D., Mordasini, C., Schlecker, M., Schwarz, K. R., Lacour, S., Nowak, M., & Schulik, M. 2022, Interpreting the Atmospheric Composition of Exoplanets:

Sensitivity to Planet Formation Assumptions, , 934, 74

Morbidelli, A., Szulágyi, J., Crida, A., Lega, E., Bitsch, B., Tanigawa, T., & Kanagawa, K. 2014, Meridional circulation of gas into gaps opened by giant planets in three-dimensional low-viscosity disks, , 232, 266

Mordasini, C., van Boekel, R., Mollière, P., Henning, T., & Benneke, B. 2016, The Imprint of Exoplanet Formation History on Observable Present-day Spectra of Hot Jupiters, , 832, 41

Mousis, O., Lunine, J. I., Pasek, M., Cordier, D., Hunter Waite, J., Mandt, K. E., Lewis, W. S., & Nguyen, M.-J. 2009, A primordial origin for the atmospheric methane of Saturn's moon Titan, , 204, 749

Nielsen, E. L., De Rosa, R. J., Macintosh, B., Wang, J. J., Ruffio, J.-B., Chiang, E., Marley, M. S., Saumon, D., Savransky, D., Ammons, S. M., Bailey, V. P., Barman, T., Blain, C., Bulger, J., Burrows, A., Chilcote, J., Cotten, T., Czekala, I., Doyon, R., Duchêne, G., Esposito, T. M., Fabrycky, D., Fitzgerald, M. P., Follette, K. B., Fortney, J. J., Gerard, B. L., Goodsell, S. J., Graham, J. R., Greenbaum, A. Z., Hibon, P., Hinkley, S., Hirsch, L. A., Hom, J., Hung, L.-W., Dawson, R. I., Ingraham, P., Kalas, P., Konopacky, Q., Larkin, J. E., Lee, E. J., Lin, J. W., Maire, J., Marchis, F., Marois, C., Metchev, S., Millar-Blanchaer, M. A., Morzinski, K. M., Oppenheimer, R., Palmer, D., Patience, J., Perrin, M., Poyneer, L., Pueyo, L., Rafikov, R. R., Rajan, A., Rameau, J., Rantakyrö, F. T., Ren, B., Schneider, A. C., Sivaramakrishnan, A., Song, I., Soummer, R., Tallis, M., Thomas, S., Ward-Duong, K., & Wolff, S. 2019, The Gemini Planet Imager Exoplanet Survey: Giant Planet and Brown Dwarf Demographics from 10 to 100 au, , 158, 13

Nikolov, N., Sing, D. K., Goyal, J., Henry, G. W., Wakeford, H. R., Evans, T. M., López-Morales, M., García Muñoz, A., Ben-Jaffel, L., Sanz-Forcada, J., Ballester, G. E., Kataria, T., Barstow, J. K., Bourrier, V., Buchhave, L. A., Cohen, O., Deming, D., Ehrenreich, D., Knutson, H., Lavvas, P., Lecavelier des Etangs, A., Lewis, N. K., Mandell, A. M., & Williamson, M. H. 2018, Hubble PanCET: an isothermal day-side atmosphere for the bloated gas-giant HAT-P-32Ab, , 474, 1705

Noll, K. S., Geballe, T. R., Leggett, S. K., & Marley, M. S. 2000, The Onset of Methane in L Dwarfs, , 541, L75

Öberg, K. I., & Bergin, E. A. 2016, Excess C/O and C/H in Outer Protoplanetary Disk Gas, , 831, L19

Öberg, K. I., Murray-Clay, R., & Bergin, E. A. 2011, The Effects of Snowlines on C/O in Planetary Atmospheres, , 743, L16

O'Neil, K. K., Martinez, G. D., Hees, A., Ghez, A. M., Do, T., Witzel, G., Konopacky, Q., Becklin, E. E., Chu, D. S., Lu, J. R., Matthews, K., & Sakai, S. 2019, Improving Orbit

Estimates for Incomplete Orbits with a New Approach to Priors: with Applications from Black Holes to Planets, , 158, 4

Oreshenko, M., Kitzmann, D., Márquez-Neila, P., Malik, M., Bowler, B. P., Burgasser, A. J., Sznitman, R., Fisher, C. E., & Heng, K. 2020, Supervised Machine Learning for Intercomparison of Model Grids of Brown Dwarfs: Application to GJ 570D and the Epsilon Indi B Binary System, , 159, 6

Owen, T., Mahaffy, P., Niemann, H. B., Atreya, S., Donahue, T., Bar-Nun, A., & de Pater, I. 1999, A low-temperature origin for the planetesimals that formed Jupiter, , 402, 269

Petit dit de la Roche, D. J. M., Hoeijmakers, H. J., & Snellen, I. A. G. 2018, Molecule mapping of HR8799b using OSIRIS on Keck. Strong detection of water and carbon monoxide, but no methane, , 616, A146

Petrus, S., Bonnefoy, M., Chauvin, G., Babusiaux, C., Delorme, P., Lagrange, A. M., Florent, N., Bayo, A., Janson, M., Biller, B., Manjavacas, E., Marleau, G. D., & Kopytova, T. 2020, A new take on the low-mass brown dwarf companions on wide orbits in Upper-Scorpius, , 633, A124

Petrus, S., Bonnefoy, M., Chauvin, G., Charnay, B., Marleau, G. D., Gratton, R., Lagrange, A. M., Rameau, J., Mordasini, C., Nowak, M., Delorme, P., Boccaletti, A., Carlotti, A., Houllé, M., Vigan, A., Allard, F., Desidera, S., D'Orazi, V., Hoeijmakers, H. J., Wyttenbach, A., & Lavie, B. 2021, Medium-resolution spectrum of the exoplanet HIP 65426 b, , 648, A59

Pinhas, A., Madhusudhan, N., Gandhi, S., & MacDonald, R. 2019, H_2O abundances and cloud properties in ten hot giant exoplanets, , 482, 1485

Pinilla, P., Lenz, C. T., & Stammler, S. M. 2021, Growing and trapping pebbles with fragile collisions of particles in protoplanetary disks, , 645, A70

Piso, A.-M. A., Öberg, K. I., Birnstiel, T., & Murray-Clay, R. A. 2015, C/O and Snowline Locations in Protoplanetary Disks: The Effect of Radial Drift and Viscous Gas Accretion, , 815, 109

Pollack, J. B., Hubickyj, O., Bodenheimer, P., Lissauer, J. J., Podolak, M., & Greenzweig, Y. 1996, Formation of the Giant Planets by Concurrent Accretion of Solids and Gas, , 124, 62

Rameau, J., Chauvin, G., Lagrange, A. M., Meshkat, T., Boccaletti, A., Quanz, S. P., Currie, T., Mawet, D., Girard, J. H., Bonnefoy, M., & Kenworthy, M. 2013, Confirmation of the Planet around HD 95086 by Direct Imaging, , 779, L26

Rasio, F. A., & Ford, E. B. 1996, Dynamical instabilities and the formation of extrasolar planetary systems, Science, 274, 954

Rich, E. A., Currie, T., Wisniewski, J. P., Hashimoto, J., Brandt, T. D., Carson, J. C., Kuzuhara, M., & Uyama, T. 2016, Thermal Infrared Imaging and Atmospheric Modeling of VHS J125601.92-125723.9 b: Evidence for Moderately Thick Clouds and Equilibrium Carbon Chemistry in a Hierarchical Triple System, , 830, 114

Royer, F., Zorec, J., & Gómez, A. E. 2007, Rotational velocities of A-type stars. III. Velocity distributions, , 463, 671

Ruffio, J.-B., Macintosh, B., Konopacky, Q. M., Barman, T., De Rosa, R. J., Wang, J. J., Wilcomb, K. K., Czekala, I., & Marois, C. 2019, Radial Velocity Measurements of HR 8799 b and c with Medium Resolution Spectroscopy, , 158, 200

Ruffio, J.-B., Konopacky, Q. M., Barman, T., Macintosh, B., Wilcomb, K. K., De Rosa, R. J., Wang, J. J., Czekala, I., & Marois, C. 2021, Deep exploration of the planets HR 8799 b, c, and d with moderate resolution spectroscopy, arXiv e-prints, arXiv:2109.07614

Safronov, V. S., & Zvjagina, E. V. 1969, Relative Sizes of the Largest Bodies during the Accumulation of Planets, , 10, 109

Santos, N. C., Adibekyan, V., Figueira, P., Andreasen, D. T., Barros, S. C. C., Delgado-Mena, E., Demangeon, O., Faria, J. P., Oshagh, M., Sousa, S. G., Viana, P. T. P., & Ferreira, A. C. S. 2017, Observational evidence for two distinct giant planet populations, , 603, A30

Sing, D. K., Fortney, J. J., Nikolov, N., Wakeford, H. R., Kataria, T., Evans, T. M., Aigrain, S., Ballester, G. E., Burrows, A. S., Deming, D., Désert, J.-M., Gibson, N. P., Henry, G. W., Huitson, C. M., Knutson, H. A., Lecavelier Des Etangs, A., Pont, F., Showman, A. P., Vidal-Madjar, A., Williamson, M. H., & Wilson, P. A. 2016, A continuum from clear to cloudy hot-Jupiter exoplanets without primordial water depletion, , 529, 59

Skrutskie, M. F., Cutri, R. M., Stiening, R., Weinberg, M. D., Schneider, S., Carpenter, J. M., Beichman, C., Capps, R., Chester, T., Elias, J., Huchra, J., Liebert, J., Lonsdale, C., Monet, D. G., Price, S., Seitzer, P., Jarrett, T., Kirkpatrick, J. D., Gizis, J. E., Howard, E., Evans, T., Fowler, J., Fullmer, L., Hurt, R., Light, R., Kopan, E. L., Marsh, K. A., McCallon, H. L., Tam, R., Van Dyk, S., & Wheelock, S. 2006, The Two Micron All Sky Survey (2MASS), , 131, 1163

Snellen, I. A. G., Brandl, B. R., de Kok, R. J., Brogi, M., Birkby, J., & Schwarz, H. 2014, Fast spin of the young extrasolar planet β Pictoris b, , 509, 63

Stone, J. M., Skemer, A. J., Kratter, K. M., Dupuy, T. J., Close, L. M., Eisner, J. A., Fortney, J. J., Hinz, P. M., Males, J. R., Morley, C. V., Morzinski, K. M., & Ward-Duong, K. 2016, Adaptive Optics imaging of VHS 1256-1257: A Low Mass Companion to a Brown Dwarf Binary System, , 818, L12

Szulágyi, J., Morbidelli, A., Crida, A., & Masset, F. 2014, Accretion of Jupiter-mass Planets in the Limit of Vanishing Viscosity, , 782, 65

Takeda, Y., & Honda, S. 2016, Oxygen abundance determination of B-type stars with the O I 7771-5 Å lines*, , 68, 32

Teague, R., Bae, J., & Bergin, E. A. 2019, Meridional flows in the disk around a young star, , 574, 378

Theissen, C. A., Konopacky, Q. M., Lu, J. R., Kim, D., Zhang, S. Y., Hsu, C.-C., Chu, L., & Wei, L. 2022, The 3D Kinematics of the Orion Nebula Cluster: NIRSPEC-AO Radial Velocities of the Core Population, , 926, 141

Theissen, C. A., & West, A. A. 2014, Warm Dust around Cool Stars: Field M Dwarfs with WISE 12 or 22 μm Excess Emission, , 794, 146

Todorov, K., Luhman, K. L., & McLeod, K. K. 2010, Discovery of a Planetary-mass Companion to a Brown Dwarf in Taurus, , 714, L84

Todorov, K. O., Line, M. R., Pineda, J. E., Meyer, M. R., Quanz, S. P., Hinkley, S., & Fortney, J. J. 2016, The Water Abundance of the Directly Imaged Substellar Companion κ And b Retrieved from a Near Infrared Spectrum, , 823, 14

Toomre, A. 1964, On the gravitational stability of a disk of stars., , 139, 1217

Tsiaras, A., Waldmann, I. P., Rocchetto, M., Varley, R., Morello, G., Damiano, M., & Tinetti, G. 2016, A New Approach to Analyzing HST Spatial Scans: The Transmission Spectrum of HD 209458 b, , 832, 202

Tsiaras, A., Waldmann, I. P., Zingales, T., Rocchetto, M., Morello, G., Damiano, M., Karpouzas, K., Tinetti, G., McKemmish, L. K., Tennyson, J., & Yurchenko, S. N. 2018, A Population Study of Gaseous Exoplanets, , 155, 156

Uyama, T., Currie, T., Hori, Y., De Rosa, R. J., Mede, K., Brandt, T. D., Kwon, J., Guyon, O., Lozi, J., Jovanovic, N., Martinache, F., Kudo, T., Tamura, M., Kasdin, N. J., Groff, T., Chilcote, J., Hayashi, M., McElwain, M. W., Asensio-Torres, R., Janson, M., Knapp, G. R., & Serabyn, E. 2020, Atmospheric Characterization and Further Orbital Modeling of κ Andromeda b, , 159, 40

van der Marel, N., Bosman, A. D., Krijt, S., Mulders, G. D., & Bergner, J. B. 2021, If you like C/O variations, you should have put a ring on it, , 653, L9

van der Marel, N., van Dishoeck, E. F., Bruderer, S., Andrews, S. M., Pontoppidan, K. M., Herczeg, G. J., van Kempen, T., & Miotello, A. 2016, Resolved gas cavities in transitional

disks inferred from CO isotopologs with ALMA, , 585, A58

Vigan, A., Fontanive, C., Meyer, M., Biller, B., Bonavita, M., Feldt, M., Desidera, S., Marleau, G. D., Emsenhuber, A., Galicher, R., Rice, K., Forgan, D., Mordasini, C., Gratton, R., Le Coroller, H., Maire, A. L., Cantalloube, F., Chauvin, G., Cheetham, A., Hagelberg, J., Lagrange, A. M., Langlois, M., Bonnefoy, M., Beuzit, J. L., Boccaletti, A., D'Orazi, V., Delorme, P., Dominik, C., Henning, T., Janson, M., Lagadec, E., Lazzoni, C., Ligi, R., Menard, F., Mesa, D., Messina, S., Moutou, C., Müller, A., Perrot, C., Samland, M., Schmid, H. M., Schmidt, T., Sissa, E., Turatto, M., Udry, S., Zurlo, A., Abe, L., Antichi, J., Asensio-Torres, R., Baruffolo, A., Baudoz, P., Baudrand, J., Bazzon, A., Blanchard, P., Bohn, A. J., Brown Sevilla, S., Carbillet, M., Carle, M., Cascone, E., Charton, J., Claudi, R., Costille, A., De Caprio, V., Delboulbé, A., Dohlen, K., Engler, N., Fantinel, D., Feautrier, P., Fusco, T., Gigan, P., Girard, J. H., Giro, E., Gisler, D., Gluck, L., Gry, C., Hubin, N., Hugot, E., Jaquet, M., Kasper, M., Le Mignant, D., Llored, M., Madec, F., Magnard, Y., Martinez, P., Maurel, D., Möller-Nilsson, O., Mouillet, D., Moulin, T., Origné, A., Pavlov, A., Perret, D., Petit, C., Pragt, J., Puget, P., Rabou, P., Ramos, J., Rickman, E. L., Rigal, F., Rochat, S., Roelfsema, R., Rousset, G., Roux, A., Salasnich, B., Sauvage, J. F., Sevin, A., Soenke, C., Stadler, E., Suarez, M., Wahhaj, Z., Weber, L., & Wildi, F. 2021, The SPHERE infrared survey for exoplanets (SHINE). III. The demographics of young giant exoplanets below 300 au with SPHERE, , 651, A72

Visscher, C., & Fegley, Bruce, J. 2005, Chemical Constraints on the Water and Total Oxygen Abundances in the Deep Atmosphere of Saturn, , 623, 1221

Vos, J. M., Biller, B. A., Bonavita, M., Eriksson, S., Liu, M. C., Best, W. M. J., Metchev, S., Radigan, J., Allers, K. N., Janson, M., Buenzli, E., Dupuy, T. J., Bonnefoy, M., Manjavacas, E., Brandner, W., Crossfield, I., Deacon, N., Henning, T., Homeier, D., Kopytova, T., & Schlieder, J. 2019, A search for variability in exoplanet analogues and low-gravity brown dwarfs, , 483, 480

Wang, J., Mawet, D., Fortney, J. J., Hood, C., Morley, C. V., & Benneke, B. 2018a, Detecting Water in the Atmosphere of HR 8799 c with L-band High-dispersion Spectroscopy Aided by Adaptive Optics, , 156, 272

Wang, J., Kolecki, J. R., Ruffio, J.-B., Wang, J. J., Mawet, D., Baker, A., Bartos, R., Blake, G. A., Bond, C. Z., Calvin, B., Cetre, S., Delorme, J.-R., Doppmann, G., Echeverri, D., Finnerty, L., Fitzgerald, M. P., Jovanovic, N., Liu, M. C., Lopez, R., Morris, E., Pai Asnodkar, A., Pezzato, J., Ragland, S., Roy, A., Ruane, G., Sappey, B., Schofield, T., Skemer, A., Venenciano, T., Kent Wallace, J., Wallack, N. L., Wizinowich, P., & Xuan, J. W. 2022, Retrieving the C and O Abundances of HR 7672 AB: A Solar-type Primary Star with a Benchmark Brown Dwarf, , 163, 189

Wang, J. J., Graham, J. R., Dawson, R., Fabrycky, D., De Rosa, R. J., Pueyo, L., Konopacky, Q., Macintosh, B., Marois, C., Chiang, E., Ammons, S. M., Arriaga, P., Bailey, V. P., Barman, T., Bulger, J., Chilcote, J., Cotten, T., Doyon, R., Duchêne, G., Esposito, T. M., Fitzgerald,

M. P., Follette, K. B., Gerard, B. L., Goodsell, S. J., Greenbaum, A. Z., Hibon, P., Hung, L.-W., Ingraham, P., Kalas, P., Larkin, J. E., Maire, J., Marchis, F., Marley, M. S., Metchev, S., Millar-Blanchaer, M. A., Nielsen, E. L., Oppenheimer, R., Palmer, D., Patience, J., Perrin, M., Poyneer, L., Rajan, A., Rameau, J., Rantakyrö, F. T., Ruffio, J.-B., Savransky, D., Schneider, A. C., Sivaramakrishnan, A., Song, I., Soummer, R., Thomas, S., Wallace, J. K., Ward-Duong, K., Wiktorowicz, S., & Wolff, S. 2018b, Dynamical Constraints on the HR 8799 Planets with GPI, , 156, 192

Ward, W. R. 1997, Protoplanet Migration by Nebula Tides, , 126, 261

Weidenschilling, S. J., & Marzari, F. 1996, Gravitational scattering as a possible origin for giant planets at small stellar distances, , 384, 619

Wilcomb, K. K., Konopacky, Q. M., Barman, T. S., Theissen, C. A., Ruffio, J.-B., Brock, L., Macintosh, B., & Marois, C. 2020, Moderate-resolution K-band Spectroscopy of Substellar Companion κ Andromedae b, , 160, 207

Witte, S., Helling, C., Barman, T., Heidrich, N., & Hauschildt, P. H. 2011, Dust in brown dwarfs and extra-solar planets. III. Testing synthetic spectra on observations, , 529, A44

Woitke, P., Helling, C., Hunter, G. H., Millard, J. D., Turner, G. E., Worters, M., Blecic, J., & Stock, J. W. 2018, Equilibrium chemistry down to 100 K. Impact of silicates and phyllosilicates on the carbon to oxygen ratio, , 614, A1

Wong, M. H., Bjoraker, G. L., Smith, M. D., Flasar, F. M., & Nixon, C. A. 2004, Identification of the 10-μm ammonia ice feature on Jupiter, , 52, 385

Wu, Y., Singh, H. P., Prugniel, P., Gupta, R., & Koleva, M. 2011, Coudé-feed stellar spectral library - atmospheric parameters, , 525, A71

Yurchenko, S. N., & Tennyson, J. 2014, ExoMol line lists - IV. The rotation-vibration spectrum of methane up to 1500 K, , 440, 1649

Zahnle, K. J., & Marley, M. S. 2014, Methane, Carbon Monoxide, and Ammonia in Brown Dwarfs and Self-Luminous Giant Planets, , 797, 41

Zhang, Y., Snellen, I. A. G., Bohn, A. J., Mollière, P., Ginski, C., Hoeijmakers, H. J., Kenworthy, M. A., Mamajek, E. E., Meshkat, T., Reggiani, M., & Snik, F. 2021, The ^{13}CO-rich atmosphere of a young accreting super-Jupiter, , 595, 370

Zuckerman, B., Rhee, J. H., Song, I., & Bessell, M. S. 2011, The Tucana/Horologium, Columba, AB Doradus, and Argus Associations: New Members and Dusty Debris Disks, , 732, 61